Remote Sensing of Environment 232 (2019) 111304

Contents lists available at ScienceDirect

Remote Sensing of Environment

journal homepage: www.elsevier.com/locate/rse

A review of earth surface thermal radiation directionality observing and modeling: Historical development, current status and perspectives

Biao Cao[a], Qinhuo Liu[a,b,*], Yongming Du[a], Jean-Louis Roujean[c], Jean-Philippe Gastellu-Etchegorry[c], Isabel F. Trigo[d], Wenfeng Zhan[e], Yunyue Yu[f], Jie Cheng[g], Frédéric Jacob[h], Jean-Pierre Lagouarde[i], Zunjian Bian[a], Hua Li[a], Tian Hu[j,a], Qing Xiao[a,b]

[a] State Key Laboratory of Remote Sensing Science, Institute of Remote Sensing and Digital Earth, Chinese Academy of Sciences, Beijing 100101, China
[b] College of Resources and Environment, University of Chinese Academy of Sciences, Beijing 100049, China
[c] Centre d'Etudes Spatiales de la BIOsphère (CESBIO) - UPS, CNES, CNRS, IRD, Université de Toulouse, 31401 Toulouse cedex 9, France
[d] IPMA – Instituto Português do Mar e da Atmosfera, Department of Meteorology and Geophysics, Lisbon, Portugal
[e] Jiangsu Provincial Key Laboratory of Geographic Information Science and Technology, International Institute of Earth System Science, Nanjing University, Nanjing 210023, China
[f] National Environmental Satellite, Data, and Information Service Center for Satellite Applications and Research, National Oceanic and Atmospheric Administration, Camp Springs, MD 20746, USA
[g] Institute of Remote Sensing Science and Engineering, Faculty of Geographical Science, Beijing Normal University, Beijing, China
[h] LISAH, IRD, INRA, Montpellier SupAgro, University of Montpellier, Montpellier, France
[i] INRA/UMR ISPA, Villenave d'Ornon, France
[j] Environmental Futures Research Institute, School of Environment and Science, Griffith University, Nathan, QLD 4111, Australia

ARTICLE INFO

Keywords:
Directional brightness temperature
Directional radiometric temperature
Directional canopy emissivity
Directional thermal emission
Thermal radiation directionality
Thermal emission directionality
Directional anisotropy
Angular anisotropy
Thermal anisotropy
Land surface temperature anisotropy

ABSTRACT

The Earth surface thermal infrared (TIR) radiation shows conspicuously an anisotropic behavior just like the bi-directional reflectance of visible and near infrared spectral domains. The importance of thermal radiation directionality (TRD) is being more and more widely recognized in the applications because of the magnitude of the effects generated. The effects of TRD were originally evidenced through experiments in 1962, showing that two sensors simultaneously measuring temperature of the same scene may get significantly different values when the viewing geometry is different. Such effect limits inter-comparison of measurement datasets and land surface temperature (LST) products acquired at different view angles, while raising the question of measurement reliability when used to characterize land surface processes. These early experiments fostered the development of modeling approaches to quantify TRD with the aim of developing a correction for Earth surface TIR radiation. Initiatives for pushing the analysis of TIR data through modeling have been lasted since 1970s. They were initially aimed at mimicking the observed TIR radiance with consideration of canopy structure, component emissivities and temperatures, and Earth surface energy exchange processes. Presently, observing the Earth surface TRD effect is still a challenging task because the TIR status changes rapidly. Firstly, a brief theoretical background and the basic radiative transfer equation are presented. Then, this paper reviews the historical development and current status of observing TRD in the laboratory, in-situ, from airborne and space-borne platforms. Accordingly, the TRD model development, including radiative transfer models, geometric models, hybrid models, 3D models, and parametric models are reviewed for surfaces of water, ice and sea, snow, barren lands, vegetation and urban landscapes, respectively. Next, we introduce three potential applications, including normalizing the LST products, estimating the hemispheric upward longwave radiation using multi-angular TIR observations and separating surface component temperatures. Finally, we give hints and directions for future research work. The last section summarizes the study and stresses three main conclusions.

* Corresponding author at: State Key Laboratory of Remote Sensing Science, Institute of Remote Sensing and Digital Earth, Chinese Academy of Sciences, Beijing 100101, China.
E-mail addresses: caobiao@radi.ac.cn (B. Cao), liuqh@radi.ac.cn (Q. Liu).

https://doi.org/10.1016/j.rse.2019.111304
Received 31 October 2018; Received in revised form 30 May 2019; Accepted 5 July 2019
Available online 18 July 2019

1. Introduction

Land surface temperature (LST) and sea surface temperature (SST) are two of the 54 Essential Climate Variables (ECVs) of the Global Climate Observation System (World Meteorological Organization, 2016). SST exerts a major influence on the exchanges of energy, momentum and gases between the sea and atmosphere, and largely governs the atmospheric response to the sea (Barton, 1992). LST value is one of the most important parameters in the physical processes of surface energy and water balance at both local and global scales (Anderson et al., 2008). LST value is the direct driving force of turbulent heat fluxes at the land surface and atmosphere interface. It is widely utilized in the fields of radiation budget (Cheng et al., 2013) and hydrological cycle (Jia et al., 2003).

Remote sensing observations offer the only possibility for measuring LST at high spatial resolution and temporal frequency, thus ensuring a wide area coverage (Li et al., 2013d). The LST estimation methods can be classified into two categories. The first, which includes the single-channel method (Qin et al., 2001), multi-channel generalized split-window algorithms (Wan and Dozier, 1996) and the multi-angle method (Sobrino, 1996), assumes that land surface emissivity (LSE) is known. The second category aims at retrieval of both LSE and LST, as is the case of simultaneous LST and LSE retrieval methods with known atmospheric information (Borel, 1998; Cheng et al., 2010a; Gillespie et al., 1998; Wan and Li, 1997), and simultaneous retrieval of LST, LSE and atmospheric profile (Ma et al., 2002; Wang et al., 2010). All of these methods generally assume that the land surface has an isotropic thermal emission and also is at thermodynamic equilibrium.

Maximal view zenith angle (VZA) of moderate spatial resolution thermal sensors onboard polar satellites (e.g. Terra/Aqua MODIS, NOAA AVHRR and FY-3 VIRR) and geostationary satellites (e.g. GOES ABI, MSG SEVIRI and FY-2 SVISSR) can be over 60°. Many studies reported that large differences of temperature measurement may result from different viewing angles, either on the ground (Kimes and Kirchner, 1983), aircraft (Lagouarde et al., 2010) or satellite (Hu et al., 2016a; Trigo et al., 2008). The thermal radiation directionality (TRD) effect can be defined as the difference between off-nadir and nadir (assuming this as a reference viewing geometry) brightness temperatures. Depending on spatial resolution and environmental conditions, such difference can reach 16 K over vegetation canopies (Kimes and Kirchner, 1983) and 12 K over urban areas (Lagouarde et al., 2013, 2010), which demands to be considered in most applications. However, until now, the TRD is ignored in operational LST estimation algorithms (Sobrino and Romaguera, 2004; Wan and Dozier, 1996; Yu et al., 2009). The presence of TRD effects seriously limits the inter-comparison of measurement datasets and LST products acquired at different view angles over the same scene at minimal observation time differences, but also the time series analysis from different viewing angle observations in the context of long-term monitoring, and the mapping over large areas with changes in viewing angles.

The study of TRD can be traced back to a 1962 pioneered work on energy balance (Monteith and Szeicz, 1962). Further in time, the concern moved progressively to the area of thermal infrared (TIR) remote sensing applications, like the assessment of directional variability of TIR radiance for various vegetation canopies (Kimes et al., 1980). In the last 40 years, several models have been proposed to simulate the directional brightness temperature (DBT) distribution or LSE distribution over different surfaces. Usually, these surfaces were assumed to be unique thematic surfaces. More recently, the DBT distribution of mixed pixels has been addressed (Cao et al., 2015; Shi, 2011). The TRD models were aimed at mimicking the observed thermal radiance with consideration of canopy structure, component emissivities and temperatures, and energy budget processes.

For inland water bodies (3.56% of land surface, according to FROM-GLC dataset (Gong et al., 2013)), barren lands (16.51% of land surface) (Garcia-Santos et al., 2012; Sobrino and Cuenca, 1999), and snow and ice (12.81% of land surface) (Cheng et al., 2010b), most of the models are trying to simulate the emissivity directionality, as this is the main source of directional effects on LST over relatively homogeneous surfaces. The structure of such surfaces is simpler when compared with those of vegetation and urban surfaces. The TRD attributed to emissivity is also a main concern for sea surfaces (Masuda et al., 1988; Wu and Smith, 1997). Although the proportion of urban landscapes is the smallest (0.66% of land surface), many models were developed to simulate the urban surface DBT (Fontanilles et al., 2008; Lagouarde et al., 2010) because the thermal environment directly links to the human life in cities, where an increasing larger share of the world's population now resides (https://data.worldbank.org/indicator/SP.URB.TOTL.IN.ZS).

More DBT models have been developed for vegetation canopies (including croplands, forests, grasslands, and shrub lands), which cover 64.72% of the world land surface (see the review by Sobrino et al., 2005). These models can be classified into four main categories: 1) radiative transfer models (RTM), such as S&W^{VM} (Snyder and Wan, 1998), FRA1997 (Francois et al., 1997), FRA2002 (Francois, 2002), REN2015 (Ren et al., 2015a), CE-P (Cao et al., 2018b) and 4SAIL (Verhoef et al., 2007). 2) geometric optical models (GOM), such as MGP (Pinheiro et al., 2004; Rasmussen et al., 2010). 3) hybrid model (HM), such as SLEC (Du et al., 2007). 4) 3D models, such as DART (Gastellu-Etchegorry et al., 2017) and TRGM (Liu et al., 2007).

The physical TRD models can be used for estimating land surface component temperatures (LSCT) of vegetated canopies (Bian et al., 2016). However, most of the existing physical TRD models are not well adapted for operational angular normalization of LST products since they tend to require many input parameters that are generally not available. On the other hand, TIR parametric models (PMs) are much more suitable. Indeed, their degree of generality versus simplicity makes them more appropriate to deal with cases in which fewer parameters are available over a short time period (e.g. Cao et al., 2019; Duffour et al., 2016b; Liu et al., 2018). TIR PMs have other applications, such as improving the accuracy of surface upward longwave radiation (SULR) (Hu et al., 2016b). The LSCT separation, LST product angular normalization and angular integrated SULR estimation are three main TRD related applications being widely discussed in recent years.

Jacob et al. (2008) and Paw U (1992) reviewed the TRD models over vegetated canopies. However, no comprehensive review for all Earth surfaces has been reported until now. In addition, there are many outstanding developments in the area of vegetated canopy TRD modeling in the past ten years, such as mixed-pixel TRD modeling, dynamic modeling and parametric modeling. The statement about the TRD effect is presented diversely across different papers, including thermal radiation directionality, thermal emission directionality, directional anisotropy, angular anisotropy, thermal anisotropy, land surface temperature anisotropy, etc. There are many quantities used to represent the TRD amplitude, such as the absolute temperature value, the temperature difference between off-nadir and nadir, the temperature ratio between off-nadir and nadir, etc. Therefore, now, it is urgent and valuable to summarize the TRD related works for future development. Considering that the LST and LSCT inversion works have been recently reviewed by Li et al. (2013d) and Zhan et al. (2013), respectively, in this paper, we aim at providing an overview of the historical development and current status in the field of TRD observations and modeling, starting with theoretical background (Section 2), followed by the multi-scale observation (Section 3), TRD modeling works (Section 4), some potential applications (Section 5) and future perspectives (Section 6). A brief summary is given at the end of this paper in Section 7.

2. Basic theoretical background

For a non-isothermal landscape, the definition of LSE and LST becomes difficult from both a theoretical and practical point of view. In this section, we present the basic equations for the simulations of the

Table 1
List of definitions of LSE.

Name	Equation	Number	References
r-emissivity	$\varepsilon_r(\theta,\varphi)=\sum_{k=1}^{k=K} a_k(\theta,\varphi)\varepsilon_k(\theta,\varphi)$	(5)	(Norman and Becker, 1995)
effective r-emissivity	$\varepsilon_r'(\theta,\varphi)=\sum_{k=1}^{k=K} a_k(\theta,\varphi)\varepsilon_k(\theta,\varphi)+\Delta\varepsilon_{x\to k}$	(6)	(Chen et al., 2004)
e-emissivity	$\varepsilon_e(\theta,\varphi)=\frac{\sum_{k=1}^{k=K} a_k(\theta,\varphi)\varepsilon_k(\theta,\varphi)B(T_k)}{\sum_{k=1}^{k=K} a_k(\theta,\varphi)B(T_k)}$	(7)	(Norman and Becker, 1995)
apparent emissivity	$\varepsilon_{app}(\theta,\varphi)=\varepsilon_r'(\theta,\varphi)+K(T_0)\sum_{k=1}^{k=K} a_k(\theta,\varphi)\varepsilon_k(\theta,\varphi)(T_k-T_0)$	(8)	(Li et al., 1999)
channel r-emissivity	$\varepsilon_{channel,r}(\theta,\varphi)=\frac{\int_{\lambda_1}^{\lambda_2} f(\lambda)\cdot\sum_{k=1}^{k=K} a_k(\theta,\varphi)\varepsilon_{\lambda,k}(\theta,\varphi)\cdot d\lambda}{\int_{\lambda_1}^{\lambda_2} f(\lambda)\cdot d\lambda}$	(9)	(Wan and Dozier, 1996)
channel e-emissivity	$\varepsilon_{channel,e}(\theta,\varphi)=\frac{\int_{\lambda_1}^{\lambda_2} f(\lambda)\cdot\sum_{k=1}^{k=K} a_k(\theta,\varphi)\varepsilon_{\lambda,k}(\theta,\varphi)B(T_k)\cdot d\lambda}{\int_{\lambda_1}^{\lambda_2} f(\lambda)\cdot\sum_{k=1}^{k=K} a_k(\theta,\varphi)B(T_k)\cdot d\lambda}$	(10)	(Wan and Dozier, 1996)
broadband emissivity	$\varepsilon_{bb}(\theta,\varphi)=\frac{\int_0^\infty \varepsilon_\lambda(\theta,\varphi)B_\lambda(T)\cdot d\lambda}{\int_0^\infty B_\lambda(T)\cdot d\lambda}$	(11)	(Cheng et al., 2013; Wang et al., 2005)

radiative transfer processes in the TIR range, and we also recall the basic definitions of LSE and LST. Finally, no less than fourteen different approaches that were proposed to describe the TRD effects are summarized.

2.1. Basic radiative transfer equation

In our analysis of the radiative transfer equation below, we assume that the contributing terms from solar beam and atmospheric scattered solar energy within the TIR are negligible. Based on the simplistic assumption of isotropy for LST and LSE, the radiative transfer equation can be written as shown in Eq. (1) in which only the atmospheric transmittance and upwelling radiance related to optical path length need to be considered as dependent on the viewing angle:

$$I(\theta_v,\varphi_v)=\tau(\theta_v,\varphi_v)(\varepsilon\cdot B(T)+(1-\varepsilon)R_{at}\downarrow)+R_{at}(\theta_v,\varphi_v)\uparrow \quad (1)$$

where I is the top of atmosphere (TOA) radiance received at the sensor level for a given channel central wavelength (λ), θ_v is the view zenith angle, φ_v is the view azimuth angle, ε is the land surface emissivity, T is the land surface temperature, $R_{at}\downarrow$ is the downward atmospheric radiance at λ, $R_{at}\uparrow$ is the upward atmospheric radiance at λ, and τ is the atmospheric transmittance at λ. $B(T)$ is the radiance calculated by the Plank's law as Eq. (2) at λ.

$$B_\lambda(T)=\frac{1.191\times 10^8}{\lambda^5\left[\exp\left(\frac{1.439\times 10^4}{\lambda\cdot T}\right)-1\right]} \quad (2)$$

Note that the symbol for wavelength, λ, is omitted in Eq. (1) and other following equations for the sake of simplicity. Actually, LST and LSE are anisotropic quantities mostly due to the non-isothermal temperature distribution combined with the 3D architecture of these surfaces. This is accounted for in Eq. (3), where $I_{outgoing}$ is the directional surface outgoing radiance at the bottom of atmosphere (BOA) for λ. It includes the surface emission term and the surface reflected downward atmospheric emission term.

$$\begin{aligned} I(\theta_v,\varphi_v) &= \tau(\theta_v,\varphi_v)I_{outgoing}(\theta_v,\varphi_v)+R_{at}(\theta_v,\varphi_v)\uparrow \\ &= \tau(\theta_v,\varphi_v)(\varepsilon(\theta_v,\varphi_v)B(T(\theta_v,\varphi_v))+(1-\varepsilon(\theta_v,\varphi_v)) \\ &\quad R_{at}\downarrow)+R_{at}(\theta_v,\varphi_v)\uparrow \end{aligned} \quad (3)$$

The estimation of LST primarily relies on the retrieval of the $T(\theta_v, \varphi_v)$ value from the sensor observed $I(\theta_v, \varphi_v)$ after a correction of the atmospheric effects and also LSE. The goal of TRD modeling is to establish a relationship between $B^{-1}(I_{outgoing}(0,0))$ and $B^{-1}(I_{outgoing}(\theta_v, \varphi_v))$ or $T(0,0)$ and $T(\theta_v, \varphi_v)$ or $\varepsilon(0,0)$ and $\varepsilon(\theta_v, \varphi_v)$. This corresponds to the BOA DBT modeling or LST modeling or LSE modeling, respectively. Meanwhile, research work on TRD is focused on revealing the relationship between canopy structure, distributions of component temperatures and directional radiance. For geometric models, the challenge is in calculating the contribution of each component and the contribution of their mutual scattering, as shown in Eq. (4).

$$\begin{aligned} I(\theta_v,\varphi_v) = \tau(\theta_v,\varphi_v)\cdot\Bigg[&\sum_{k=1}^{k=K}[a_k(\theta_v,\varphi_v)\cdot\varepsilon_k\cdot B(T_k)]+\Delta R_{scattering}+(1-\varepsilon(\theta_v,\varphi_v)) \\ &\cdot R_{at}\downarrow\Bigg]+R_{at}(\theta_v,\varphi_v)\uparrow \end{aligned} \quad (4)$$

where k is the component index, K is the total component number, a_k is the area fraction of k component in a specific viewing direction, ε_k and T_k are the supposedly isotropic emissivity and temperature of the k component, respectively, $\Delta R_{scattering}$ is the radiance component due to mutual scattering of components, and $\varepsilon(\theta_v, \varphi_v)$ is the composite directional emissivity of a pixel which will be introduced in detail in next sub-section.

2.2. Basic definition of LSE

The emissivity at a given wavelength λ (units, μm) and temperature T (units, K), is defined as the ratio of the radiance emitted by a body at the temperature T and the radiance emitted by a black body at the same temperature T. The surface emissivity is well defined for a homogeneous surface in thermal equilibrium. However, this traditional definition will face several problems when used on non-isothermal heterogeneous scenes. Therefore, several new definitions of emissivity for any viewing direction (θ, φ) were developed to suit remote sensing applications, as listed in Table 1.

In Table 1, a_k is the area fraction of k-th component among the K components. (θ, φ) represent the view direction in zenith and azimuth. The increment $\Delta\varepsilon$ in Eq. (6) represents the interaction (i.e. multi scattering) between the components in the pixel. The temperature of k-th component is T_k. T_0 is the pixel reference temperature, and $K(T_0)$ is equal to $B'(T_0)/B(T_0)$. $f(\lambda)$ is sensor spectral response within wavelength bounded by λ_1 and λ_2. All the parameters are listed in the glossary.

It is worth mentioning that all definitions of spectral emissivity are more or less ambiguous. This arises from the fact that there are many ways for defining the two parameters (LSE and LST) from a single equation (ensemble radiance). The definition makes sense only if the defined parameters are measurable from space. The e-emissivity relies on an emission mechanism where LST derived from it changes with wavelength for nonisothermal pixel. In turn, the r-emissivity relies on reflection mechanism obeying Kirchhoff's law (Jacob et al., 2017). It remains that a precise description of the components' temperature distribution is difficult to be known. Considering this criterion, effective r-emissivity defined by Eq. (6) is particularly appropriate for LSE and LST retrievals from space measurements because it can be directly determined by the radiance measured over visible and near infrared (VNIR) spectral domain (e.g. NDVI (Valor and Caselles, 1996)).

The broadband emissivity is a critical parameter in the Earth surface radiation budget estimation and LST validation using pyrgeometer observations (Cheng and Liang, 2014). In applications, the broadband emissivity is often approximated as a linear combination of some narrowband estimate (Cheng et al., 2013; Ogawa et al., 2003; Wang et al., 2005). It should be noted that the linear equations are derived from spectral libraries and field measurements with a fixed temperature value and the land surface is assumed to be homogeneous and isothermal during the regression of coefficients.

2.3. Basic definition of LST

As for LSE, LST may also correspond to different definitions depending on the context it is being referred to Fontanilles et al. (2010). Norman and Becker (1995) provided a quite comprehensive review of the terminology used in thermal remote sensing, some of which are summarized in the sections below, such as directional radiometric temperature (DRT) and DBT, LSCT, etc.

2.3.1. Aerodynamic temperature

Aerodynamic temperature is the air temperature at the thermal roughness length. It is the physical temperature to be used with single source soil–vegetation–atmosphere transfer (SVAT) models based on excess resistance (Kustas and Anderson, 2009). It is a key parameter in models simulating land-atmosphere processes, which are relevant in numerous applications (e.g., climate, hydrology, agriculture). However, remote sensing methods cannot directly measure aerodynamic temperature. Several studies have attempted to derive relationships between aerodynamic temperature and LST which can be classified into statistical approaches (Benali et al., 2012; Cresswell et al., 1999), temperature–vegetation index approaches (Czajkowski et al., 2000; Prihodko and Goward, 1997) and energy-balance approaches (Sun et al., 2005; Zhang et al., 2015). Zakšek and Schroedter-Homscheidt (2009) reviewed the types of methods commonly used to estimate aerodynamic temperature based on LST.

2.3.2. Thermodynamic/kinetic temperature

Thermodynamic temperature is a macroscopic quantity thought to be constant throughout any group of subsystems that are in thermodynamic equilibrium, assuming therefore no heat transfer. A statistical interpretation of the thermodynamic temperature is referred to as the kinetic temperature. It is a macroscopic quantity defined on a microscopic scale in terms of the mean kinetic energy of particles. Remote sensing also cannot measure the thermodynamic or kinetic temperature directly. Instead, DRT is used as a proxy, once it is derived from the observed DBT.

2.3.3. Directional brightness temperature (DBT)

The DBT is the temperature of a black body that would have the same radiance as that actually observed from the target with the radiometer considering its sensor response function. It is a directly measured parameter in TIR remote sensing depended on the viewing angle, channel band and the sensor used. The TOA DBT and BOA DBT are widely discussed, but the TRD physical models usually aims to simulate the BOA DBT patterns.

2.3.4. Directional radiometric temperature (DRT)

The surface-leaving radiance always includes the reflected emission of atmosphere and surroundings because LSE is not unity. After the removal of reflected radiance and emissivity normalization, the DRT can be obtained. The value of DRT depends on the selected definition of LSE (Ren et al., 2014). DRT provides the best approximation for a thermodynamic/kinetic temperature based on remote sensing measurements. DRT is the quantity to estimate from satellite observations in the domain of LST inversions.

2.3.5. Land surface component temperature (LSCT)

Soil and vegetation temperatures are input variables of two-source SVAT models (Kustas and Anderson, 2009). They correspond to kinetic or radiometric temperatures. Several studies have focused on methodologies to derive the temperature of such components, e.g., by separating the sunlit soil temperature and shaded soil temperature (Bian et al., 2016), and distinguishing the sunlit leaf and shaded leaf temperatures (Timmermans et al., 2009). Canopy temperature profiles from the soil surface to the top of canopy are considered in some models (van der Tol et al., 2009), which may be determined through inversion techniques if the appropriate DBT observations are available (Kimes, 1981).

2.4. Ways to describe TRD

There are 14 methods for describing TRD in models, as indicated by

Table 2
Fourteen methods for describing TRD effect.

ID	Quantity	Physical meaning
1	$\varepsilon(\theta_v, \varphi_v)$	Absolute directional emissivity
2	$B^{-1}(I_{outgoing}(\theta_v, \varphi_v))$	BOA DBT
3	$T(\theta_v, \varphi_v)$	DRT
4	$\varepsilon(\theta_v, \varphi_v)/\varepsilon(0, 0)$	Relative directional emissivity
5	$B^{-1}(I_{outgoing}(\theta_v, \varphi_v))/B^{-1}(I_{outgoing}(0, 0))$	Ratio of off-nadir to nadir DBT
6	$T(\theta_v, \varphi_v)/T(0, 0)$	Ratio of off-nadir to nadir DRT
7	$B^{-1}(I_{outgoing}(\theta_v, \varphi_v))$-$B^{-1}(I_{outgoing}(0, 0))$	Difference between off-nadir and nadir DBT
8	$T(\theta_v, \varphi_v)$-$T(0, 0)$	Difference between off-nadir and nadir DRT
9	DBT_{max}-DBT_{min}	Difference between maximum and minimum DBT
10	DBT_{max}-DBT_{nadir}	Difference between maximum and nadir DBT
11	DBT_{nadir}-DBT_{min}	Difference between nadir and minimum DBT
12	*DBT_55_AVE*	Average of the DBT values for all VAA directions with VZA equal to 55°
13	*DBT_55_STD*	Standard deviation of the DBT values for all VAA directions with VZA equal to 55°
14	*DBT_SPP_STD*	Standard deviation of DBT values in the solar principal plane for VZA within [−50°, +50°] range

Table 3
List of main TRD measurement for homogeneous samples.

Surface type	VZA	TRD amplitude (relative emissivity, the 4th quantity in Table 2)	Authors and year
Ice	0°-65°	10%	Rees and James, 1992
Water	0°-65°	7%	Cuenca and Sobrino, 2004; Masuda et al., 1988; Rees and James, 1992; Sobrino and Cuenca, 1999
Coarse grain snow	0°-70°	4.5–6.8%	Hori et al., 2006
Agricultural soils	0°-70°	3–9%	Labed and Stoll, 1991
Sand	0°-70°	3%	Cuenca and Sobrino, 2004; Labed and Stoll, 1991; Sobrino and Cuenca, 1999
Slime, Gravel	0°-65°	2%	Cuenca and Sobrino, 2004; Sobrino and Cuenca, 1999
Clay	0°-65°	1%	Cuenca and Sobrino, 2004; Sobrino and Cuenca, 1999
Silt-loam	0°-65°	1%	Snyder et al., 1997

the quantities shown in Table 2. The most widely used is BOA DBT (quantity 2 in Table 2) because it can be easily obtained after applying atmospheric correction and the inverse Planck function to satellite or airborne observations (Cao et al., 2015). If the absolute directional emissivity and the downward atmospheric radiance are known, the DRT (quantity 3) can be further obtained to describe the TRD effect. For example, the DRT is considered in the process of LST product angular normalization (Ren et al., 2014). A homogeneous scene, such as one of water, snow or soil, is always treated as an isothermal surface, thus its TRD is always attributed to the absolute directional emissivity. Therefore, quantity 1 in Table 2 is also used to describe TRD (Sobrino and Cuenca, 1999).

Errors of absolute values are usually restrained by using quantities such as the ratio of off-nadir to nadir absolute emissivities (quantity 4) (Sobrino and Cuenca, 1999; Sun et al., 2015), the ratio of off-nadir to nadir DBT (quantity 5) and the ratio of off-nadir to nadir DRT (quantity 6) (Vinnikov et al., 2012). In addition, the difference between off-nadir and nadir DBT/DRT (quantity 7/8) is usually defined as directional anisotropy to express the TRD effect. It is widely used in urban TRD modeling studies (Lagouarde et al., 2010). Another advantage of quantities 5–8 is that they can be used to describe the TRD pattern which can be further assumed steady within a time period. This will benefit to the multi-angle dataset construction. All quantities 1–8 have different values in different directions.

In addition, six indicators were proposed to describe the TRD effect with a unique value for one scene, including the difference between maximum and minimum DBT (DBT_{max}-DBT_{min}, Cao et al., 2019), the difference between maximum and nadir DBT (DBT_{max}-DBT_{nadir}, Bian et al., 2018), the difference between nadir and minimum DBT (DBT_{nadir}-DBT_{min}, Chehbouni et al., 2001), the average of the DBT values for all VAA directions with a 55° VZA (*DBT_55_AVE*, Huang et al., 2011), the standard deviation of the DBT values for all VAA directions with a 55° VZA (*DBT_55_STD*, Huang et al., 2011) and the standard deviation of DBT values in the solar principal plane for VZA within [−50°, +50°] range (*DBT_SPP_STD*, Duffour et al., 2016a).

3. TRD measurement and observation

Multi-scale measurements and observations were performed over homogeneous and heterogeneous scenes, including a laboratory measurement of one sample, in-situ measurements of possibly mixed samples, airborne observations of a patchwork of different objects and satellite observations of a patchwork of different areas.

The characterization and evidence of the TRD phenomenon have been originally reported from ground measurements (Monteith and Szeicz, 1962; Sutherland and Bartholic, 1977). Later, the impact of TRD was studied in the laboratory by measuring temperature and emissivity properties of homogeneous samples (Labed and Stoll, 1991; Snyder et al., 1997). Usually, the directionality of homogeneous surfaces is attributable to the emissivity. Since 2000, equipment and facilities with more view angles and better efficiency have been developed to obtain in-situ multi angle datasets over heterogeneous vegetated landscapes (Li et al., 2004). For TRD observations over urban canopy, a scientific protocol of airborne measurements was proposed to overcome the footprint limitation of ground measurement equipment (Lagouarde et al., 2004). Multi-angle datasets of vegetation and urban canopies were obtained with a trade-off between viewing angles and time-consumption of the experiments. ATSR series are space-borne sensors offering more variability in viewing angles (the same scene is sampled at 0° and 55°) in the TIR band, and are reliable data sources for studying the effects of TRD at the satellite scale, although caution must be taken concerning the small differences in the dual-view observation times. Recently, Hu et al. (2016a) presented a first satellite-based assessment of urban TRD (> 10 K) using ten years of the MODIS LST product. Equally high values were reported over other types of surfaces, especially in moderately vegetated areas (Ermida et al., 2014; Guillevic et al., 2013). In this section, the main TRD measurements obtained from laboratory, field, aircraft and satellite are summarized.

3.1. Laboratory and in-situ measurements of homogeneous samples

TRD effects have been reported for both heterogeneous (such as wheat, cotton, and sunflower crops) and homogeneous surfaces (such as water, snow and soil). The latter are attributed to the sample emissivity properties. The early works that measured the TRD in the laboratory can be divided into two categories. One focused on the creation of spectral libraries of emissivity, such as the UCSB MODIS library (Snyder et al., 1997) and USGS ASTER library (Salisbury et al., 1994), and the other focused on the determination of emissivity properties for accurate estimation of LST, taking into account the TRD effect of emissivity (Sobrino and Cuenca, 1999). Table 3 lists the main TRD measurements collected in laboratory and in-situ conditions for homogeneous samples, including soil, sand, snow, water and ice. In this table, the relative directional emissivity (i.e. the 4th quantity in Table 2) is used to describe the TRD effect amplitude. This is defined as the ratio of off-nadir to nadir emissivities. The maximum relative directional emissivity is equal to one appearing in the nadir. There are different degrees of decreases in the oblique directions for different surfaces as shown in Table 3. Results show that ice, water, snow and agricultural soils have significant TRD effects while least effects arise for slime, gravel, clay and silt-loam. The TRD amplitude of sand is between agricultural soils and clay (about 3% of decrease from 0° to 70°). Some of the measurements (e.g. Cuenca and Sobrino, 2004; Hori et al., 2006; Sobrino and Cuenca, 1999) were performed outside of the laboratory, and other measurements were obtained in laboratory.

3.2. In-situ measurements

The main difficulty of in-situ measurements is in making observations of multiple viewing geometries during a time period short enough (usually < < 30 min) such that temperature changes can be neglected. In this section, we provide a summary of well-documented in-situ TRD

Table 4
List of the typical in-situ TRD measurements. The (*), (&) and (#) in the sixth column represent the 9th, 10th, and 11th quantities in Table 2 respectively. They are used to show the measured in-situ TRD amplitude over soils or vegetations. Worth outlining here that the sensor used in Monteith and Szeicz (1962) is a Linke-Feussner pyrheliometer with a quartz filter.

Earth surface	Height /LAI	Sensor FOV	Sensor wavelength	Sensor VZA	TRD amplitude	Authors and year
Grass	0.25 m	10°	> 3 μm	0°-80°	3 K (*)	Monteith and Szeicz, 1962
Semiarid grass	–	15°/60°	8–14 μm	0°-55°	5 K (#)	Chehbouni et al., 2001
Sudan grass	–	7°, 30°	8–13 μm	15°-75°	0.6 K (*)	Fuchs et al., 1967
Alfalfa	–	7°, 30°	8–13 μm	15°-75°	1.8 K (*)	Fuchs et al., 1967
Soybeans	–	7°, 30°	8–13 μm	15°-60°	1.7 K (*)	Fuchs et al., 1967
Soybeans	–	5°	10.5–12.5 μm	0°-75°	1.5 K (*)	Nielsen et al., 1984
Wheat	0.53 m	4°	10.5–12.5 μm	0°-80°	13 K (#)	Kimes et al., 1980
Cotton rows	0.55 m	15°	8–14 μm	0°-80°	16.2 K (#)	Kimes and Kirchner, 1983
Sunflower	1.5 m	4°	8–14 μm	0°-90°	9.3 K (*)	Paw et al., 1989
Leafless forest	21.5 m	2°	8–12 μm	0°-70°	8 K (*)	Balick and Hutchinson, 1986
Oak-hickory forest	21.5 m	2°; 3°	8–12 μm	10°-85°	3.2 K (*)	McGuire et al., 1989
Corn	1.1 m	5°	8–14 μm	0°-60°	4 K (#)	Lagouarde et al., 1995
Ploughed soil	0.25 m	35°	8–14 μm	0°-60°	3.5 K (&)	Lagouarde et al., 1995
Furrowed soil	0.08 m	5°	8–14 μm	0°-60°	5 K (#)	Verbrugghe and Cierniewski, 1998
Coarse rough soil	0.055 m	18° × 24°	8–13 μm	0°-70°	4 K (#)	Li et al., 2004
Wheat	LAI = 1.5	18° × 24°	8–13 μm	0°-70°	5.5 K (#)	Li et al., 2004
Wheat	LAI = 4.1	18° × 24°	7.5–13.5 μm	0°-60°	3 K (*)	Du et al., 2007
Corn	H = 2.2 m	28°	8–14 μm	0°-60°	6.5 K (*)	Ren et al., 2013
Corn	LAI = 1.2	54° × 68°	7.5–14 μm	0°-50°	4 K (&)	Bian et al., 2018

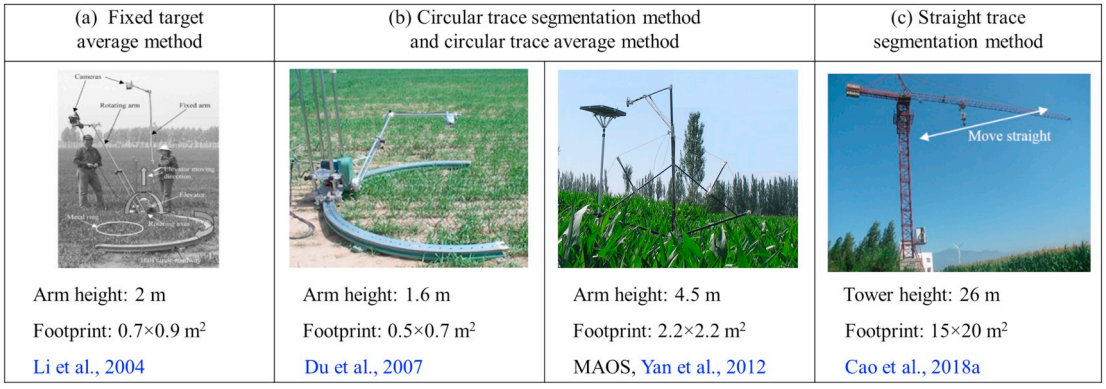

Fig. 1. Information of four kinds of ground-based multi-angle measurement protocols.

measurements (see Table 4). They show that the TRD amplitude for heterogeneous surfaces (cotton, wheat, sunflower, forest, corn and furrowed soil) is significantly larger than that of homogeneous surfaces, such as grass and soybeans. In order to obtain directional measurements, most of the radiometers in Table 4 have narrow field-of-view (FOV). Furthermore, four kinds of measurement protocols (see Fig. 1) are introduced, including circular trace average method, fixed target average method, circular trace segmentation method and straight trace segmentation method.

In the very first experiments, ground-based multi-angle observation systems were implemented manually. Data were acquired by rotating the arm of the goniometer on which the TIR radiometer was fixed to change the viewing zenith angle (Barton and Takashima, 1986; Lagouarde et al., 1995) and by moving along a track of the goniometer to change the view azimuth angle (VAA). Then, the TIR data acquired in a certain view angle was usually averaged to represent the directional emission of the scene in this view direction (we call it as circular trace average method). To increase the automation and speed of measurement acquisition, Yan et al. (2012) developed a portable Multi-Angle Observation System (MAOS) which can provide the bi-directional reflectance factor (BRF) and DBT distributions concomitantly. As shown in Fig. 1b, it is composed by a spectroradiometer (FOV = 25°), a TIR radiometer (FOV = 28°), a video camera and a two-dimension automatic goniometer. The improved system is able to make > 13 zenith measurements in 6 min at an arbitrary azimuth direction.

The circular trace average method observes different areas in different viewing directions which may reduce the quality of the measurement dataset (Zhang et al., 2000). Therefore, Li et al. (2004) designed an automated system to improve the accuracy of TIR measurements consisting of two identical thermal cameras and a metal ring to fix the view areas for different viewing directions (we call it the fixed target average method). As shown in Fig. 1a, it is composed of: (1) a semicircular roadway of 2 m diameter; (2) an elevator of 1 m height; (3) a 2 m rotating arm equipped with one thermal camera for changing the view zenith angle (VZA); and (4) a fixed arm equipped with another thermal camera to record the target nadir temperature variation with time during the measurements. The pixels within the metal ring of thermal camera image were extracted and averaged to ensure the area of research target is fixed. The system needs only 2 min to make directional measurements from about −70° to 70° for a given azimuth. For completing one hemispheric measurement, it needs about 20 min if the multidirectional measurements are conducted with a 30° interval in the azimuth direction.

Measurements with the circular trace average method and fixed target average method are influenced by the radiometer FOV. In order to reduce this effect, which means different pixels have different specific view angles. Du et al. (2007) segmented the observed TIR images into small images with narrow FOV according to the VZA and VAA values (we call it the circular trace segmentation method). The observation protocol is the same as the circular trace average method.

However, the process of averaging is changed to segmentation with a critical sector size. Time normalization was done using nadir data of different azimuthal plane observations. Indeed, as shown in Fig. 1b, no TIR camera was fixed in the nadir direction to correct the time shift of temperature.

All the above three protocols are limited by the viewing footprint which is smaller than 2.5 × 2.5 m^2. Cao et al. (2018a) mounted the TIR camera on a tower to overcome this problem during experiments (see Fig. 1c). A tower crane was constructed for near-surface observations with height ranging from 1.0 m to 26 m above the ground (the target size is 15 m × 20 m when the height is 15 m). The directional radiance of the TIR band can cover −1° to 53° using an oblique FLIR 655sc camera with a FOV equal to 54° × 68° and an oblique angle equal to 26°. The tower can move straight on the slideway and a turntable device changes the observation azimuth. The high frequency of the sensors is aimed at acquiring datasets with a high overlap rate to extract multi-angle values. It provides the spatio-temporal averaged result of different directions by segmenting the acquired images into small sectors according to the viewing angles (we call this the straight trace segmentation method). The information extraction method is similar to the circular trace segmentation method. However, their observation protocols are different. In addition, this system also can also observe the BRF as MAOS.

3.3. Airborne observations

The ground measurements are limited by the target spatial size and the target height. For example, it is difficult to observe TRD variations of forest and urban canopies using ground measurements. This explains the development of airborne observation approaches, including the cross track and parallel track protocols.

Lagouarde et al. (2014, 2000) extracted the DBT TRD of pine forest and row-planted vineyards using a thermal camera (INFRAMETRICS Model 760) mounted on a small aircraft at an oblique angle of 20°. They extracted DBT with VZA up to 60° from nearly half hour of observations with four pairs of cross flight lines in opposite directions (Fig. 2a-b). The lines contain the solar principal plane, the cross solar principal plane and two transitional planes. In this type of experiments, the target area must be large enough to be representative of the considered landscape. Then, the spatio-temporal averaged multi-angle DBT dataset can be obtained after sensor calibration, lens distortion correction, geometric correction, viewing angle retrieval, and atmospheric correction. Such experiments were also carried out over the cities of Marseille and Toulouse (Lagouarde et al., 2012, 2010, 2004) with observed maximum TRD effect of 7 K and 10 K, respectively. Voogt and Oke (1998) used a helicopter to assess quantitatively the magnitude of TRD in different districts of the city of Vancouver. The results stressed strong TRD effects in all urban zones with a maximum value of 9 K over the high-rise downtown area near midday. The results illustrate that the DRT of urban areas is closely related to the sun-surface-sensor geometry. Compared to the hypothesis of isotropic brightness temperatures, the actual brightness temperature anisotropy leads to a very different upward longwave radiation. Sugawara and Takamura (2006) found that the TRD effect leads to about 8% error in the urban SULR estimates based on the airborne observations over Sapporo and Tokyo.

Liu et al. (2012) carried out multi-angle observations over key experimental areas of the middle reaches of the WATER (Li et al., 2009) and HiWATER (Li et al., 2013c) comprehensive experiments. They used the airborne Wide-angle Infrared Dual-mode line/area Array Scanner (WiDAS) in WATER and HiWATER which was developed on the basis of Airborne Multi-angular TIR/VNIR Imaging System (AMTIS) (Fan et al., 2004). A thermal infrared camera (FLIR A655sc), equipped with 68° × 54° wide-angle FOV lens, was placed aboard the aircraft with a forward inclination of 12°. The flight protocol consisted of several long parallel flight lines that were flown in opposite directions (Fig. 2c). One track in one direction took about 4 min, and the turning took about 4 min. The overlap between two sequential WiDAS images is larger than 85% in the TIR band, indicating that the same ground point can be almost simultaneously observed in several sequential images, as shown in Fig. 2d. They extracted 15 observations with different viewing angles (from −50° to +20° with a step equal to 5°) in one track. The TIR images were resampled to 5 m spatial resolution after the preprocessing steps. Observations with a wide VZA range can be obtained for target areas close to the track line center. Until now, these datasets were not used to produce hemispherical DBT distribution due to the relatively long time interval between adjacent tracks. The airborne multi angle observations of a single flight were used for LSCT estimation studies (Bian et al., 2016; Liu et al., 2012).

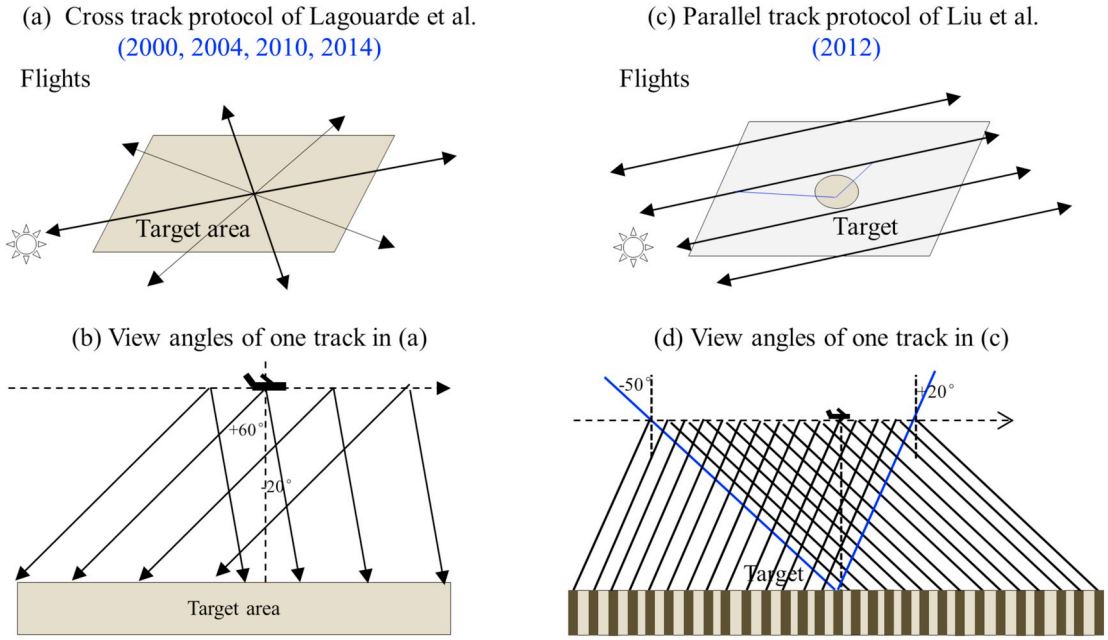

Fig. 2. Protocols of two kinds of airborne multi angle observations.

Table 5
Main parameters of ATSR, ATSR2, AATSR and SLSTR.

Sensor	Satellite	Year	Bands and nadir spatial resolution	Swath
ATSR	ERS-1	1991–2000	(1.613; 3.742; 10.85; 12.02) 1 km	500 km
ATSR2	ERS-2	1995–2011	(0.554; 0.659; 0.868; 1.613; 3.742; 10.85; 12.02) 1 km	500 km
AATSR	ENVISAT	2002–2012	(0.554; 0.659; 0.868; 1.613; 3.742; 10.85; 12.02) 1 km	500 km
SLSTR	SENTINEL-3	2016-	(0.554; 0.659; 0.868 1.374; 1.613; 2.25) 500 m; (3.742; 10.85; 12.02) 1 km	> 1400 km (Nadir)

3.4. Space borne observations

Only the ATSR series of sensors (ATSR, ATSR2, AATSR, SLSTR) can supply near-simultaneous observations at different angles (0° and 55°) (Ghent et al., 2017). Their characteristics (spectral bands, spatial resolution, swath and working time) are summarized in Table 5. Compared to ATSR, the ATSR-2 and AATSR have three additional bands in the visible and near infrared domains for vegetation monitoring. Two more channels were added in SLSTR for cloud detection. In addition, the spatial resolution of the VNIR and shortwave infrared bands of SLSTR were enhanced to 500 m from 1 km in the past. A conical scan was used to give a dual directional viewing of the Earth's surface for these sensors. Coll et al. (2019) extracted the BOA DBT difference between the nadir observation and the forward observation using an automated, pixel-by-pixel atmospheric correction method and found that the maximum difference can be up to 8 K for sparsely vegetated land surface (LAI ranging from 0.5 to 2.0) during summer whereas the difference of over sea water surfaces was uniform and independent on the season, with an average of about 0.7 K.

Other TIR sensors onboard polar orbiting satellites do not have near-simultaneous two-angle observations as ATSR series. More information about them can be found in Jacob et al. (2008). Their maximum VZA can be up to 60° due to their FOV scanning and the Earth's curvature. The VZA and VAA over a single pixel in certain locations change depending on day of the observation. Fig. 3a shows the daytime viewing angles of Terra MODIS and Aqua MODIS over a year (2012) for the HiWATER superstation (Li et al., 2013c). For geostationary satellites, the viewing angle of each pixel is fixed. The VZA of a pixel located on the edge of the image will be over 60° with a footprint that is much larger compared to central pixels as shown in Fig. 3b (Rasmussen et al., 2011, 2010). On the other hand, the illumination geometry, solar zenith angle (SZA, θ_s) and solar azimuth angle (SAA, φ_s), change both during the day and seasonally for geostationary satellites and the virtual constellation of these can supply a series of multi-angle observations within a limited time interval (Minnis and Khaiyer, 2000). Therefore, both the polar orbiting and geostationary satellites are influenced by the TRD effect. They can also be used as a data source of TRD empirical modeling.

For MODIS, besides the LST products of split window algorithm (Wan and Dozier, 1996), the day/night algorithm (Wan and Li, 1997) and the TES algorithm (Malakar and Hulley, 2016) are regularly used to generate LST and LSE products simultaneously. Ren et al. (2011) generated the empirical relationships between the directional emissivity, land cover, and seasonal variations by performing a statistical analysis of 5-year MOD11B1 emissivity products. They found that the emissivities increased with increase of VZA in the MODIS MIR bands and decreased in the TIR bands with angular variation of emissivity around 0.01–0.02. Hu et al. (2019) did a similar work based on MYD21 products and found that the angular variation of directional emissivity in Band 29 (8.55 μm) could reach up to 0.03, but was < 0.01 for Bands 31 (11 μm) and 32 (12 μm). García-Santos et al. (2015) obtained the LSE dependence on VZA over arid regions based on simulated MOD21 products. Results showed that band 29 LSE decreased by up to 0.038 from nadir to a zenith angle of 60°, whereas LSEs for bands 31 and 32 did not show significant variation.

4. TRD modeling over Earth surface

Atmospheric effects can be considered rather accurately using atmospheric codes such as MODTRAN (Berk et al., 2005), provided the input data are well known. Therefore, most TRD models were developed at the BOA level to simulate the $I_{outgoing}(\theta v, \varphi v)$ or $B^{-1}(I_{outgoing}(\theta v, \varphi v))$ patterns of Earth surface. For homogeneous surfaces, such as water, ice, sea, snow and soil, the TRD effect is always attributed to the emissivity. Therefore, TRD models were developed to simulate the $\varepsilon(\theta v, \varphi v)$ patterns for them. The existing TRD models can be classified into five classes: radiative transfer models (RTM), geometric optical models (GOM), hybrid models (HM), 3D models and parametric models (PM). Table 6 summarized the typical models of different surfaces. A review of the 70 TRD models will be introduced one by one below. The 9 models underlined in Table 6 (Cupid, SCOPE, THERMO, TRGMEB, BAI2016, DARTEB, SEB, TUF-3D, SOLENE) are radiative transfer models coupled with an energy budget module to generate the component temperature via an iterative process. Most TRD models were not

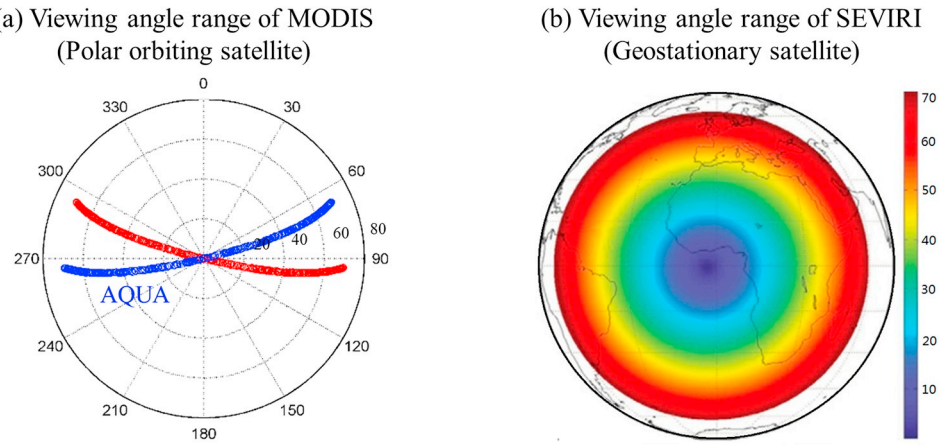

Fig. 3. Viewing angle ranges of typical polar orbiting and geostationary satellites.

Table 6
Models classification for different surface types.

	RTM	GOM	HM	3D model	PM
Inland Water/Ice	• MAS1988	–	–	–	–
Sea	–	• MAS1988 • WU1997 • MAS2006 • BOU2006 • LI2011A • LI2011B • LI2013 • LI2012 • LI2014 • CHE2017	–	HEN2003	–
Snow	• Mie/DW • WAL1994 • MIS1997 • Mie/Conel • Mie/Hapke • Mie/DISORT • HOR2013	–	–	–	–
Sand/soil	• HAP1981 • BEK1985 • HAP1993 • Mie/Hapke • Mie/Conel • Mie/DISORT • Mie/DW • T-matrix/Conel • T-matrix/Hapke	• VER1998	–	–	• NER1991 • GAR2012
Continuous Vegetation	• KIM1980 • PRE1985 • FRA1997 • FRA2002 • SAIL-Thermique • TSAIL • 4SAIL • Cupid • SCOPE • REN2015 • CE-P	–	–	• THERMO • XU2002 • Extended-DART • TRGM • TRGMEB • BAI2016	• LSF-LI • ROSS-LI • VIN2012 • RL • VIN2012-RL
Row-planted vegetation	–	• SUT1977 • JAC1979 • KIM1983 • CAS1989 • SOB1990	• CHE2002 • YAN2003 • YU2004 • SLEC • Fovmod		
Discrete vegetation	–	• MGP	–		
Urban	–	–	–	• SUM • SUMVEG • LAG2000 • TITAN • Extended-DART • DARTEB • SEB • TUF-3D • SOLENE	• VIN2012 • USEA • RL • GUTA-sparse • GUTA-osg

named. For the sake of simplification, the first three characters of the surname of the first author and the year of publication were combined to refer to them.

4.1. TRD modeling over water bodies, ice and sea

Inland water bodies are always treated as specular surfaces. Their directional emissivity can be calculated by Fresnel's and Snell's laws if they are assumed to be homogeneous with plane surfaces and the imaginary parts of their refractive indices are neglected. Rees and James (1992) suggested a refractive index of l.43 ± 0.03 for water in TIR band. Then, the simulated water emissivity is equal to 0.969 ± 0.003 and 0.893 ± 0.06 for nadir and 65° oblique viewing direction, respectively. The Fresnel's law (Eq. (12)) and Snell's law (Eq. (13)) are shown below where the θ_{in} is the incident angle, θ_{out} is the refractive angle and n is the refractive index (Masuda et al., 1988). Eqs. (12)–(13) show that the larger the refractive index, the smaller the emissivity value. For ice specular surfaces, the directional emissivity can be calculated by Fresnel theory and Snell's law as water with a larger refractive index (1.60 ± 0.09) suggested by Rees and James (1992). Then, the simulated nadir emissivity and emissivity of 65° equal to 0.947 ± 0.012 and 0.863 ± 0.015, respectively, which is always smaller than that of a water surface.

$$\varepsilon(\theta_{in}) = 1 - \frac{1}{2}\cdot\left[\left(\frac{n\cos\theta_{in} - \cos\theta_{out}}{n\cos\theta_{in} + \cos\theta_{out}}\right)^2 + \left(\frac{\cos\theta_{in} - n\cos\theta_{out}}{\cos\theta_{in} + n\cos\theta_{out}}\right)^2\right] \quad (12)$$

$$\sin\theta_{out} = (1/n)\sin\theta_{in} \quad (13)$$

The uncertainty of sea surface emissivity must be within 0.005 in the TIR domain in order to obtain SST with an error < 0.3 K (Wu and Smith, 1997). The main differences between sea and inland water bodies include the surface roughness caused by the wind, and the

Table 7
List of typical water/sea TRD models. Here, and in subsequent tables describing existing models, we also include the models' main features, most relevant publication and the citation number at the moment of writing this article to indicate their usage in general.

Name	Authors	Year	Main features	Basic model	Cited time
MAS1988	Masuda et al.	1988	Considering surface roughness, no scattering	Cox-Munk	493
WU1997	Wu and Smith	1997	Considering scattering using a specific cutoff angle	MAS1988	212
HEN2003	Henderson et al.	2003	A Monte Carlo ray-tracing model considering polarization	Monte Carlo	67
MAS2006	Masuda	2006	Considering scattering using a wind speed dependent weighting function	WU1997	49
BOU2006	Bourlier	2006	Considering scattering using a statistical illumination function	MAS1988	14
LI2011A	Li et al.	2011	Calculate first-order scattering by a monostatic statistical illumination function	Smith illumination function	13
LI2011B	Li et al.	2011	Considering polarization and first-order scattering	LI2011A; BOU2006	14
LI2013	Li et al.	2013	Considering polarization and second-order scattering	LI2011B	6
LI2012	Li et al.	2012	Considering polarization, first-order scattering and non-Gaussian surface slope distribution	LI2011B	9
LI2014	Li et al.	2014	Considering polarization, second-order scattering and non-Gaussian surface slope distribution	LI2012 LI2013	4
CHE2017	Cheng et al.	2017	Considering foam cover	WU1997	1

whitecaps resulting from wave-breaking at the crest. In addition, the temperature and salinity dependence should be considered in sea surface emissivity modeling (Embury et al., 2012). According to Cox and Munk (1954), the facet slope distribution of a wind-roughened sea surface can be approximately normal and isotropic with a Gaussian probability density function. However, until now, only a few studies have investigated the effects of foam and whitecaps on the simulation in the TIR band (Branch et al., 2016; Cheng et al., 2017). Measurements show that foam can reduce the angular variation of sea surface emissivity up to 0.04 for VZA equal to 65° (Niclòs et al., 2007). Typical models of sea surface emissivity are listed in Table 7.

The pioneering modeling work for sea surface was conducted by Masuda et al. (1988). They designed the MAS1988 emissivity model by coupling the Cox-Munk function and the Fresnel's law of specular water surface. Then, a directional emissivity look-up-table (LUT) for water and sea surface with different wind speeds (< 15 m/s) was generated and widely used. Results show that the relative difference of emissivities between pure water and sea water is < 0.1% for VZA < 50° for wind speed < 15 m/s. François and Ottlé (1994) validated the simulated emissivity of MAS1988 model ranging in 52°–55° by the retrieved emissivity from ATSR.

Smith et al. (1996) measured the sea surface emissivity with different wind speeds and compared it with the simulated result of Masuda et al. They found that the emissivity computed by MAS1988 is smaller than that observed for view angles larger than 60°. In order to improve this situation, Wu and Smith (1997) designed an improved model that considers the surface-reflected surface-emission based on the modeling works of Watts et al. (1996). In addition, the improved model showed that the computed sea surface emissivity is only weakly dependent on wind speed for most view angles (< 60°) used in practice. This is because the roughness structure tends to reduce the direct emission and to increase the surface-reflected emission for small to moderate view angles. Niclos et al. (2005) measured sea radiance of four channels within the 8–14 μm region using the CIMEL CE-312 radiometer in five directions (25°, 35°, 45°, 55°, 65°) and at two wind speeds (4.5 m/s and 10.3 m/s). They confirmed the advantage of the WU1997 model for simulating sea surface emissivity for observation angles larger than 50°, compared to MAS1988 model.

In the WU1997 model, a specific cutoff angle was introduced to distinguish the sea leaving radiation and the sky radiation, for calculating surface-reflected emission. However, using the ambiguous cutoff angle, the dependence of the probability function on a surface wind speed cannot be taken into account. Masuda (2006) overcame this issue by using a weighting function which is expressed as a function of the surface wind speed by way of the probability distribution function of sea surface slope. They proved that a difference of 5° in cutoff angle causes the surface-reflected emission fluctuation approximately by 0.01 ~ 0.02 for VZA equal to 75°. The MAS2006 model was simplified into a fifth degree polynomial fitting model, referred to as SEMIS (Islam et al., 2016).

Bourlier (2006) developed a statistical illumination function instead of the weighting function of MAS2006 to calculate surface reflections. To overcome the significant overestimation (underestimation) of first-order reflection of MAS2006 (BOU2006) model when taking the Monte Carlo ray-tracing sea emissivity model (Henderson et al., 2003) as reference, Li et al. (2011a) developed a unpolarized emissivity model with first-order reflection based on Smith illumination function (Smith, 1967) and further a polarized emissivity model with first-order reflection (Li et al., 2011b) based on LI2011A and BOU2006 models. Then, a polarized emissivity model with second-order reflection was considered by introducing an improved bistatic illumination function (Li et al., 2013b) based on LI2011B. LI2011B and LI2013 models are only suitable for the one-dimensional sea surface. They were extended into two-dimensional versions (3D problems) in 2012 and 2014, respectively (Li et al., 2012; Li et al., 2014a) to model real sea surface conditions.

4.2. TRD modeling over snow surface

According to (Hori et al., 2006), snow can be divided into five types according to the snow particle radius: frost, fine new dendrite snow, medium granular snow, coarse granular/grain snow and welded sun crust snow. Keck et al. (2017) proposed a method for retrieving these snow/ice types by remotely sensed spectral and directional emissivity from AATSR. In general, snow particles are expressed as aggregated ice crystals. Emissivity modeling of snow is similar to that of soil. However, the texture and roughness are simpler. As demonstrated by Hulst (1957), the distances between neighboring particles must be at least three particle radii for the independent scattering approximation to be valid. This requirement is not met in most cases. Therefore, the main difficulty in modeling is in calculating the scattering efficiency of a single particle of close-packed snow. The typical TRD models of snow are listed in Table 8.

The pioneering work was performed by Dozier and Warren (1982) who proposed a DBT model (Mie/DW model) of snow surfaces with Mie scattering theory for single scattering and delta-Eddington approximation for single scattering albedo (ω) and asymmetry factor (g) based on the snow albedo model in the solar spectrum (Wiscombe and Warren, 1980). The directional-hemispheric reflectance was converted to directional emissivity (corresponding to r-emissivity) via Kirchhoff's law. Simulation results showed that the directional emissivity has a significant angular dependence which will produce differences between thermodynamic temperature and brightness temperature as large as 3 K at wavelengths 12–14 μm when VZA equals to 75° but < 0.5 K in the nadir direction.

In the Mie theory, all types of photo-particle interactions such as reflection, refraction and diffraction are included. However, Wald

Table 8
List of typical snow TRD models, as in Table 7.

Name	Authors	Year	Main features	Basic model	Cited time
Mie/DW	Dozier and Warren	1982	Mie scattering theory for single scattering and delta-Eddington approximation for single scattering albedo ω and asymmetry factor g	Snow albedo model in the solar spectrum	273
WAL1994	Wald	1994	Employing the diffraction subtraction method to improve Mie scattering for close-packed snow	Mie/DW	54
MIS1997	Mishchenko and Macke	1997	Employing the static structure factor to improve Mie scattering for close-packed particles	Mie/DW	112
Mie/Conel	Cheng et al	2010	Mie scattering theory for single scattering and a two-stream approximation for multiple scattering	A cloudy atmosphere model	28
Mie/Hapke	Cheng et al.	2010	Mie scattering theory for single scattering and Hapke model for multiple scattering	Hapke emission theory	28
Mie/DISORT	Cheng et al.	2010	Mie scattering theory for single scattering and DISORT model for multiple scattering	DISORT	28
HOR2013	Hori et al.	2013	A linear combination of specular and blackbody surfaces' emissivities with a weighting parameter	WAL1994	16

(1994) found that these phenomena are dependent for media with close-packed particles. Then he proposed a term of "diffraction subtraction" to modify the scattering cross section of close-packed large opaque spheres to account for the effect of close packing on the diffraction cross section of a scattering particle. Besides the diffraction subtraction solution, Mishchenko and Macke (1997) developed a static structure factor correction to simulate the asymmetry parameters of the phase function for isolated and densely packed composite spherical particles. Both the diffraction subtraction and static structure factor correction were widely used in snow emissivity modeling.

Cheng et al. (2010b) combined the Mie scattering theory for single scattering and three different solutions for multiple scattering (Conel model, Hapke model and DISORT model). They further cross-compared the combined models with Mie/DW through in-situ measurement of Hori et al. (2006). They found that only the Mie/DW cannot simulate the emissivity dependence of the particle radii and all four models are not accurate enough because of the assumption of independence between particles. After having corrected the Mie scattering component of close-packed particles, the Mie-corrected/Hapke model was found to perform the best to mimic the snow directional emissivity, with a RMSE < 0.009 in the 8–11 μm spectral region. The role of diffraction subtraction and static structure factor correction in improving the modeling was clearly confirmed.

To improve the accuracy of the angular dependence of emissivity spectra for different snow and ice types. Hori et al. (2013) proposed a semi-empirical model with a weighted sum of two emissivity components: one each for specular and blackbody surfaces. The calibrated weighting parameters (effective areal fraction of specular surface) for fine new dendrite snow, medium granular snow, coarse granular/grain snow, welded sun crust snow and bare glaze ice are equal to 0.22, 0.29, 0.41, 0.53 and 0.95, respectively. This model was used to improve the retrieval of mountain glacier surface temperatures from Landsat-ETM + TIR observations (Wu et al., 2015).

4.3. TRD modeling over barren lands

Most barren lands are pure soil surfaces. Several measurements showed that soil emissivity is angular dependent as introduced in Table 1. Ignoring its angular effects will lead to ± 0.4 to about ± 1.3 K error in estimated LST from the split window algorithm and a further 2% to 8% error to the estimated SULR (Garcia-Santos et al., 2012). Labed and Stoll (1991) found that directional dependence of soil emissivity arises from geometrical effects of grain size, roughness and porosity. Table 9 lists the typical soil TRD models. Some of them were initially proposed to simulate the directional emissivity of mineral samples (such as quartz, gypsum, enstatite) rather than exactly soil samples.

There exist two empirical models for directional soil emissivity simulation. The first one was proposed by Nerry et al. (1991) based on the assumption of totally incoherent scattering by a rough medium at 10.6 μm accounting for slope distribution and shadowing effects. However, the backscattered peak was not yet addressed, which limited its wide usage. Garcia-Santos et al. (2012) measured 12 inorganic bare soil samples to obtain a more powerful empirical relationship between the emissivity and view angle, sand and clay percentage. Their particles sizes are limited to 0.2–1 cm to achieve a low roughness. Results show that emissivity of all samples studied is almost isotropic in azimuth and also in zenith, up to VZA = 40°. This decrease of emissivity with larger VZA is most pronounced in sandy soil, while clayey samples did not show a significant decrease.

Two physical models were proposed based on Hapke's reflectance theory and Hapke's emission theory to simulate soil directional emissivity. For the first one (HAP1981 (Hapke, 1981)), the reflectance was simulated to convert to emissivity based on Kirchhoff's law. One major assumption in Hapke's theory is that the particles are large compared to the wavelength and closely packed. As a result, the particle cross

Table 9
List of typical soil TRD models, as in Table 7.

Name	Authors	Year	Main features	Category	Cited time
HAP1981	Hapke	1981	Only modeled reflected light; the particles are large compared to the wavelength and closely packed	physical model	1742
BEK1985	Becker et al.	1985	Improve the Leader's two-scale roughness model using a new shadowing function	physical model	35
HAP1993	Hapke	1993	Based on emission theory; It is a ray model that does not include diffraction effects.	physical model	1962
Mie/Hapke	Moersch and Christensen	1995	Using Mie theory to calculate single-scattering albedo for HAP1993	physical model	153
Mie/Conel	Moersch and Christensen	1995	Mie scattering theory for single scattering and a two-stream approximation for multiple scattering	physical model	153
VER1998	Verbrugghe and Cierniewski	1998	A parallel trihedron structure geometric model	physical model	5
Mie/DISORT	Pitman et al.	2005	Mie scattering theory for single scattering and 4-stream DISORT for multiple scattering	physical model	35
Mie/DW	Garcia-Santos et al.	2016	Mie scattering theory for single scattering and delta-Eddington approximation for single scattering albedo ω and asymmetry factor g	physical model	4
T-matrix/ Conel	Ito et al.	2017	T-matrix for single particle scattering and a two-stream approximation for multiple scattering	physical model	2
T-matrix/ Hapke	Ito et al.	2017	Using T-matrix to calculate single-scattering parameters for HAP1993	physical model	2
NER1991	Nerry et al.	1991	Only one variable: VZA	Empirical model	18
GAR2012	Garcia-Santos et al.	2012	Three variables: VZA, sand content, clay content	Empirical model	25

sections used in calculating the magnitude of absorption and scattering are geometrical optics cross sections and diffraction can be ignored. In 1993, Hapke developed the emission theory (HAP1993 (Hapke, 1993)), which can be used to simulate the directional emissivity with only two parameters, including single scattering albedo and view angle. It also does not include the diffraction effects. A two-stream approximation was used to get the scattering efficiency of a particle which can be converted to the single scattering albedo. The Mie/Hapke model (HAP1981; HAP1993) and Mie/Conel model were proposed by Moersch and Christensen (1995) to simulate the directional soil emissivity without removing the diffraction contribution. Wald and Salisbury (1995) proved the necessity to remove the diffraction for Mie/Hapke model (HAP1993), which finally led to the Mie-corrected/Hapke model. Pitman et al. (2005) proposed the Mie/DISORT model to simulate soil emissivity with a suggestion of 4-stream solution.

Mie/DW model was developed to simulate the directional emissivity of snow with a δ correction for diffraction removal. García-Santos et al. (2016) evaluated its accuracy for soil emissivity spectrum and compared it with Mie/Hapke model (HAP1993). The diffraction subtraction (Wald, 1994), static structure factor (Mishchenko and Macke, 1997) and δ correction method (Joseph et al., 1976) were used to perform the Mie scattering correction to take into account the closely packing conditions for these two models. They found that the Mie-corrected/Hapke performs relatively better but depends on the mean diameter of the grains for angular effect simulation. The results show that these models describe well the decrease of soil emissivity with viewing angle if the compactness correction of the soil grains formulated by the δ correction or diffraction subtraction methods is taken into account (García-Santos et al., 2018). The Mie-δ correction/Hapke model was also used to simulate the Regolith emissivity of Saturn's rings (Morishima et al., 2012). Ito et al. (2017) explored the ability of the T-matrix and radiative transfer models (Conel model and Hapke model) to produce emissivity spectra of enstatite particles of different sizes and obtained improved results compared to the combination of Mie theory and radiative transfer models. However, the diffraction parameter correction is still required in the T-matrix/Conel and T-matrix/Hapke models. The superposition of the T-matrix method with the ability to compute the scattering properties of an elementary volume (a cluster of particles) can produce relatively better agreement with the measurements than the sole use of the T-matrix method (Ito et al., 2018).

The roughness of the soil surface is another challenge in modeling. Lagouarde et al. (1995) found that the directional effects are highly dependent upon the structure of the observed surface, such as whether the soil is ploughed or not. Becker et al. (1985) extended the Leader's two-scale roughness model (Leader, 1976) using a new shadowing function to simulate the directional emissivity. The improvement accounts for the macrostructure (cavity effect) of the surface, which was shown to be responsible for a major part of the angular distribution, especially of the backscattering peak. For strong shadowing effect simulations, the Gaussian distribution (Cox and Munk, 1954) of soil surface slope was assumed. The modified model is then able to fit the measured data qualitatively and quantitatively in most situations. Verbrugghe and Cierniewski (1998) proposed a parallel trihedron structure geometric model to simulate the DBT of furrowed soil with the inputs of precise soil micro-relief geometry configuration, the illumination and viewing conditions of the surface and the radiative temperatures of the shaded and sunlit soil facets. They found that the TRD can reach up to 6 K while the VER1998 model can simulate the DBT with a coefficient of determination equal to 0.949.

Above all, many studies focused on directional soil emissivity simulation by considering the roughness, and the sand and clay percentage for dry inorganic bare soils. However, the influence of soil moisture (Lesaignoux et al., 2013; Wang et al., 2015) and soil organic matter contents was not analyzed comprehensively. In addition, the spectral soil model without considering the angular effect is still a challenge to the thermal infrared community. One limitation is that the measurements of the complex index of refraction of soil particles are rarely reported.

4.4. TRD modeling over vegetation

Compared to water, sea, snow and soil, more studies reported progress in TRD modeling over vegetated surfaces. The RTM, GOM, HM, 3D model and PM of vegetation canopies are discussed in this section. In the end, the roadmap of vegetation TRD model development is given in Section 4.4.6.

4.4.1. RT models

The grassland and mature cropland (e.g. soybean) are frequently abstracted as homogeneous scenes formed by many layers (see Fig. 4). The DBT of homogeneous scene is functioned with leaf area index (LAI), leaf angle distribution (LAD), leaf/soil emissivity, leaf/soil temperature profile and solar-target-sensor geometry. Each layer is described as a homogeneous medium with an infinitely thin thickness. The contribution of each layer is calculated by the directional gap fraction in Eq. (14) (Nilson, 1971). The definition of G in Eq. (14) can be found in the glossary. The DBT is calculated after an integration of the TIR contribution from all layers. The largest difficulty is to calculate the mutual-scattering between the different leaf layers, and the scattering between the leaf and background inclusive. In addition, the reflected

Fig. 4. Homogeneous scene examples: (a) grassland, (b) cropland, and (c) side view of the abstract scene.

atmospheric radiance should also be considered in the BOA DBT simulation.

$$pgap(\theta_v, \varphi_v) = e^{-G(\theta_v,\varphi_v)\cdot LAI/\cos\theta_v} \quad (14)$$

The pioneering RT model devoted to homogeneous vegetation canopies was developed by Kimes (1980). The directional gap fraction is the main solution of this model as shown in Eq. (15). For a vegetation canopy with n layers, the BOA thermal radiance, $I_{outgoing}$, depends on the mean component emissivity (ε_i) and temperature (T_i) of each layer i, and the component proportion which is determined by the canopy structure (LAI, LAD) and the viewing angle (θ_v, φ_v). σ in Eq. (15) is the Stefan-Boltzmann constant.

$$I_{outgoing}(\theta_v, \varphi_v) = \pi^{-1}\cdot \sum_{i=1}^{i=n}\left[\prod_{ii=0}^{ii=i-1} pgap_{ii}(\theta_v, \varphi_v)\cdot\left(1 - pgap_i(\theta_v\varphi_v)\right)\right]\cdot\varepsilon_i\cdot\sigma\cdot T_i^4 \quad (15)$$

This model (referred to as KIM1980) explains the main causes of TRD including two points: the architecture of the whole vegetation canopy and the temperature vertical profile. However, the scattering between layers and the reflected atmospheric radiance are omitted in this model. Prévot (1985) tried to overcome this shortcoming and proposed a new model (referred to as PRE1985). This model calculates canopy radiance as resulting from radiative interactions between the soil and the surrounding vegetation, plus interactions between the leaves within the vegetation. Iterations are performed to simulate the multiple reflections within the canopy and between the ground and the canopy. Fortunately, two iterations are generally sufficient for the model to converge since the leaf and soil emissivities (ε_v and ε_s) are close to unity in the TIR domain. The iteration solution hinders its wide application. Therefore, Francois proposed two parameterized models (Francois, 2002; Francois et al., 1997) based on PRE1985 model. The cavity effect factor was first introduced in the FRA1997 model to describe the multi-scattering effect within the canopy. It is defined as the ratio of (1-ε_{limit}) and (1-ε_v) whereas ε_{limit} is the limiting value for canopy emissivity corresponding to very large LAI, which can be calibrated by PRE1985 model. A LUT of cavity effect factor for different VZA was built. This concept is widely accepted by the TIR modeling community because of its simplicity. For FRA2002 model, the main consideration is the multiple scattering at the interface of the soil and vegetation layers, not the factor of cavity effect that describes the scattering effect within leaf layers. FRA2002 model was further improved by (Shi, 2011) to simulate the thermal radiance over a cropland and bare soil patch mixed scene.

The SAIL model (Verhoef, 1984) was first proposed to simulate the BRF of vegetation canopies in the VNIR band. It is a four-steam (downward, upward, solar and sensor) radiative transfer model. Then, it was later extended to the TIR domain with the same modeling framework but considering the temperature differences between the sunlit and shaded leaves/soils (named 4SAIL model (Verhoef et al., 2007)). The emission terms of leaf and soil were added into the four differential equations of SAIL. This extension enables the simulation of the TRD while considering multiple scattering inside the vegetation canopy. Liu et al. (2003) achieved a similar work (named TSAIL model) but only considering two components (leaf and soil) without separating their sunlit and shaded status. Therefore, the TSAIL model cannot simulate the hot spot effect. Thanks to Kirchhoff's law, the SAIL-Thermique model also has the potential to simulate directional canopy emissivity (DCE) of homogeneous canopy accounting for multiple scattering since it can compute directional-hemispherical reflectance based on SAIL formalism (Jacob et al., 2017; Olioso, 1992; Olioso et al., 2018, 2014). Ren et al. (2015a) evaluated the FRA1997 model taking 4SAIL simulated emissivity as reference and found that the cavity effect factor in FRA1997 was obviously overestimated. Then, they recalibrated the LUT. Cao et al. (2018b) found that the cavity effect factor should not only be angle-dependent but also LAI-dependent. This means that the cavity effect should change with LAI and canopy architecture (i.e., LAI 3D distribution). They developed the CE-P model based on the concept of spectral invariants in PARAS model (Rautiainen and Stenberg, 2005; Stenberg et al., 2016) to simulate the DCE and also DBT (Guo et al., 2019) with the ability to separate different orders of scattering.

Aforementioned models require to have a knowledge of the component temperatures in order to use them as inputs. But such information is generally difficult to obtain accurately. Coupling with energy balance model is a potential solution to determine the component temperature distributions. In this domain, the Cupid model is the most widely used as a multi source SVAT model (Norman, 1993, 1988, 1979) with the ability to simulate a wide variety of physiological and environmental processes simultaneously occurring at the soil/canopy interface. In Cupid, profiles of thermal radiant flux density and leaf temperature distributions are obtained from the simultaneous solution of radiative, convective and conductive equations. 4SAIL can predict both albedo and DBT in a coherent manner based on comprehensive radiation transfer processes devoted to homogeneous canopies. van der Tol et al. (2009) coupled the 4SAIL model and convective and conductive models, which led to the SCOPE model. This model can simulate the dynamic patterns of DBT using meteorological driven data. It is widely used in the TRD modeling community (Duffour et al., 2015).

Table 10 summarizes eleven typical radiative transfer models. It gives their names, authors, years of publication, main features, basic models and their citation count at the moment of writing this article, as an indication of their usage in general. The first parameterized model FRA1997 and the first four component model 4SAIL are the most cited by the community. In addition, the Cupid and SCOPE model are also widely cited because they can be used for research studies in domains of the TRD, and also the latent/sensible heat flux.

4.4.2. GO models

Three types of scenes (see Fig. 5) are abstracted as geometric objects to simulate DBT using GO models. These include, respectively, a discrete forest scene, a row-box scene, a crop and road mixed scene. The discrete forest scene considers four components (Pinheiro et al., 2004), which encompass sunlit/shaded leaf and sunlit/shaded soil. For a row-box scenes, some models consider three components (soil, box top and

Table 10
List of typical canopy radiative transfer models, as in Table 7.

Name	Authors	Year	Main features	Basic model	Cited times
KIM1980	Kimes	1980	No inter-scattering	NIL1971	73
PRE1985	Prévot	1985	Consider inter-scattering by iteration solution	KIM1980	29
FRA1997	Francois et al.	1997	Introduced the cavity effect factor	PRE1985	121
FRA2002	Francois et al.	2002	Considering the multi-scattering at the boundary of soil and leaf	PRE1985	80
SAIL-Thermique	Olioso	1992	Considering the multiple scattering	SAIL	36
TSAIL	Liu et al.	2003	Only consider two components	SAIL	30
4SAIL	Verhoef et al.	2007	Considering four components to simulate hot spot effect	SAIL	131
Cupid	Norman	1979	Considering energy balance	Energy balance Equation	429
SCOPE	van der Tol et al	2009	Considering energy balance	4SAIL	166
REN2015	Ren et al	2015	Recalibration of cavity effect factor by 4SAIL	4SAIL and FRA1997	13
CE-P	Cao et al.	2018	Give a new equation of cavity effect by spectral invariants	PARAS	–

box side) (Sobrino and Caselles, 1990) whereas other authors treat such a scene as a combination of four components (Jackson et al., 1979). Within the crop and road mixed scenes, six components are considered (Cao et al., 2015) to distinguish a sunlit/shaded road from sunlit/shaded soil and sunlit/shaded vegetation. The emissivity of each component takes a unique value, independently of whether it is sunlit or shaded.

GO models treat vegetation as opaque objects without considering the radiative transfer process of light inside these objects. They can simulate and interpret the hot spot effect that is associated to the shading effects between the opaque objects. Given information on canopy structure as well as illumination and viewing geometries, these models can estimate the relative abundances (projected fractional cover) of each component of the simulated landscape. By assuming the components to be Lambertian emitters and reflectors, these models can estimate the DBT of the composite surface. This is formulated by Eq. (16–17) where A_k is the component fractional cover in different viewing directions of component k, which is difficult to assess, K is the total number of components, ε_k and T_k are the broadband emissivity and radiometric temperature of k^{th} component, respectively, and BT_k is the brightness temperature of component k.

$$B^{-1}(I_{outgoing}(\theta_v,\varphi_v)) = \left(\sum_{k=1}^{k=K} A_k \cdot BT_k^4\right)^{\frac{1}{4}} \tag{16}$$

$$T(\theta_v,\varphi_v) = \left(\frac{\sum_{k=1}^{k=K} A_k \cdot \varepsilon_k \cdot T_k^4}{\sum_{k=1}^{k=K} A_k \cdot \varepsilon_k}\right)^{\frac{1}{4}} \tag{17}$$

The pioneering work about GO modeling was reported by Sutherland and Bartholic (1977). These authors measured the row-planted grove using a TIR sensor and found that the geometric structure of the scene can lead to an increase of canopy emissivity which is referred to as the cavity effect. An infinite long box structure for the medium and the view factors were first proposed to explain the variability as the most basic concept. Jackson et al. (1979) improved the original model from the nadir direction to the cross-row plane considering four components: sunlit leaf, shaded leaf, sunlit soil and shaded soil. Further in time, the model suitable for all planes was developed by Kimes (1983). Caselles and Sobrino (1989) proposed view factors of ground to box side, box side to ground and box side to another box side to properly simulate the single scattering resulting from the row structure. The FOV effect of the thermal radiometer was also considered later (Sobrino et al., 1990).

In pixels of satellite thermal images, non-vegetation endmembers (such as buildings, water bodies, roads) are always mixed with vegetation. Cao et al. (2015) attempted to build a new DBT model (CCM) to consider the contributions of roads. The road zone consists of the road itself together with adjacent crop sides. The KIM1983 model was selected to simulate DBT of a road zone with four components: sunlit/shaded leaf and sunlit/shaded road. The KIM1983 model can be considered as a special case of CCM. Pinheiro et al. (2004, 2006) designed

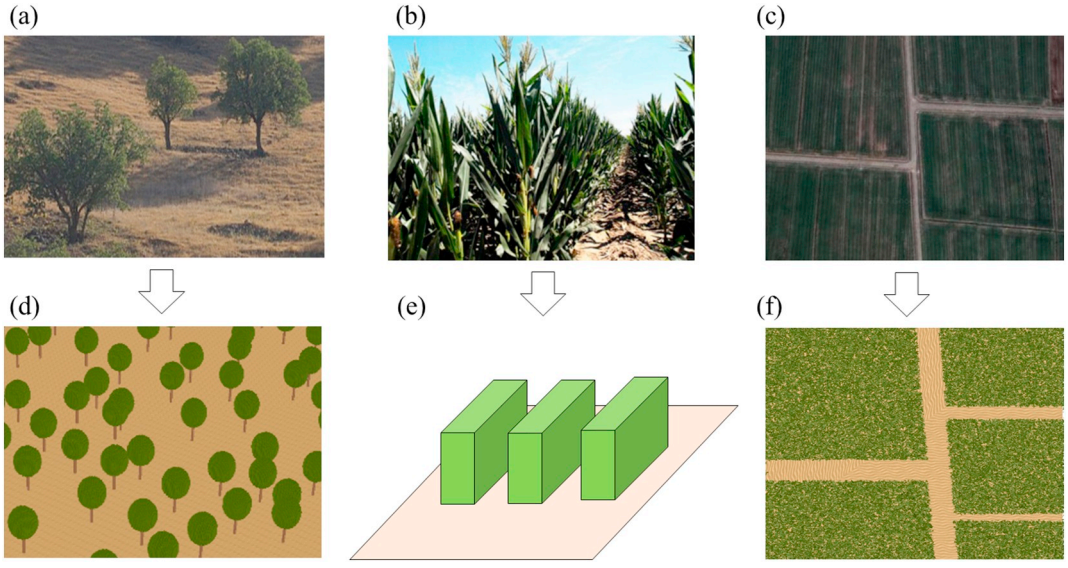

Fig. 5. Three typical scenes: (a) discrete forest, (b) row-planted cropland (c) crop and road mixed scene and their virtual scenes (d-f).

Table 11
List of typical GO models for discrete and row-planted canopies, as in Table 7.

Name	Authors	Year	Main features	Basic model	Cited time
SUT1977	Sutherland and Bartholic	1977	Abstract the row-planted scene to infinite long box	–	87
JAC1979	Jackson et al.	1979	Calculate the component fraction in the cross row plane	SUT1977	155
KIM1983	Kimes	1983	Calculate the component fraction in any plane	JAC1979	150
CAS1989	Caselles and Sobrino	1989	Propose three view factors to calculate single scattering	KIM1983	149
SOB1990	Sobrino and Caselles	1990	Considering the FOV effect	CAS1989	131
MGP	Pinheiro et al.	2004	First GO model for discrete forest canopy	Li-Strahler GO model	82
CCM	Cao et al.	2015	First GO model considering contribution of roads	KIM1983	10

the MGP model to simulate DBT of discrete tree canopies, such as savanna landscapes in Africa. Four components were considered in this model. It was extended from the geometric optics part of the Geometric Optical–Radiative Transfer (GORT) model in the VNIR band (Li and Strahler, 1992). This model has been used to analyze the angular effects of AVHRR (Pinheiro et al., 2004), MODIS (Yu et al., 2006) and SEVIRI (Rasmussen et al., 2011, 2010).

Table 11 lists seven typical GO models, including their names, authors, publication years, main features, basic models and their cited times. The row structure models were more widely concerned. The solution of calculating the component fractions in any plane achieved by Kimes (1983) was a landmark progress in the GO model series.

4.4.3. Hybrid models

The GO models of a row-planted scene in Section 4.4.2 assume that the row box is opaque. However, the existing gap within the rows will offer space leading to some light transmittance and also the inter-scattering increment as introduced in Section 4.4.1. Hybrid models were developed to improve the simulated accuracy of row-planted scenes through the combination of RT and GO modeling approaches. They consider the gap within row, the limit distance from soil layer to bottom leaf layer, the growth stage, the FOV effect etc (see Fig. 6).

The pioneering work was reported by Chen et al. (2002) who took into account the gaps along illumination and viewing directions. They proposed a bi-directional gap model on the basis of the idea of gap probability (Li and Strahler, 1988) of discrete vegetation canopy plus the inter-correlation of continuous vegetation developed by Kuusk (1985). This model can be used to explain the "hot spot" phenomenon in the TIR region. The improvement was achieved based on the KIM1983 model (Kimes, 1983). Yan et al. (2003) proposed a similar work to simulate the hot spot effect of row-planted vegetation with the idea of gap probability (Li and Strahler, 1988) for a discrete vegetation canopy. This includes notably the overlap index (Li and Strahler, 1986) of conifer forest canopy introduced by "Li-Strahler" to express the correlation between the sun and view directions. It should be noted that the Li-Strahler GO models were originally aimed to simulate the BRF in the VNIR band.

Yu et al. (2004) further improved the row model with gaps to be able to consider a limiting distance between the soil and leaf. This made the position of the hot spot phenomenon more accurate and widely accepted by the TRD modeling community. The Fovmod model (Ren et al., 2013) was developed to simulate the radiance with finite FOV based on the YU2004 model, the SOB1990 model (Sobrino et al., 1990) and the Extended DART model (Guillevic et al., 2003). Du et al. (2007) found that wheat ears will change the DBT pattern in the field experiment and proposed a new model considering the soil layer, leaf layer and ear layer (SLEC model). For SLEC, the leaf layer contribution is simulated based on the RT model KIM1980, and the ear contribution is simulated by the Li-Strahler GO model (Li and Strahler, 1986).

Table 12 summarizes the five typical hybrid models. The most cited one is YU2004 which considers the gap within the row and also the limiting distance between the soil and leaf layer. However, the number of cited times is obviously lower than that of landmark papers about the RT or GO models. Their complexity limits their practicability in fact. It can be seen that the KIM1983 model in Table 11 is cited by almost all of the hybrid models in Table 12 as it is used as the basis model.

4.4.4. 3D models

All the models in Sections 4.4.1–4.4.3 are physically-based models based on very simplified landscape. For instance, classic RTM considers that the vegetation canopy is a homogenous and continuous medium. Therefore, it is hardly extendable to discrete vegetation canopies. On the other hand, GOM model neglects the multiple-scattering mechanisms within canopy (Eq. (17)) or just uses a component brightness

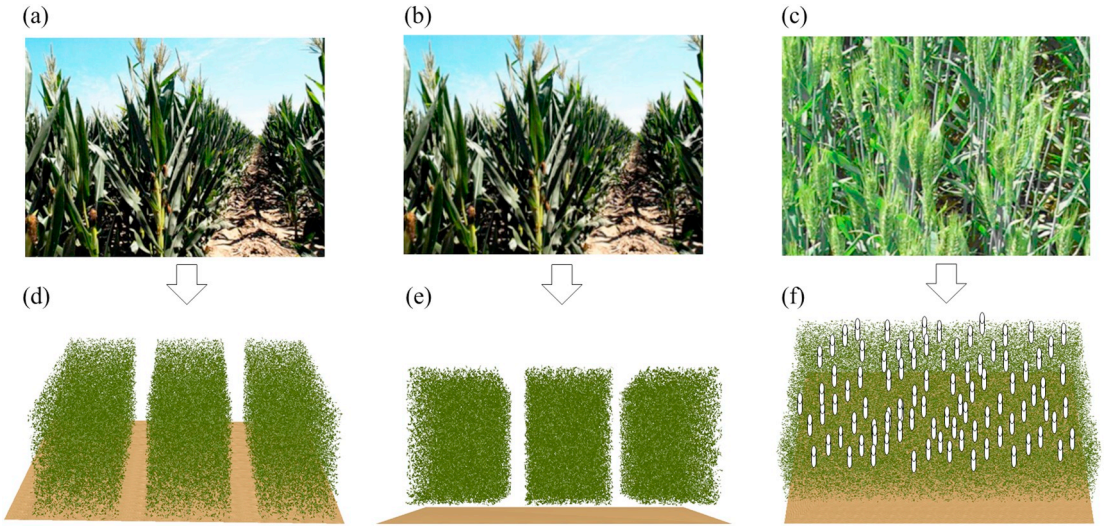

Fig. 6. Three typical row-planted scenes for hybrid TRD models: (a) no space between soil and leaf, (b) a limit distance from soil to leaf (c) wheat with ears and their virtual scenes (d-f).

Table 12
List of typical canopy hybrid models, as in Table 7.

Name	Authors	Year	Main features	Basic models	Cited times
CHE2002	Chen et al.	2002	Consider the gap within row	KIM1983, Li-Strahler, 1988 Kuusk, 1985	26
YAN2003	Yan et al.	2003	Consider the gap within row	KIM1983, Li-Strahler, 1988 Li-Strahler, 1986	28
YU2004	Yu et al.	2004	Consider a limit distance between soil and leaf	CHE2002 and GANIS, 1997	54
SLEC	Du et al.	2007	Consider the ear of wheat	KIM1980 and Li-Strahler, 1986	25
Fovmod	Ren et al.	2013	Consider the FOV effect	YU2004, SOB1990, DART, 2003	17

temperature concept (Eq. (16)) to circumvent the simulation of the multiple scattering effects. The hybrid model is a compromise scheme which combines the advantages of the RTM and the GOM. However, this is at the cost of strong simplifications considering the vegetation canopy 3D architecture. Instead, 3D models can make it possible to precisely describe the radiation regime and the DBT pattern over a virtual heterogeneous scene owing to a detailed simulation of vegetation morphology and growth characteristics.

In the TIR region, three categories of 3D models are widely used: Monte Carlo, Radiosity and Ray-tracing. Xu et al. (2002) proposed a matrix expression of the thermal radiative characteristics for an open complex medium in considering the scattering effect between components. The scattering increment was simulated by reverse Monte Carlo approach. The DART model (Gastellu-Etchegorry et al., 1996) was extended to the TIR domain by Guillevic et al. (2003). The radiation propagation of DART is tracked with a ray tracing approach combined with the discrete ordinate method. The Extended TIR DART model can also consider the contribution of atmospheric emission. It was further extended to DARTEB (Gastellu-Etchegorry, 2008) to simulate the energy budget over urban surfaces by a combination of the radiative transfer module and energy balance module. The RGM model (Qin and Gerstl, 2000) was even extended as TRGM (Liu et al., 2007) to simulate the DBT pattern. It was coupled with the Cupid model to simulate the dynamic component temperatures automatically (Huang et al., 2011) and further extended to be TRGMEB model (Bian et al., 2017b) with combination of the energy balance module as SCOPE. To determine the leaf level temperature distributions of a 3D canopy, the THERMO (Dauzat et al., 2001) and BAI2016 (Bailey et al., 2016) models were achieved by coupling with radiation budget and energy balance modules.

Table 13 lists the six typical 3D models. All of them were developed in the 2000's, which can be explained in terms of computational limitation in the past. Most of the 3D models are used to cross validate other models or to simulate images for future satellite missions because of their high accuracy.

4.4.5. Parametric models

As noted above, many physical models were designed to simulate the TRD pattern of vegetation canopies. However, the introduction of too many input parameters hindered their operational use. Indeed, for satellite remote sensing applications, there exists a real difficulty in obtaining all these input parameters in an accurate way. Therefore, parametric models were primarily invented to be a trade-off between physical accuracy and operational implementation. Recently, four kernel driven models have been proposed: ROSS-LI (Peng et al., 2011) and RL (Duffour et al., 2016b; Lagouarde and Irvine, 2008) are extensions of VNIR kernel models to TIR region, whereas LSF-LI (Su et al., 2002) and VIN2012 (Vinnikov et al., 2012) were specially designed for the TIR region. These models are summarized in Table 14. It can be seen that the VIN2012 is the most cited one. In addition, VIN2012 and RL were combined by Ermida et al. (2018b) to form a new parametric model with the ability to simulate the shadowing effect in daytime and the emissivity anisotropy in nighttime.

The kernel driven model was originally proposed by Roujean et al. (1992) to simulate the directional signatures of land surface reflectance. However, the TIR kernel driven models can be used to fit the hemispherical pattern of BOA thermal radiance, BOA DBT and also DRT. The LSF-LI, ROSS-LI and VIN2012 are linear combinations of three kernels as shown in Eq. (18–20), where K_{geo}, K_{vol} are the two kernels depending on the solar-target-view geometry, and f_{geo}, f_{vol}, f_{iso} are three kernel coefficients to be estimated. The isotropic kernel K_{iso} is omitted in the equations. For these three linear kernel models, the K_{geo} kernel is Li-DenseR (Li and Strahler, 1992), LiSparseR (Li and Strahler, 1986) and Solar (Vinnikov et al., 2012) kernels, the K_{vol} is LSF (Li et al., 1999), RossThick (Ross, 1981) and Emissivity (Vinnikov et al., 2012), respectively. Noting that these kernels are a simplification of physics with some necessary assumptions but still preserving the essence of their basic physical modeling ability. The combination of three kernels with different basic signatures allows describing almost all observed signatures thanks to an inversion procedure of kernel coefficients that provides the contribution for each of the basic signatures.

$$I_{outgoing}(\theta_v, \varphi_v, \theta_s, \varphi_s) = f_{geo} K_{geo}(\theta_v, \varphi_v, \theta_s, \varphi_s) + f_{vol} K_{vol}(\theta_v, \varphi_v, \theta_s, \varphi_s) + f_{iso} \quad (18)$$

$$B^{-1}[I_{outgoing}(\theta_v, \varphi_v, \theta_s, \varphi_s)] = f_{geo} K_{geo}(\theta_v, \varphi_v, \theta_s, \varphi_s) + f_{vol} K_{vol}(\theta_v, \varphi_v, \theta_s, \varphi_s) + f_{iso} \quad (19)$$

$$DRT(\theta_v, \varphi_v, \theta_s, \varphi_s) = f_{geo} K_{geo}(\theta_v, \varphi_v, \theta_s, \varphi_s) + f_{vol} K_{vol}(\theta_v, \varphi_v, \theta_s, \varphi_s) + f_{iso} \quad (20)$$

Roujean (2000) proposed a non-linear parametric model to simulate surface BRF in the VNIR with a focus on the simulation of the hot spot effect. Roujean and Lagouarde et al. extended this model to the TIR band by replacing the reflectance by the DBT (named as RL model (Duffour et al., 2016b; Lagouarde and Irvine, 2008)). The RL model is the only one with a non-linear expression, as shown in Eq. (21). There are also three parameters to be estimated: the nadir brightness

Table 13
List of typical 3D models, as in Table 7.

Name	Authors	Year	Basic model	Cited time
THERMO	Dauzat et al.	2001	Energy balance Equation	135
XU2002	Xu et al.	2002	Monte Carlo	18
Extended DART	Guillevic et al	2003	DART, 1996	47
TRGM	Liu et al.	2007	RGM, 2000	43
TRGMEB	Bian et al.	2017	TRGM, 2007	1
BAI2016	Bailey et al.	2016	Energy balance Equation	21

Table 14
List of typical semi-physical models, as in Table 7.

Name	Authors	Year	Basic model	Cited time
LSF-LI	Su et al.	2002	LSF, 1999 and Li-Strahler, 1992	7
ROSS-LI	Peng et al	2011	Ross, 1981 and Li-Strahler, 1986	8
VIN2012	Vinnikov et al.	2012	Mathematical statistical model	29
RL	Duffour et al.	2016	Hot spot BRF model	9
VIN2012-RL	Ermida et al.	2018	VIN2012 and RL models	1

temperature BT_N, the temperature difference (ΔT_{HS}) in the hot spot geometry compared to nadir observation, and a scale factor k to describe the width of the hot spot. The RL model also can be used to simulate the DRT by changing the left item to be $DRT(\theta_v,\varphi_v,\theta_s,\varphi_s)$ as in Eq. (20).

$$B^{-1}(I_{outgoing}(\theta_v,\varphi_v,\theta_s,\varphi_s)) = \Delta T_{HS}\frac{e^{-k\sqrt{\tan^2\theta_s+\tan^2\theta_v-2\tan\theta_s\tan\theta_v\cos\Delta\varphi}}-e^{-k\tan\theta_s}}{1-e^{-k\tan\theta_s}}+BT_N \quad (21)$$

Until now, they have been used to correct the angular effect of GOES EAST and GOES WEST LST products (Vinnikov et al., 2012) and MODIS and SEVIRI LST products (Ermida et al., 2018a, 2017). Liu et al. (2018) compared the ROSS-LI, VIN2012 and RL kernel models using 4SAIL as the reference and found that they underestimate the hot spot effect for continuous scenes. Ermida et al. (2018b) attempted to combine the VIN2012 model and RL model to overcome this problem. This problem should be improved before being applied to thermal infrared satellite acquisitions in order to achieve accurate angular effect corrections for LST products (Cao et al., 2019).

4.4.6. A roadmap of vegetation TRD model development

As reviewed in Sections 4.4.1–4.4.5, BRF models play an important role in the development of TRD models. Parts of them were even extended into the TIR band directly, such as the ROSS-LI and RL parametric models. Most of them have been improved by considering the self-emission of components while keeping the ability to deal with reflectance and transmittance for the BRF simulation. Fig. 7 shows the relationship between the typical RTM, GOM, HM, 3D and PM and corresponding BRF models (in blue font).

Fig. 7 illustrates the fact that the 4SAIL and KIM1983 models were two meaningful TRD models in the physical model development road. For 4SAIL, it successfully inherited the four stream radiation transfer solutions from SAIL model, so it can simulate multi-scattering in a homogeneous canopy precisely. The 4SAIL was often used as a benchmark to validate other analytical RTMs, such as the CE-P model, and it was also used to renew the LUT of the cavity effect factor, which has been the main parameterized solution for DBT simulation of a homogeneous canopy. In addition, it is coupled with an energy balance module to become a comprehensive SVAT model (SCOPE). For KIM1983, it firstly gave a solution of the component fraction in any plane of an infinitely long row box. It is the basic model of further development of GO models and also plays as the basis of hybrid models. In addition, the first GO model (CCM) that could simulate a mixed pixel with crop and road also referred to the KIM1983 model.

A striking feature to be observed from Fig. 7 is that most of the physical TRD models were developed before 2010 and that the development of parametric models is more recent. This is mostly due to the two following reasons: (1) the classical physical solutions of homogeneous and discrete scenes were judged mature enough to support the development of the parametric models; (2) the demand for an angular correction of LST products matches the criterion of operational efficiency. However, too many input parameters limited the operational use of physical models, meanwhile inverting parametric models

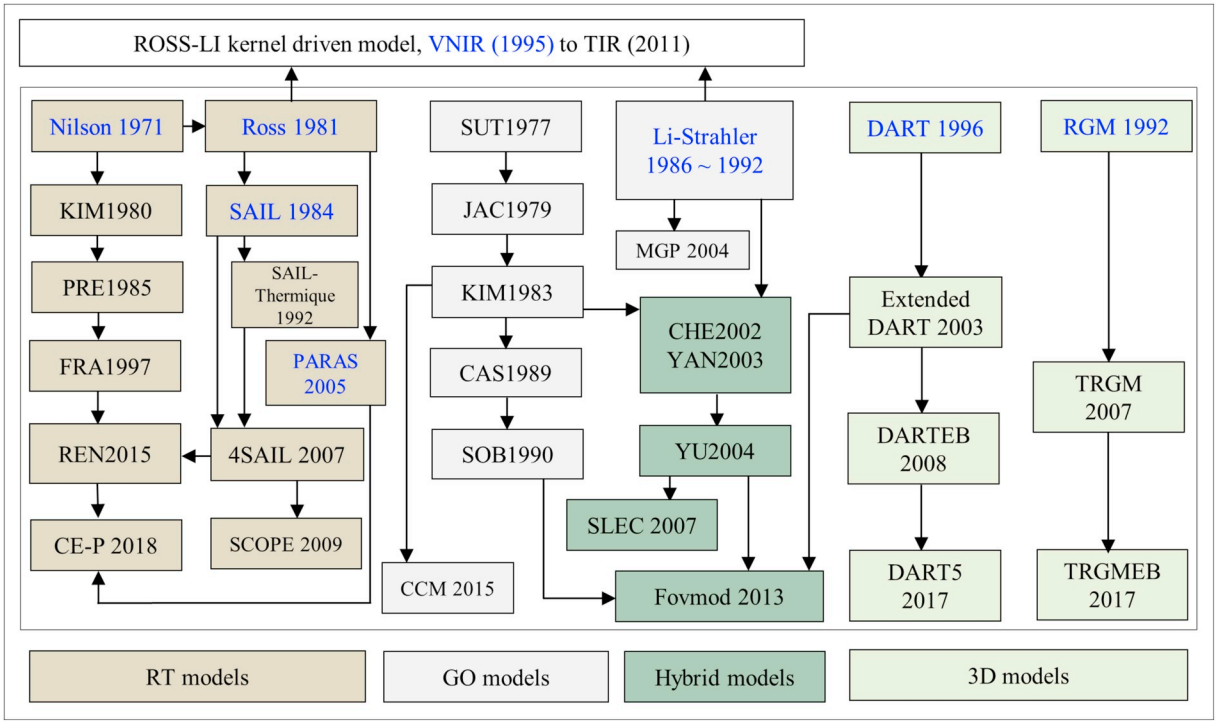

Fig. 7. The relationship between TRD models and BRF models.

Table 15
List of typical urban TRD models, as in Table 7.

Name	Authors	Year	Main features	Cited time
SUM	Soux et al.	2004	building-street-building-alley structure; no scattering	89
SUM_{VEG}	Dyce and Voogt	2018	Considering the tree crowns	7
LAG2010	Lagouarde et al.	2010	Linear combination of sunlit/shaded walls/streets/roofs	58
TITAN	Fontanilles et al	2008	Considering the singe scattering	22
Extended DART	Guillevic et al	2003	Considering the multi scattering	47
VIN2012	Vinnikov et al.	2012	Containing a emissivity kernel and a hot spot kernel	29
USEA	Sun et al.	2015	Aimed at simulation urban surface emissivity anisotropy based on VIN2012 model	4
RL	Duffour et al.	2016	Good performance for hot spot effect	10
GUTA-sparse	Wang et al.	2018	sparse urban canopy without mutual shadowing effect	–
GUTA-osg	Wang et al.	2018	dense urban canopy with mutual shadowing effect	–

behaved better numerically in virtue of their linear formulation.

4.5. TRD modeling over urban scenes

Urban surface temperature plays an important role in the investigation of urban climate and environment (Voogt and Oke, 2003). The TRD effect leads to variations of urban surface brightness temperature in different directions up to 10 K (Lagouarde et al., 2010; Voogt and Oke, 1998). The major challenges of urban TRD modeling is related to the complex 3D urban surface form, material temperature heterogeneity and emissivity properties that are similar to a vegetation canopy. Until now, four comprehensive experiments were carried out in different cities to study the urban energy budget, including the UBL-ESCOMPTE (Cros et al., 2004), BUBBLE (Rotach et al., 2005), CAPITOUL (Masson et al., 2008) and one in Vancouver (Voogt and Oke, 1998). There are two kinds of TRD models (3D and PM) over urban areas, as summarized in Table 15 and described below.

4.5.1. 3D models

A visualization model for interpolating 2D thermal satellite data over a 3D urban surface is developed by Nichol (1998) to study the difference between nadir temperature and complete temperature (Adderley et al., 2015; Voogt and Oke, 1997) over urban surfaces. The SUM model aimed at calculating the surface-sensor-sun relations was proposed by Soux et al. (2004). The urban canopy unit of SUM was abstracted as a building-street-building-alley combination in both the x- and y- directions, with the possibility of street and alley widths changing between the x- and y-directions. All surface elements within the sensor's FOV that are not blocked by other buildings contribute to the sensor-detected radiance weighted by their view fractions. The view fractions of 7 components (roofs, sunlit and shaded walls, and sunlit and shaded streets and alleys) are calculated by a contour integration based on Stokes theorem while all roofs are treated as flat in this model. The urban road network is usually not explicitly described, but is described as an equivalent medium, for example, a gridded distribution of roads with different widths and densities. The SUM model was extended (Voogt, 2008) to be suitable for actual building structure and validated by in-situ measurements in a light industrial district of Vancouver of British Columbia (Voogt and Oke, 1998). Ma (2009) proposed a similar computer model to simulate the thermal infrared radiation of 3-D urban targets (CoMSTIR) which was used to assess the thermal anisotropy on remote estimation of urban thermal inertia (Zhan et al., 2012). Dyce and Voogt (2018) investigated the influence of trees on urban TRD by considering the tree crown in the SUM model. They found the trees will both decrease and increase anisotropy as a function of tree crown plan fraction and building plan fraction.

To simulate the TRD over an urban canopy, Lagouarde et al. (2010) proposed a simple linear aggregation model with 6 components (sunlit/shaded walls/streets/roofs) weighted by their corresponding surface ratios in the viewed urban scene. The surface ratios are calculated by POV-Ray software based on the real 3D form of the city of Toulouse. The component directional brightness temperatures are simulated by the SOLENE urban energy budget model (Hénon et al., 2007) while the city is described by 18 canyon streets oriented in all directions in 10° steps. Results showed that TRD effect was underestimated by about 15–30%.

The scattering contributions of environment and atmosphere are simulated exactly in the TITAN model (Fontanilles et al., 2008). Here, the total incident signal is composed of solar reflection from the ground, atmosphere, ground emissions, and neighboring environmental effects. Therefore, the model can simulate the signal in the infrared spectral domain from 3 to 14 μm. The sensor level simulation is achieved through a coupling with the MODTRAN model. The street canyon structure is used in this model while the roofs of houses are slightly inclined to be more realistic. Each synthetic scene is modeled by triangular facets whose size is chosen by the user. This model was evaluated by the measurements in the CAPITOUL experiment (Masson et al., 2008) with radiative temperature anisotropy amplitude up to 10 K.

The DART model (Gastellu-Etchegorry et al., 2017) can simulate radiative transfer of heterogeneous areas, taking into account detailed 3D surface architecture. It has been widely used for vegetation and urban canopy simulations. It simulates the main mechanisms of interactions between surface and atmosphere from VNIR to TIR domain (Gastellu-Etchegorry et al., 2004) by a ray-tracing method. The outputs are reflectance, radiance, radiative temperatures, directional images at any latitude in the atmosphere, and also the urban 3D radiative budget. Kanda et al. built an outdoor micro-scale model (named COSMO) of an urban canopy with 32×16 blocks within $100 \times 50\,m^2$ in Japan (Kanda et al., 2007). Morrison et al. (2018) proposed a method to extract the component brightness temperature from near surface TIR camera observations over COSMO and simulate the directional anisotropy by DART. They found that the maximum difference between off-nadir and nadir directions can be up to 6.18 K at 13:00. Recently, DART was coupled with energy models for mapping the anthropogenic fluxes of Basel, London and Heraklion (Chrysoulakis et al., 2018). For that, DART combined with urban geometric database and BOA irradiance to obtain urban radiative budget fluxes from time series of Landsat-8 images at 100 m spatial resolution.

The distribution of the component temperature for an urban canopy is a stringent requirement by users eager to use this information as inputs for most analytical models (such as TITAN and DART). However, these TIR properties may vary rapidly in time, according to the local meteorology. It is an outcome of the urban surface energy budget. Asano et al. (1996) developed a spherical thermography technique to better sample the 3D temperature distribution of urban areas. Many microscale and mesoscale three-dimensional urban energy balance models have been developed with the aim of determining the temperature distribution and also the component fluxes (net radiation flux, sensible heat flux, latent heat flux, storage heat flux and so on). The most widely used urban energy budget models in TRD related research include the TUF-3D model (Krayenhoff and Voogt, 2007), the SOLENE

model (Hénon et al., 2011, 2007), the DARTEB model(Gastellu-Etchegorry, 2008) and the TEB model (Masson, 2000). The TUF-3D model was also used to evaluate the urban emissivity model based on sky view factor (Yang et al., 2016, 2015). Within these models, the radiation module, the conduction module and the convection module are considered with different degrees of complexity. Most of them use the canyon street model with flat roof while some models use the regular cubic block model (Krayenhoff and Voogt, 2007). Grimmond et al. (Grimmond, 2010) performed a comparison of 33 widely used urban energy budget models using a dataset containing net all-wave radiation, sensible heat, and latent heat flux observations for an industrial area in Vancouver, British Columbia, Canada. They found that the models simulate well net all-wave radiation but poorly the latent heat flux.

4.5.2. Parametric models

Parametric models for urban canopies have been increasingly considered in recent years. At first, they aimed to simulate directly the TIR signal by kernel driven models developed for a vegetation landscape. For instance, the RL model was used to describe the urban TRD effect over an urban surface (Duffour et al., 2016b; Lagouarde and Irvine, 2008). Results show that the R^2 of RL model can be up to 0.80 for airborne multi angle dataset collected over the city of Toulouse (Lagouarde et al., 2010). The VIN2012 model (Vinnikov et al., 2012) was also used to fit the limited observations over urban canopy (Jiang et al., 2018) in order to study the estimation of complete temperature of urban surface (Adderley et al., 2015; Voogt and Oke, 1997) by different DRTs.

Wang et al. proposed two new parametric models. One for a sparse urban canopy without mutual shadowing (Wang et al., 2018b) and one for a dense urban canopy with mutual shadowing effect (Wang et al., 2018a) respectively. The GUTA-sparse model was validated with airborne multi angle dataset over the city of Marseille (Lagouarde et al., 2004). The RMSEs obtained for four flights were between 0.40 and 0.56 K while the anisotropy amplitudes at the four flight times all exceeded 8 K. The GUTA-osg model was evaluated based on the anisotropy of airborne measurements of temperature over the city of Toulouse (Lagouarde et al., 2010), which gives RMSEs < 0.8 K and $R^2 > 0.85$. To describe the urban surface emissivity anisotropy, Sun et al. (2015) developed a parametric model (USEA) with three kernels referenced to the VIN2012 kernel model.

In summary, two conclusions can be drawn. The first one is that the energy budget coupling model is widely discussed for urban canopies. The other tendency is that more and more parametric models were developed in recent years. Model accuracy versus practicality appears to decide how to retain the best model. Clearly, a better trade-off between these two factors should be achieved in the future.

5. Potential applications of TRD models

Applications of TRD models may be grouped into two clear tendencies. (1) The development of practical parametric models for implementation at the scale of satellite observations to improve the precision of LST/LSE and SULR products. For instance, a possible option is to perform an angular normalization for the LST product, including correcting the off-nadir value to be the nadir value (Ren et al., 2014) or the hemispherical-integrated value (Vinnikov et al., 2012). In addition, integrating the ground leaving radiance in the upper hemispherical space results in a high-quality SULR product by considering the TRD effect (Hu et al., 2016b, 2017). However, the existing parametric models are still deficient, particularly as they underestimate the hot spot effect (Liu et al., 2018). (2) An enhanced consideration of surface structural elements and environmental conditions. Some physical models were used to separate the LSCT based on ground and airborne measurements and satellite observations (Zhan et al., 2013). In this section, background, difficulties, solutions and effectiveness will be summarized for three potential applications of TRD models, including LST products angular normalization, SULR estimation and LSCT separation. No global products of LST, SULR and LSCT considering TRD effect have been generated until now since there are still many challenges to overcome.

5.1. LST products angular normalization

The TRD effects place a severe limitation for comparing LST retrievals from different pixels in the same image and also for comparing LST derived from different images acquired under different viewing configuration. Ultimately, differences among satellite products due to the viewing geometries pose a serious limitation to the combined use of those products (Ermida et al., 2017). The reported absolute difference (mean bias) between the MODIS LST and SEVIRI LST can reach 12 K (4.5 K) over sparse vegetation canopies if observation geometries are disregarded (Ermida et al., 2014; Guillevic et al., 2013; Trigo et al., 2008), which emphasizes the need to account for illumination and viewing configurations for LST product. The MODIS sensor, mounted onboard a sun-synchronous orbit platform, does not see the surfaces with a unique viewing direction, conversely to SEVIRI that is mounted on a geostationary platform. Ideally, both MODIS and SEVIRI LST products should be normalized to a reference viewing geometry. It should be pointed out that angular normalization of LST products will not account for all existing differences among the products (i.e., differences induced by spectral or temporal or spatial configurations), which need to be characterized by considering collocated values obtained with similar view and illumination directions. Therefore, in the LST comparison of MODIS and VIIRS (Liu et al., 2015), the SNOs Tool (Simultaneous Nadir Overpasses (SNOs) Tool, 2014) was proposed to restrain their temporal and viewing angle differences. The SNOs Tool selection can make sure that the difference between LST products is coming from sensor calibration or the estimation algorithm, not from the TRD effect.

DART, MGP and SVAT models were used to account for the TRD effect in LST product inter-comparison or validation (Ermida et al., 2014; Guillevic et al., 2013, 2012), with difficulties induced by model requirements of many input parameters. Fortunately, parametric TRD models can normalize the angular effect for existing LST products, including correction to the nadir direction and hemispherical direction. Ren et al. (2014) corrected the estimated DRT to the nadir direction for WiDAS airborne multi angle dataset by using the ROSS-LI model. They found that the temperature difference between the normalized nadir temperature and the minimum temperature of the observing directions was 0.5–2.0 K for most vegetated pixels and always several Kelvin for most non-vegetated pixels. The VIN2012 model was used to correct the LST product of MODIS and SEVIRI to the nadir direction by Ermida et al. (2017). Their daytime difference decreases from 3.5 K to 2.3 K after adjustment to the nadir direction. The RL model was also used to achieve the angular normalization coupled with VIN2012. Better performances were obtained by VIN2012-RL compared to RL model, especially for the nighttime data and low tree coverage (Ermida et al., 2018b). In addition, Vinnikov et al. identified the difference between estimated DRT and hemispherical measurement of pyrgeometer and proposed the VIN2012 model (Vinnikov et al., 2012) to obtain hemispherical temperature from two observations of GOES-EAST and GOES-WEST, to be compared with the in-situ temperature from a pyrgeometer. The corrected difference between the LST product and pyrgeometer measurement estimated values can be better than 0.5 K (Vinnikov et al., 2012).

The corrected nadir LST have a closer correspondence to the nadir radiometer measurement (Duan et al., 2019; Li et al., 2013a; Niclòs et al., 2011) in the experiments. The corrected hemispherical LST has a better correspondence to pyrgeometer measurements in the field. The corrected hemispherical LST has the physical meaning of upward hemispherical integrated LST value while the pyrgeometer obtains the

downward hemispherical integrated value (Allen et al., 2017). The pyrgeometer measurement is most widely used because this observation is available for almost all flux stations, such as SURFRAD stations in the USA (Duan et al., 2019; Li et al., 2014c; Liu et al., 2015; Wang and Liang, 2009; Yu et al., 2009), HiWATER and CERN stations in China (Li et al., 2014b).

As already mentioned, physical TRD models and parametric models can be used to perform angular normalization. However, detailed structural information and component temperature distribution are difficult to obtain, which restricts the implementation of physical models. On the other hand, the lack of quasi-synchronous multi-angle datasets at the satellite scale limits the implementation of parametric TRD models. In order to decrease this constraint, multi-observations at different times in the same location (Ermida et al., 2017) and multi-pixels of different location with the same land cover type (Liu et al., 2018) are combined to form an equation system of multi-angle observations that can be used to estimate the kernel coefficients. Until now, only the GOES and SEVIRI disks are normalized by parametric models. Further work is needed to make the algorithms more practical and the LST product more consistent.

5.2. SULR estimation considering the TRD effect

SULR is an essential component of Earth surface radiation balance. The meteorological, hydrological, and agricultural research communities require an accuracy of 5–10 W/m^2 for SULR retrieved from satellite data. However, the RMSE of existing products (e.g. CERES-FSW, ISCCP-FD and GEWEX-SRB) ranges from 19.92 to 33.6 W/m^2 (Cheng and Liang, 2016). The methods for estimating SULR can be divided into three main categories: 1) the physical temperature emissivity algorithm (Tang and Li, 2008; Wang et al., 2005) with inputs of broadband emissivity, radiometric temperatures and downward longwave radiation (DLR); 2) the hybrid method (Cheng and Liang, 2016; Jiao et al., 2015; Wang et al., 2009), with a relationship between clear-sky TOA radiance and SULR built using an artificial neural network model or a multivariate linear model based on an extensive simulated database. The separation between LST and LSE is avoided in order to improve the accuracy; 3) hemispherical integration methods with consideration of the Earth surface TRD effect (Hu et al., 2017, 2016b).

The importance of the TRD effect of SULR estimate over vegetation and urban canopies had been reported long before (Otterman et al., 1997; Sugawara and Takamura, 2006). Cheng and Liang (2014) provided error ranges of surface longwave net radiation incurred by ignoring TRD of non-vegetated surfaces (water, snow, sand, soil and minerals). These works led to the pioneering development of considering the TRD effect in SULR estimation by Hu et al. (2016b). In this work, the 4SAIL model was used to simulate the multi angle DBT and also SULR dataset coupling with the MODTRAN atmospheric radiation transfer model as a support. Based on the ROSS-LI model, a selection of five angles was suggested to do the fitting in the upper hemispherical space. Firstly, the FRA1997 model helped to simulate the LSE TRD of continuous canopies with prior information about component emissivity and LAI. DRT was estimated for each viewing direction by a single channel algorithm. Then, the SULR considering TRD can be obtained by hemispherical integration of SULR in each direction. Thanks to this improvement, the RMSE and MBE are decreased about 7.5 W/m^2 and 10.5 W/m^2 at most (Hu et al., 2016b), compared to the traditional SULR algorithm that does not consider the TRD effect.

In extending this approach to discrete and row-planted scenes, the FRA1997 model should be improved to be able to simulate the directional canopy emissivity of these scenes, such as Bian et al. (2018) did recently. However, up to this date, no similar LSE directionality model for non-vegetated surface exists. Hu et al. (2017)) attempted to develop a direct physical algorithm by skipping the step of DRT and directional emissivity separation. At first, the goal was to simulate the directional surface outgoing spectral radiation in all upward directions by ROSS-LI kernel driven model with inputs from multi-angle observations. Then the directional surface outgoing spectral radiation was converted to directional longwave radiation by a linear regression equation. The SULR is finally obtained by integrating the directional longwave radiation. The main idea is similar to the hybrid method of traditional SULR solutions in omitting the process of LST/LSE separation. This is simpler to achieve and also more accurate, with further improvement of RMSE (MBE) equal to about 0.6 (1.7) W/m^2 (Hu et al., 2017). The largest asset of this direct physical algorithm is the potential to be applied in multiple land surface types, although it has been evaluated only over vegetation canopies and houses. More work needs to be done to evaluate its accuracy over other land covers and also to construct input multi angle datasets based on existing TIR satellite sensors.

5.3. Generating global LSCT product

LSCT has a clearer physical meaning compared to the pixel-averaged temperature. Demand for LSCT product is increasing for many diverse applications, such as land surface heat flux estimation based on two source energy balance (TSEB) model (Norman et al., 1995). The LSCT can be estimated from multi-angle, multi-spectral, multi-pixel, multi-resolution and multi-temporal observations. The multi-angle solution is relatively more mature than others because the band dependent emissivity is very difficult to determine for multi-spectral methods (Song and Zhao, 2007), the multi-pixel and multi-resolution methods cannot achieve pixel to pixel estimation (Zhan et al., 2011) and the temporal model parameters of multi-temporal method are difficult to determine (Zhan et al., 2013; Zhao et al., 2014). Here, only the multi-angle LSCT estimation methods are summarized since they strongly rely on TRD modeling progress. Reports about retrieval of LSCT over urban areas are scarce since they have a more complex 3D architecture (including roofs, walls, roads, vegetations and so on) than a vegetated canopy (Fontanilles and Briottet, 2011). This section will focus on the multi-angle LSCT estimation methods of vegetation.

For the continuous vegetated canopies, assuming that the number of sensor viewing angles (m) is not less than the number of canopy layers (n), the brightness component profile can be obtained by a least squares approach based on the KIM1980 model (Kimes, 1981) as shown in Eq. (22). Liu et al. (2012) retrieved the brightness temperature of leaf and soil components using a semi-physical approach that links them to the VNIR reflectance.

$$P_{BT^4} = (A^T A)^{-1} A^T M_{BT}$$

$$P_{BT^4} = \begin{pmatrix} BT(x_1)^4 \\ BT(x_2)^4 \\ \vdots \\ BT(x_n)^4 \end{pmatrix}, \quad A = \begin{pmatrix} a_{11} & a_{12} & \cdots & a_{1n} \\ a_{21} & a_{22} & \cdots & a_{2n} \\ \vdots & \vdots & \vdots & \vdots \\ a_{m1} & a_{m2} & \cdots & a_{mn} \end{pmatrix}, \quad M_{BT} = \begin{pmatrix} BT(\theta_1, \varphi_1)^4 \\ BT(\theta_2, \varphi_2)^4 \\ \vdots \\ BT(\theta_m, \varphi_m)^4 \end{pmatrix} \tag{22}$$

where the matrix P_{BT^4} shows the brightness temperature profile of different height (x_1 and x_n represent the top and bottom layer of the canopy, respectively), the component proportion matrix A is determined by the canopy 3D structure and the viewing angle, and M_{BT} is the matrix of BOA DBT measured by the TIR sensor in multi directions. Here, n is the total layer number and m is the total observation number.

In order to further estimate the radiometric temperature of each component, Xu et al. (2002) derived an improved matrix equation (see Eq. (23)), with separation of the component temperatures and emissivities. The innovative solution was to propose a matrix formed by component effective emissivity, which is determined by the component emissivity and the canopy structure to consider multi scattering between the components. It provides a generic framework to address LSCT estimation for continuous, discrete and also row-planted scenes (Fan and Xu, 2005). Bian et al. (2016) separated the leaf, sunlit soil and shaded soil temperatures from airborne WiDAS data based on Eq. (23) and further discussed the importance of considering a clumping index

in the LSCT estimation over discrete and row-planted scenes (Bian et al., 2017a) within this generic framework.

$$P_T = (W^T W)^{-1} W^T L$$

$$P_T = \begin{pmatrix} B(T_1) \\ B(T_2) \\ \vdots \\ B(T_n) \end{pmatrix} \cdot W = \begin{pmatrix} \varepsilon_{e,1}(\theta_1,\varphi_1) & \varepsilon_{e,2}(\theta_1,\varphi_1) & \cdots & \varepsilon_{e,n}(\theta_1,\varphi_1) \\ \varepsilon_{e,1}(\theta_2,\varphi_2) & \varepsilon_{e,2}(\theta_2,\varphi_2) & \cdots & \varepsilon_{e,n}(\theta_2,\varphi_2) \\ \vdots & \vdots & \vdots & \vdots \\ \varepsilon_{e,1}(\theta_m,\varphi_m) & \varepsilon_{e,2}(\theta_m,\varphi_m) & \cdots & \varepsilon_{e,n}(\theta_m,\varphi_m) \end{pmatrix} \cdot L = \begin{pmatrix} L(\theta_1,\varphi_1) \\ L(\theta_2,\varphi_2) \\ \vdots \\ L(\theta_m,\varphi_m) \end{pmatrix} \quad (23)$$

where L represents the multi angle measured radiance vector without the atmospheric effect, P_T represents the blackbody thermal radiance vector with the component radiometric temperatures (T_n), and W represents the matrix of component effective r-emissivity (i.e. Eq. (6) in Table 1) which is determined by the component emissivity and the canopy structure. Jia et al. (2003) and Li et al. (2001) retrieved the radiometric temperatures of leaves and soil at the satellite pixel scale using two angular observations from ATSR. Only two component temperature values can be obtained from two viewing angles, such as the ATSR series. However, component temperatures distinguishing sunlit and shaded status (Timmermans et al., 2009), even temperature profile from canopy top to bottom, can be retrieved from observations with more viewing angles. Most LSCT estimation studies were done based on airborne observations (Bian et al., 2016; Fan et al., 2004; Liu et al., 2012) and ground-based multi-angle measurements (Chehbouni et al., 2001; Francois et al., 1997; Kimes, 1983; Menenti et al., 2001; Merlin and Chehbouni, 2004; Xu et al., 2001). Unmanned Aerial Vehicle (UAV) multi-angle observations potentially permit to estimate LSCT with better temporal and spatial resolutions, and supplement traditional ground-based and airborne observations. The LSCT can even be extracted directly from UAV images acquired from low flying altitude (Hoffmann et al., 2016).

However, hitherto, no global LSCT product has been published. For the satellite LSCT inversion, the fraction of vegetation cover (FVC) is widely used to express the contribution of different components while the scattering effect is simplified. The atmospheric effects make the LSCT estimation from both airborne and spaceborne sensors more difficult (Coll et al., 2019; Jacob et al., 2003). The ATSR series sensor can supply observations with two viewing angles and two TIR bands. The split window band configuration can ensure accuracy of atmospheric correction. The two viewing angles approach has the potential to separate the leaf and soil temperatures, at least in theory. The TRD models have made a lot of progress, also the atmospheric correction algorithms (Li et al., 2013d) and LSE estimation methods (Li et al., 2013e). For example, the recently developed CE-P radiative transfer model (Cao et al., 2018b) directly links the LAI and viewing angle to the directional brightness temperatures with the ability to separate the zero, first, and second order scattering analytically. It potentially improves the accuracy of LSCT estimates compared to the former FVC solution. Furthermore, the two SLSTR sensors onboard Sentinel-3A and Sentinel-3B can jointly cover the Earth surface within one day. The virtual satellite constellation of polar and geostationary sensors can contribute multiple observations for any location within one day. Developing an operational LSCT estimation algorithm and generating the associated global product would be valuable. A new integrated retrieval method that combining multi-angle, multi-spectral, multi-pixel, multi-resolution and multi-temporal methods by using observations from virtual satellite constellation is a promising solution.

6. Future development and perspectives

6.1. TRD modeling over complex Earth surface

As reviewed in Section 4, most of the existing TRD models show high performance for pure pixels on flat ground. The topographic effect and pixel mixture are not widely discussed although the rugged terrain covers approximately 24% of the Earth land surface (Wen et al., 2018) and about 65% of the 1 km scale pixels of the Earth land surface are mixed (Yu et al., 2018).

Topography may change the TRD pattern of mountain forest canopies significantly. Lipton and Ward (1997) simulated the surface temperatures using a mesoscale numerical weather prediction model with high-resolution digital elevation data (30 m) from the USGS Digital Elevation Map datasets. The TRD effect reached as much as 9 K while assuming a satellite sensor resolution of 14 km. Even larger biases were found with finer sensor resolutions. The brightness temperature difference was up to 6 K over mountain forest canopies and varied as a function of the time of day, as indicated by GOES 8, 9, 10 simultaneous observations (Minnis and Khaiyer, 2000). Yan et al. (2016) proposed a longwave topographic radiation model considering all possible radiation-affecting factors over rugged terrain, including terrain obstruction, shadows, sky shielding by surrounding terrain, radiation contributed by the nearby terrain and invisibility of some pixels in observing direction. They found that topographic effects can result in longwave net radiation differences as high as 100 W/m^2. Even on the flat ground, the TIR pixel always contains different end-members, such as water bodies, leafy and woody material, and man-made material (Cao et al., 2015). The linear spectral mixture model could not consider the mutual shadowing and scattering effect at the boundary. The spatial resolutions of TIR sensors are relatively coarser than those of VNIR sensors, with larger probability of mixed pixels. It is, therefore, expected that the enhancement of TRD modeling over complex terrain and mixed scenes in the near future will improve our understanding and application of remotely sensed LST fields over those surfaces. Such understanding may also support the comparison of LST estimates from sensors with different spatial resolution over the same region.

6.2. Two ways for developing dynamic TRD model

Multi-angle datasets can be organized by removing cloudy day data from several day observations in the VNIR band (Zeng et al., 2016). This approach is based on the assumption that the land surface reflectance properties remain unchanged within a time frame (Jiao et al., 2014). However, for the land surface TIR properties, this is certainly not true, especially for the LST. Compared to the VNIR region that shows more inertia in the signal variability, rapid TIR temporal variations represent a major difficulty to correctly include the directionality issue in the satellite-derived LST/LSE products. The full potential of the TIR satellite-based network is limited by the close coupling that exists between the angular dependence and time dependence. It is almost impossible to exploit the angular information without dealing with the temporal issue. Therefore, for the angular normalization of GOES-EAST and GOES-WEST network, the observation time difference is always limited within 15 min to restrain the error caused by time shift (Vinnikov et al., 2012). In addition, analyzing the LST temporal trend without considering the angular effect is also physically confusing. The diurnal temperature cycle (DTC) modeling works based on 4-time MODIS observations within one day were limited by the hypothesis of isotropy LST (Duan et al., 2014). Recently, the existing nine four-parameter DTC models were compared to in-situ thermal observations and LST values from the geostationary MSG and FY-2F sensors without considering the TRD effect (Hong et al., 2018). The GOT09-dT-τ model with day-to-day change of residual temperature equal to zero and atmospheric optical thickness equal to 0.01 shows the best performance of the nine models.

Developing a dynamic TRD model is a potential solution to separate the close coupling between the angular dependence and time dependence. It can further be split into two aspects. The first one is the coupling of a TRD model with energy budget models to simulate DBT in any direction and at any time, such as SCOPE, TRGMEB and DARTEB models (Bian et al., 2017b; Gastellu-Etchegorry, 2008; van der Tol et al., 2009). Such category of models requires the tuning of numerous parameters, which is mathematically and numerically challenging. Multi-angle observations of different viewing times have the potential to determine these with supporting of meteorological driving data. The second solution is assuming dynamic LST results from the dynamic LSCT (Quan et al., 2014). Then, the angular anisotropy of LST can be explained by the view fraction variation of components. The TRD and DTC effects have the potential to be successfully separated. Therefore, for vegetation canopies with two components (soil and leaf), only the eight parameters of LSCT DTC models are unknown. These can be easily estimated using available observations within a given time period, no matter the viewing time and angle differences, which makes the second way simpler and more practical. However, for other land surfaces, such as urban canopies, at least six components have to be considered (sunlit/shaded roof, road and wall), and the subsequent estimation of 24 unknown LSCT DTC parameters remains challenging. On the other hand, the error of data pre-processing (geolocation, calibration) will make the solution of dynamic TIR satellite network very difficult.

6.3. Developing TIR kernel driven models aiming at LST product harmonization

The parametric model supports the angular normalization and SULR estimation by considering the TRD effect as discussed in Sections 5.1 and 5.2, respectively. To deal with instantaneous multi-angle observations, a parametric model offers a more practical use than a physical model because it does not require inputs of scene structure and component temperature distributions. Only the solar and sensor geometries are needed for a retrieval of the kernel coefficients. There are five existing TIR kernel models for vegetated surfaces (see Section 4.4.5). The ROSS-LI and LSF-LI models were selected to correct for the angular effect of DBT/LST of airborne sensors (Peng et al., 2011; Ren et al., 2014; Su et al., 2002) while RL, VIN2012 and VIN2012-RL models were adopted to correct for satellite-derived LST products (Ermida et al., 2018a, 2017; Vinnikov et al., 2012). The two DBT kernel models for urban targets (in Section 4.5.2) were also evaluated by airborne measurements, showing RMSE < 0.56 K and 0.8 K respectively (Wang et al., 2018a, 2018b).

The ROSS-LI and RL models were extended to the thermal domain without considering the physical mechanisms in the TIR region, such as the zero transmittance of components. The VIN2012 model is a mathematically statistic model. The accuracy of existing parametric models should be evaluated comprehensively by ground and airborne multi-angle measurements and simulated results of a physical model before being used to correct the directional anisotropy of TIR satellite observations. It is reported that all of the existing kernel driven models will underestimate the hot spot effect for homogeneous canopies (Liu et al., 2018) which should be overcome in the future to achieve a relatively better accuracy for both continuous and discrete canopies (Cao et al., 2019). The accuracy of existing kernel models for heterogeneous land surfaces was not discussed until now. To overcome these disadvantages, a new kernel driven model suitable for a complex surface should be developed based on recent progress of TRD physical models. Maybe some structure relevant information can be extracted from the VNIR band as a priori knowledge to improve the TIR kernel driven model. Developing a new heterogeneous kernel is a potential way to achieve this goal. But more kernels mean more viewing angles in practice to justify their contribution. Therefore, in terms of accuracy and practicality, the question will still remain in many cases.

The development of efficient models that can describe satellite-derived TRD at different spatial scales may be used to move towards a true harmonization of LST products derived from different sensors. This is a relevant issue since a global coverage with high temporal sampling will necessarily require the use of several platforms and, ideally, well inter-calibrate sensors.

6.4. Designing simultaneous multi-angle multi-band satellite sensors

Current multi-angle observations of a satellite network are constrained by differences in viewing time because the LST has significant temporal variability. The coupling of angular change and temporal variation makes a high-quality multi-angle dataset very difficult to obtain and further limits TRD related applications at the satellite scale. Ideally, there should be a TIR satellite sensor with simultaneous multi-viewing angles and high revisit frequency. TIR measurements usually change rapidly at the landscape scale. This is in favor for having high-resolution pixels clearly. Thus, ideally a constellation of polar orbiting satellites would appear to be the best solution to meet these requirements, which is potentially able to achieve with the onboard ECOSTRESS, GF-5, foreseen TRISHNA (Lagouarde et al., 2018) and LSTM (Koetz et al., 2018) missions. A geostationary satellite constellation will allow to supply high quality multi-angle multi-band observations with moderate spatial solution.

In this regard, parametric models may represent suitable tools to devise optimal angular configuration (Hu et al., 2016b; Ren et al., 2015b). For the minimum angle configuration, Ren et al. (2015b) suggested a protocol with three values (0, +30, −50) based on the 4SAIL generated dataset and ROSS-LI parametric model with three kernel coefficients to be estimated. Hu et al. (2016b) further discussed the best angle configuration using the same dataset and parametric model. They found that a five angle (0, ± 30, ± 50) configuration is preferable compared to the three angle (0, +30 and − 50) or even seven angle (such as 0, ± 10, ± 30 and ± 50) configurations. Lessons learned remain nevertheless too limited to decide on a design, as the 4SAIL model is only suitable for depicting a homogenous scene. Besides, the ROSS-LI model is a direct extension of the VNIR model with limited accuracy in the representativeness of TRD simulation (Liu et al., 2018). Furthermore, the analysis of Hu et al. (2016b) does not consider the FOV effect of the linear array imaging mode, which is the mainstream solution for satellite sensors.

For the scope of developing the best configuration of spectral bands, Sobrino and Jiménez-Muñoz (2014) proved there exists a minimum number of TIR bands required to separate the LST and LSE without any prior knowledge about the land surface. It should be at least 8.9, 10.6 and 12.0 μm. Beyond the NDVI dependent bands, also the water vapor dependent bands, the fire detecting bands and the cloud identifying bands should be included to ensure a high-quality dataset. For the best band configuration, the forthcoming TRISHNA (8.6, 9.1, 10.3 and 11.5 μm (Lagouarde et al., 2018)) and HyspIRI (3.98, 7.35, 8.28, 8.63, 9.07, 10.53, 11.33 and 12.05 μm (Lee et al., 2015)) missions can be referenced. They are aimed at monitoring the climate change, water cycle, terrestrial and aquatic ecosystems, Earth surface composition and change, extreme events, natural disasters, and human health through high spatio-temporal TIR observations (50–60 m resolution and 3–5 days revisit). The spatial resolution is also critical because high resolution will benefit TRD research but will also lead to a certain delay in the time of revisit. Launching a simultaneous multi-angle multi-band TIR sensor will bring new insights in the exploitation of TIR observations and applications, thereby forming a booster for more comprehensive research works in the near future.

6.5. Establishing multi-angle datasets from ground and UAV observations

Multi-angle datasets over different underlying surfaces are important for evaluating TRD models. However, the amount of accurate datasets reported in the literature is limited. Most of them were

obtained from airborne observations supported by comprehensive outdoor experiments which face two main difficulties: 1) they are financially expensive and therefore challenging for the community; 2) The time acquired for TIR images collection impacts the quality of multi-angle datasets. Thus, most of the existing TIR multi-angle datasets consist of spatio-temporal averaged values.

In recent years, UAV platforms provide new solutions to study the land surface thermal environments. Such platforms have been widely-used to identify crop frost, to analyze crop water stress index of different vegetated species, etc. Even the thermal point cloud of 3D tree canopies has been captured using UAV based photogrammetry (Webster et al., 2018). However, no TRD study based on UAV observations has been published, although UAV based solutions have the advantages of being low cost and not time-consuming, when compared with traditional airborne multi-angle observations. More efforts should be conducted to generate multi-angle datasets over different underlying surfaces by using UAV platforms in the future.

As a more common approach, ground-based and tower crane-based observations can acquire TIR multi-angle datasets. However, the footprint area and the experimental location are limited, which makes this approach difficult to be performed over tree canopies, urban canopies and sea surfaces. In addition, ground measurements are also influenced by both the LST temporal drift and the FOV effect. The simultaneous acquisition of component temperatures is vital to TRD models. Taking a tree canopy as an example, it is difficult to measure the shaded crown temperature in practice. More multi-angle datasets of canopy radiance and related component temperatures would be valuable, especially long-time series observations. Multi-angle datasets from ground and UAV observations will benefit the evaluation of TRD models and the development of new simultaneous multi-angle multi-band satellite sensors.

7. Summary

Besides atmospheric correction and temperature/emissivity separation, the TRD effect is another challenging issue in the thermal infrared domain. Most of the operational satellite LST and LSE products assume that the land surface radiation is isotropic, which leads to large uncertainties in the validation and/or inter-comparison. Many physical models (see Section 4) have been proposed to link land surface structure, component emissivities, temperature distribution and sensor-target-sun geometry to the satellite-recorded directional radiance. However, they are difficult to be used for angular correction since the temperature distribution is always unknown. Only two-angle TIR sensors are available onboard spaceborne platforms, which makes the impossibility of estimating more component temperature distribution beyond soil and leaf temperatures. Multi-angle observations have the potential to determine more component temperatures. However, multi-angle datasets from TIR satellite-based virtual network is limited by geolocation and radiometric calibration uncertainties and the close coupling between angular dependence and time dependence. It is almost impossible to exploit the angular information without dealing with the temporal issue. This is the main difference between the BRDF in the VNIR spectral domain and the TRD in the TIR spectral domain. Therefore, the parametric TRD model is a potential solution for LST angular correction and SULR accurate estimation since the exact temperature distribution is not required.

More works need to be conducted to develop comprehensive physical TRD models for complex land surfaces, and then some simplifications need to be done to propose a better parametric model as a trade-off between physical accuracy and operational use. Multi-angle TIR satellite sensor after optimizing the angle and spectral configurations will surely benefit TRD models and applications in the future. Some near surface, airborne and especially UAV experiments should be carried out to evaluate the sensor parameters at the regional scale and thus establish multi-angle datasets as an important support to future researches on TRD. The global LST, LSCT, SULR satellite products considered the TRD effect are widely expected by the TIR community and also the follow-up application areas. We can draw the following three conclusions.

(1) The TRD effect is evidenced with laboratory, ground, airborne and satellite observations. It seriously limits further improvements of LST accuracy. A true harmonization of LST products is significantly required and more cooperation between the TRD modeling and LST estimation communities should be carried out to achieve this goal. The TRD modeling is the most potential solution, and it is time to leave out the hypothesis of isothermal surface in LST estimation.
(2) Among physical models, existing models of water bodies, ice, sea, snow and vegetation are relatively more mature than those of barren lands and urban scenes. In addition, parametric TRD models are not as mature as physical TRD models although they have greater potential to achieve LST harmonization. Complex surface modeling, dynamic modeling and parametric modeling are three important directions for TRD model developments.
(3) It has been proved that multi-angle TIR observations permit to normalize the LST angular effect, to separate the LSCT and estimate SULR more accurately. More time series of ground-based and airborne multi-angle datasets over different surfaces are valuable to improve the TRD models. Such datasets can also help in determining optimal configurations for the future multi-angle satellite sensor, which will provide a more robust solution of the TRD effect in the TIR domain.

Glossary

AMTIS	Airborne Multi-angular TIR/VNIR Imaging System	a_k	Area fraction of k component
ASTER	Advanced Spaceborne Thermal Emission and Reflection Radiometer	B	Planck function
ATSR	Along-Track Scanning Radiometer	B'	First derivative of Planck's function
AVHRR	Advanced Very High Resolution Radiometer	B^{-1}	Inverse Planck function
BT	Brightness Temperature	$G(\theta_v,\varphi_v)$	Mean projection of unit leaf area in direction (θ_v,φ_v)
BRF	Bi-directional Reflectance Factor	I	TOA radiance
BOA	Bottom Of Atmosphere	$I_{outgoing}$	Surface outgoing radiance of BOA
DBT	Directional Brightness Temperature	k	Component order
DRT	Directional Radiometric Temperature	K	Total component number
DLR	Downward Longwave Radiation	i	Layer order
DCE	Directional Canopy Emissivity	n	Total layer number
UAV	Unmanned Aerial Vehicle	m	Total observation number
ECV	Essential Climate Variable	$pgap$	Directional gap fraction
FOV	Field-Of-View	$R_{at}\downarrow$	Downward atmospheric radiance
GOM	Geometric Optical Model	$R_{at}\uparrow$	Upward atmospheric radiance
GOES	Geostationary Operational Environmental Satellite	T	Temperature
HM	Hybird Model	T_0	Pixel reference temperature
LST	Land Surface Temperature	T_i	Mean temperature of layer i
LSE	Land Surface Emissivity	T_k	Temperature k component
LSCT	Land Surface Component Temperature	θ_v	View Zenith Angle
LAI	Leaf Area Index	φ_v	View Azimuth Angle
LAD	Leaf Angle Distribution	θ_s	Solar Zenith Angle
LUT	Look-up-table	φ_s	Solar Azimuth Angle

MAOS	Multi-Angle Observation System	τ	Atmospheric transmittance
MODIS	Moderate Resolution Imaging Spectroradiometer	λ	Wavelength
NDVI	Normalized Difference Vegetation Index	λ_1	Start wavelength of sensor
PM	Parametric Models	λ_2	End wavelength of sensor
RTM	Radiative Transfer Model	σ	Stefan-Boltzmann constant
SEVIRI	Spinning Enhanced Visible and Infrared Imager	ε	Emissivity
SSE	Sea Surface Emissivity	ε_k	Emissivity of k component
SST	Sea Surface Temperature	ε_i	Mean emissivity of layer i
SAA	Solar Azimuth Angle	ε_r	r-emissivity
SZA	Solar Zenith Angle	ε_r'	effective r-emissivity
SULR	Surface Upward Longwave Radiation	ε_e	e-emissivity
SVAT	Soil–Vegetation–Atmosphere Transfer	ε_{app}	apparent emissivity
SLSTR	Sea and Land Surface Temperature Radiometer	$\varepsilon_{channel,r}$	channel r-emissivity
TIR	Thermal InfraRed	$\varepsilon_{channel,e}$	channel e-emissivity
TRD	Thermal Radiation Directionality	ε_{bb}	Broadband emissivity
TOA	Top Of Atmosphere	ε_{limit}	Canopy limit emissivity
VZA	View Zenith Angle	ε_v	Leaf emissivity
VAA	View Azimuth Angle	ε_s	Soil emissivity
VNIR	Visible and Near InfraRed	$\Delta\varepsilon_{x\to k}$	Scattering from component x to k
WiDAS	Wide-angle Infrared Dual-mode line/area Array Scanner	$\Delta R_{scattering}$	Mutual scattering of components

Acknowledgements

This work was supported in part by the National Key Research and Development Program of China under Grant 2018YFA0605503, and in part by the National Natural Science of Foundation of China under Grant 41871258, and in part by the Strategic Priority Research Program of Chinese Academy of Sciences under Grant XDA15012400, and in part by the National Natural Science of Foundation of China under Grant 41501366, Grant 41571329, Grant 41571357, Grant 41571359, and Grant 41671366, and in part by the Director Foundation of the Institute of Remote Sensing and Digital Earth of Chinese Academy of Sciences under Grant Y5SJ1300CX, and in part by the China Scholarship Council project 201704910069, and in part by the PIFI project of Chinese Academy of Sciences under Grant 2017VCA0034, 2017VCC0011 and 2019DC0020.

References

Adderley, C., Christen, A., Voogt, J.A., 2015. The effect of radiometer placement and view on inferred directional and hemispheric radiometric temperatures of an urban canopy. Atmos. Meas. Tech. 8, 2699–2714. https://doi.org/10.5194/amt-8-2699-2015.

Allen, M., Voogt, J., Christen, A., Allen, M.A., Voogt, J.A., Christen, A., 2017. Time-continuous hemispherical urban surface temperatures. Remote Sens. 10, 3. https://doi.org/10.3390/rs10010003.

Anderson, M.C., Norman, J.M., Kustas, W.P., Houborg, R., Starks, P.J., Agam, N., 2008. A thermal-based remote sensing technique for routine mapping of land-surface carbon, water and energy fluxes from field to regional scales. Remote Sens. Environ. 112, 4227–4241.

Asano, K., Hoyano, A., Matsunaga, T., 1996. Development of an urban thermal environment measurement system using a new spherical thermography technique, in: infrared technology and applications XXII. Presented at the Infrared Technology and Applications XXII, International Society for Optics and Photonics, pp. 620–632. doi:https://doi.org/10.1117/12.243504.

Bailey, B.N., Stoll, R., Pardyjak, E.R., Miller, N.E., 2016. A new three-dimensional energy balance model for complex plant canopy geometries: model development and improved validation strategies. Agric. For. Meteorol. 218–219, 146–160. https://doi.org/10.1016/j.agrformet.2015.11.021.

Balick, L.K., Hutchinson, B.A., 1986. Directional thermal infrared exitance distributions from a leafless deciduous forest. IEEE Trans. Geosci. Remote Sens. GE-24, 693–698. https://doi.org/10.1109/TGRS.1986.289616.

Barton, I.J., 1992. Satellite-Derived Sea surface temperatures-a comparison between operational, theoretical, and experimental algorithms. J. Appl. Meteorol. 31, 433–442. https://doi.org/10.1175/1520-0450(1992)031<0433:SDSSTA>2.0.CO;2.

Barton, I.J., Takashima, T., 1986. An AVHRR investigation of surface emissivity near Lake Eyre, Australia. Remote Sens. Environ. 20, 153–163. https://doi.org/10.1016/0034-4257(86)90020-9.

Becker, F., Ramanantsizehena, P., Stoll, M.P., 1985. Angular variation of the bidirectional reflectance of bare soils in the thermal infrared band. Appl. Opt. 24, 365–375.

Benali, A., Carvalho, A.C., Nunes, J.P., Carvalhais, N., Santos, A., 2012. Estimating air surface temperature in Portugal using MODIS LST data. Remote Sens. Environ. 124, 108–121. https://doi.org/10.1016/j.rse.2012.04.024.

Berk, A., Anderson, G.P., Acharya, P.K., Bernstein, L.S., Muratov, L., Lee, J., Fox, M., Adler-Golden, S.M., Chetwynd, J.H., Hoke, M.L., Lockwood, R.B., Gardner, J.A., Cooley, T.W., Borel, C.C., Lewis, P.E., 2005. MODTRAN 5: a reformulated atmospheric band model with auxiliary species and practical multiple scattering options: update, in: algorithms and Technologies for Multispectral, hyperspectral, and Ultraspectral imagery XI. Presented at the algorithms and technologies for multispectral, hyperspectral, and ultraspectral imagery XI, International Society for Optics and Photonics, pp. 662–668. doi:https://doi.org/10.1117/12.606026.

Bian, Z., Xiao, Q., Cao, B., Du, Y., Li, H., Wang, H., Liu, Q., Liu, Q., 2016. Retrieval of leaf, sunlit soil, and shaded soil component temperatures using airborne thermal infrared multiangle observations. IEEE Trans. Geosci. Remote Sens. 54, 4660–4671. https://doi.org/10.1109/TGRS.2016.2547961.

Bian, Z., Cao, B., Li, H., Du, Y., Song, L., Fan, W., Xiao, Q., Liu, Q., 2017a. A robust inversion algorithm for surface leaf and soil temperatures using the vegetation clumping index. Remote Sens. 9, 780. https://doi.org/10.3390/rs9080780.

Bian, Z., Du, Y., Li, H., Cao, B., Huang, H., Xiao, Q., Liu, Q., 2017b. Modeling the temporal variability of thermal emissions from row-planted scenes using a radiosity and energy budget method. IEEE Trans. Geosci. Remote Sens. 55, 6010–6026. https://doi.org/10.1109/TGRS.2017.2719098.

Bian, Z., Cao, B., Li, H., Du, Y., Lagouarde, J.-P., Xiao, Q., Liu, Q., 2018. An analytical four-component directional brightness temperature model for crop and forest canopies. Remote Sens. Environ. 209, 731–746. https://doi.org/10.1016/j.rse.2018.03.010.

Borel, C.C., 1998. Surface emissivity and temperature retrieval for a hyperspectral sensor, in: IGARSS '98. Sensing and Managing the Environment. 1998 IEEE International Geoscience and Remote Sensing. Symposium Proceedings. (Cat. No.98CH36174). Presented at the IGARSS '98. Sensing and Managing the Environment. 1998 IEEE International Geoscience and Remote Sensing. Symposium Proceedings. (Cat. No. 98CH36174), pp. 546–549 vol.1. doi:https://doi.org/10.1109/IGARSS.1998.702966

Bourlier, C., 2006. Unpolarized emissivity with shadow and multiple reflections from random rough surfaces with the geometric optics approximation: application to Gaussian sea surfaces in the infrared band. Appl. Opt., AO 45, 6241–6254. doi:https://doi.org/10.1364/AO.45.006241.

Branch, R., Chickadel, C.C., Jessup, A.T., 2016. Infrared emissivity of seawater and foam at large incidence angles in the 3–14μm wavelength range. Remote Sens. Environ. 184, 15–24. https://doi.org/10.1016/j.rse.2016.06.009.

Cao, B., Liu, Q., Du, Y., Li, H., Wang, H., Xiao, Q., 2015. Modeling directional brightness temperature over mixed scenes of continuous crop and road: a case study of the Heihe River Basin. IEEE Geosci. Remote Sens. Lett. 12, 234–238. https://doi.org/10.1109/LGRS.2014.2333874.

Cao, B., Bian, Z., Xiao, Q., Fang, J., Huang, H., Bai, J., Fan, W., Du, Y., Li, H., Liu, Q., 2018a. Evaluation the Spatial-Temporal Average Method in the Multi-Angle Information Extraction Based on near Surface Observation Sensors. (Presented at the IEEE International Symposium on Geoscience and Remote Sensing IGARSS).

Cao, B., Guo, M., Fan, W., Xu, X., Peng, J., Ren, H., Du, Y., Li, H., Bian, Z., Hu, T., Xiao, Q., Liu, Q., 2018b. A New Directional Canopy Emissivity Model Based on Spectral Invariants. IEEE Transactions on Geoscience and Remote Sensing 1–16. doi:https://doi.org/10.1109/TGRS.2018.2845678

Cao, B., Gastellu-Etchegorry, J.-P., Du, Y., Li, H., Bian, Z., Hu, T., Fan, W., Xiao, Q., Liu, Q., 2019. Evaluation of four kernel-driven models in the thermal infrared band. IEEE Trans. Geosci. Remote Sens. https://doi.org/10.1109/TGRS.2019.2899600.

Caselles, V., Sobrino, JoséA, 1989. Determination of frosts in orange groves from NOAA-9 AVHRR data. Remote Sens. Environ. 29, 135–146. https://doi.org/10.1016/0034-4257(89)90022-9.

Chehbouni, A., Nouvellon, Y., Kerr, Y.H., Moran, M.S., Watts, C., Prevot, L., Goodrich, D.C., Rambal, S., 2001. Directional effect on radiative surface temperature measurements over a semiarid grassland site. Remote Sens. Environ. 76, 360–372.

Chen, L., Liu, Q., Fan, W., Li, X.W., Xiao, Q., Yan, G., Tian, G., 2002. A bi-directional gap model for simulating the directional thermal radiance of row crops. Science in China (Series D) 45, 1086–1098. https://doi.org/10.3321/j.issn:1006-9267.2002.04.004.

Chen, L., Li, Z.-L., Liu, Q., Chen, S., Tang, Y., Zhong, B., 2004. Definition of component effective emissivity for heterogeneous and non-isothermal surfaces and its approximate calculation. Int. J. Remote Sens. 25, 231–244. https://doi.org/10.1080/0143116031000116426.

Cheng, J., Liang, S., 2014. Effects of thermal-infrared emissivity directionality on surface broadband emissivity and longwave net radiation estimation. IEEE Geosci. Remote Sens. Lett. 11, 499–503. https://doi.org/10.1109/LGRS.2013.2270293.

Cheng, J., Liang, S., 2016. Global estimates for high-spatial-resolution clear-sky land surface upwelling longwave radiation from MODIS data. IEEE Trans. Geosci. Remote Sens. 54, 4115–4129. https://doi.org/10.1109/TGRS.2016.2537650.

Cheng, J., Liang, S., Wang, J., Li, X., 2010a. A stepwise refining algorithm of temperature and emissivity separation for hyperspectral thermal infrared data. IEEE Trans. Geosci. Remote Sens. 48, 1588–1597. https://doi.org/10.1109/TGRS.2009.2029852.

Cheng, J., Liang, S., Weng, F.Z., Wang, J.D., Li, X.W., 2010b. Comparison of radiative transfer models for simulating snow surface thermal infrared emissivity. Selected Topics in Applied Earth Observations and Remote Sensing, IEEE Journal of 3, 323–336. https://doi.org/10.1109/jstars.2010.2050300.

Cheng, J., Liang, S., Yao, Y., Zhang, X., 2013. Estimating the optimal broadband emissivity spectral range for calculating surface longwave net radiation. IEEE Geosci. Remote Sens. Lett. 10, 401–405. https://doi.org/10.1109/LGRS.2012.2206367.

Cheng, J., Cheng, X., Liang, S., Niclòs, R., Nie, A., Liu, Q., Cheng, J., Cheng, X., Liang, S., Niclòs, R., Nie, A., Liu, Q., 2017. A lookup table-based method for estimating sea surface hemispherical broadband emissivity values (8–13.5 μm). Remote Sensing 9, 245. doi:https://doi.org/10.3390/rs9030245.

Chrysoulakis, N., Grimmond, S., Feigenwinter, C., Lindberg, F., Gastellu-Etchegorry, J.-P., Marconcini, M., Mitraka, Z., Stagakis, S., Crawford, B., Olofson, F., Landier, L., Morrison, W., Parlow, E., 2018. Urban energy exchanges monitoring from space. Sci. Rep. 8. https://doi.org/10.1038/s41598-018-29873-x.

Coll, C., Galve, J.M., Niclòs, R., Valor, E., Barberà, M.J., 2019. Angular variations of brightness surface temperatures derived from dual-view measurements of the advanced along-track scanning radiometer using a new single band atmospheric correction method. Remote Sens. Environ. 223, 274–290. https://doi.org/10.1016/j.rse.2019.01.021.

Cox, C., Munk, W., 1954. Measurement of the roughness of the sea surface from photographs of the suns glitter. J. Opt. Soc. Am. 44, 838–850.

Cresswell, M.P., Morse, A.P., Thomson, M.C., Connor, S.J., 1999. Estimating surface air temperatures, from Meteosat land surface temperatures, using an empirical solar zenith angle model. Int. J. Remote Sens. 20, 1125–1132. https://doi.org/10.1080/014311699212885.

Cros, B., Durand, P., Cachier, H., Drobinski, Ph., Fréjafon, E., Kottmeier, C., Perros, P.E., Peuch, V.-H., Ponche, J.-L., Robin, D., Saïd, F., Toupance, G., Wortham, H., 2004. The ESCOMPTE program: an overview. Atmos. Res. 69, 241–279. doi:https://doi.org/10.1016/j.atmosres.2003.05.001.

Cuenca, J., Sobrino, J.A., 2004. Experimental measurements for studying angular and spectral variation of thermal infrared emissivity. Appl. Opt. 43, 4598–4602.

Czajkowski, K.P., Goward, S.N., Stadler, S.J., Walz, A., 2000. Thermal remote sensing of near surface environmental variables: application over the Oklahoma Mesonet. Prof. Geogr. 52, 345–357. https://doi.org/10.1111/0033-0124.00230.

Dauzat, J., Rapidel, B., Berger, A., 2001. Simulation of leaf transpiration and sap flow in virtual plants: model description and application to a coffee plantation in Costa Rica. Agric. For. Meteorol. 109, 143–160. https://doi.org/10.1016/S0168-1923(01)00236-2.

Dozier, J., Warren, S.G., 1982. Effect of viewing angle on the infrared brightness temperature of snow. Water Resour. Res. 18, 1424–1434.

Du, Y., Liu, Q., Chen, L., Liu, Q., Yu, T., 2007. Modeling directional brightness temperature of the winter wheat canopy at the ear stage. Geoscience and Remote Sensing, IEEE Transactions on 45, 3721–3739. https://doi.org/10.1109/tgrs.2007.903401.

Duan, S.-B., Li, Z.-L., Tang, B.-H., Wu, H., Tang, R., 2014. Generation of a time-consistent land surface temperature product from MODIS data. Remote Sens. Environ. 140, 339–349. https://doi.org/10.1016/j.rse.2013.09.003.

Duan, S.-B., Li, Z.-L., Li, H., Göttsche, F.-M., Wu, H., Zhao, W., Leng, P., Zhang, X., Coll, C., 2019. Validation of collection 6 MODIS land surface temperature product using in situ measurements. Remote Sens. Environ. 225, 16–29. https://doi.org/10.1016/j.rse.2019.02.020.

Duffour, C., Olioso, A., Demarty, J., Van der Tol, C., Lagouarde, J.-P., 2015. An evaluation of SCOPE: a tool to simulate the directional anisotropy of satellite-measured surface temperatures. Remote Sens. Environ. 158, 362–375. https://doi.org/10.1016/j.rse.2014.10.019.

Duffour, C., Lagouarde, J.-P., Olioso, A., Demarty, J., Roujean, J.-L., 2016a. Driving factors of the directional variability of thermal infrared signal in temperate regions. Remote Sens. Environ. 177, 248–264. https://doi.org/10.1016/j.rse.2016.02.024.

Duffour, C., Lagouarde, J.-P., Roujean, J.-L., 2016b. A two parameter model to simulate thermal infrared directional effects for remote sensing applications. Remote Sens. Environ. 186, 250–261. https://doi.org/10.1016/j.rse.2016.08.012.

Dyce, D.R., Voogt, J.A., 2018. The influence of tree crowns on urban thermal effective anisotropy. In: Urban Climate, ICUC9: The 9th International Conference on Urban Climate 23, pp. 91–113. https://doi.org/10.1016/j.uclim.2017.02.006.

Embury, O., Merchant, C.J., Filipiak, M.J., 2012. A reprocessing for climate of sea surface temperature from the along-track scanning radiometers: basis in radiative transfer. Remote Sensing of Environment, Advanced Along Track Scanning Radiometer (AATSR) Special Issue 116, 32–46. doi:https://doi.org/10.1016/j.rse.2010.10.016.

Ermida, S.L., Trigo, I.F., DaCamara, C.C., Göttsche, F.M., Olesen, F.S., Hulley, G., 2014. Validation of remotely sensed surface temperature over an oak woodland landscape — the problem of viewing and illumination geometries. Remote Sens. Environ. 148, 16–27. https://doi.org/10.1016/j.rse.2014.03.016.

Ermida, S.L., DaCamara, C.C., Trigo, I.F., Pires, A.C., Ghent, D., Remedios, J., 2017. Modelling directional effects on remotely sensed land surface temperature. Remote Sens. Environ. 190, 56–69. https://doi.org/10.1016/j.rse.2016.12.008.

Ermida, S.L., Trigo, I., DaCamara, C., Pires, A., 2018a. A methodology to simulate LST directional effects based on parametric models and landscape properties. Remote Sens. 10, 1114. https://doi.org/10.3390/rs10071114.

Ermida, S.L., Trigo, I.F., DaCamara, C.C., Roujean, J.-L., 2018b. Assessing the potential of parametric models to correct directional effects on local to global remotely sensed LST. Remote Sens. Environ. 209, 410–422. https://doi.org/10.1016/j.rse.2018.02.066.

Fan, W., Xu, X., 2005. Integrative inversion of land surface component temperature. Science in China Ser. D Earth Sciences 48, 2011–2019.

Fan, W., Xu, X., Wang, F., Liu, Q., 2004. Retrieval of plant and soil temperature by AMTIS data. Journal of Remote Sensing 8, 295–299.

Fontanilles, G., Briottet, X., 2011. A nonlinear unmixing method in the infrared domain. Appl. Opt., AO 50, 3666–3677. doi:https://doi.org/10.1364/AO.50.003666.

Fontanilles, G., Briottet, X., Fabre, S., Tremas, T., 2008. Thermal infrared radiance simulation with aggregation modeling (TITAN): an infrared radiative transfer model for heterogeneous three-dimensional surface-application over urban areas. Appl. Opt. 47, 5799–5810.

Fontanilles, G., Briottet, X., Fabre, S., Lefebvre, S., Vandenhaute, P.-F., 2010. Aggregation process of optical properties and temperature over heterogeneous surfaces in infrared domain. Appl. Opt., AO 49, 4655–4669. doi:https://doi.org/10.1364/AO.49.004655.

Francois, C., 2002. The potential of directional radiometric temperatures for monitoring soil and leaf temperature and soil moisture status. Remote Sens. Environ. 80, 122–133.

François, C., Ottlé, C., 1994. Estimation of the angular variation of the sea surface emissivity with the ATSR/ERS-1 data. Remote Sens. Environ. 48, 302–308. https://doi.org/10.1016/0034-4257(94)90004-3.

Francois, C., Ottle, C., Prevot, L., 1997. Analytical parameterization of canopy directional emissivity and directional radiance in the thermal infrared. Application on the retrieval of soil and foliage temperatures using two directional measurements. International Journal of Remote Sensing 18, 2587–2621.

Fuchs, M., Kanemasu, E.T., Kerr, J.P., Tanner, C.B., 1967. Effect of viewing angle on canopy temperature measurements with infrared thermometers. Agronomy Journal 59, 494-.

Garcia-Santos, V., Valor, E., Caselles, V., Angeles Burgos, M., Coll, C., 2012. On the angular variation of thermal infrared emissivity of inorganic soils. Journal of Geophysical Research-Atmospheres 117.

García-Santos, V., Coll, C., Valor, E., Niclòs, R., Caselles, V., 2015. Analyzing the anisotropy of thermal infrared emissivity over arid regions using a new MODIS land surface temperature and emissivity product (MOD21). Remote Sens. Environ. 169, 212–221. https://doi.org/10.1016/j.rse.2015.07.031.

García-Santos, V., Valor, E., Caselles, V., Doña, C., 2016. Validation and comparison of two models based on the Mie theory to predict 8–14 μm emissivity spectra of mineral surfaces. Journal of Geophysical Research: Solid Earth 121, 1739–1757. https://doi.org/10.1002/2015JB012654.

García-Santos, V., Valor, E., Biagio, C.D., Caselles, V., 2018. Predictive power of the emissivity angular variation of soils in the thermal infrared (8–14μm) region by two Mie-based emissivity theoretical models. IEEE Geosci. Remote Sens. Lett. 15, 1115–1119. https://doi.org/10.1109/LGRS.2018.2826446.

Gastellu-Etchegorry, J.P., 2008. 3D modeling of satellite spectral images, radiation budget and energy budget of urban landscapes. Meteorog. Atmos. Phys. 102, 187. https://doi.org/10.1007/s00703-008-0344-1.

Gastellu-Etchegorry, J.P., Demarez, V., Pinel, V., Zagolski, F., 1996. Modeling radiative transfer in heterogeneous 3-D vegetation canopies. Remote Sens. Environ. 58, 131–156. https://doi.org/10.1016/0034-4257(95)00253-7.

Gastellu-Etchegorry, J.P., Martin, E., Gascon, F., 2004. DART: a 3D model for simulating satellite images and studying surface radiation budget. Int. J. Remote Sens. 25, 73–96. https://doi.org/10.1080/0143116031000115166.

Gastellu-Etchegorry, J.P., Lauret, N., Yin, T.G., Landier, L., Kallel, A., Malenovsky, Z., Al Bitar, A., Aval, J., Benhmida, S., Qi, J.B., Medjdoub, G., Guilleux, J., Chavanon, E., Cook, B., Morton, D., Chrysoulakis, N., Mitraka, Z., 2017. DART: recent advances in remote sensing data modeling with atmosphere, polarization, and chlorophyll fluorescence. IEEE Journal of Selected Topics in Applied Earth Observations and Remote Sensing 10, 2640–2649. https://doi.org/10.1109/jstars.2017.2685528.

Ghent, D.J., Corlett, G.K., Göttsche, F.-M., Remedios, J.J., 2017. Global Land Surface Temperature From the Along-Track Scanning Radiometers. J. Geophys. Res. Atmos. 122, 2017JD027161. doi:https://doi.org/10.1002/2017JD027161

Gillespie, A., Rokugawa, S., Matsunaga, T., Cothern, J.S., Hook, S., Kahle, A.B., 1998. A temperature and emissivity separation algorithm for Advanced Spaceborne Thermal Emission and Reflection Radiometer (ASTER) images. IEEE Trans. Geosci. Remote Sens. 36, 1113–1126. https://doi.org/10.1109/36.700995.

Gong, P., Wang, J., Yu, Le, Zhao, Yongchao, Zhao, Yuanyuan, Liang, L., Niu, Z., Huang, X., Fu, H., Liu, S., Li, C., Li, X., Fu, W., Liu, C., Xu, Y., Wang, X., Cheng, Q., Hu, L., Yao, W., Zhang, Han, Zhu, P., Zhao, Z., Zhang, Haiying, Zheng, Y., Ji, L., Zhang, Y., Chen, H., Yan, A., Guo, J., Yu, Liang, Wang, L., Liu, X., Shi, T., Zhu, M., Chen, Y., Yang, G., Tang, P., Xu, B., Giri, C., Clinton, N., Zhu, Z., Chen, Jin, Chen, Jun, 2013. Finer resolution observation and monitoring of global land cover: first mapping results with Landsat TM and ETM + data. Int. J. Remote Sens. 34, 2607–2654. https://doi.org/10.1080/01431161.2012.748992.

Grimmond, C.S.B., 2010. The International Urban Energy Balance Models Comparison Project: First Results from Phase 1. Journal of Applied Meteorology and Climatology 49.

Guillevic, P.C., Gastellu-Etchegorry, J.P., Demarty, J., 2003. Thermal infrared radiative transfer within three-dimensional vegetation covers. J. Geophys. Res.-Atmos. 108, 42–48.

Guillevic, P.C., Privette, J.L., Coudert, B., Palecki, M.A., Demarty, J., Ottlé, C., Augustine, J.A., 2012. Land surface temperature product validation using NOAA's surface climate observation networks—scaling methodology for the visible infrared imager radiometer suite (VIIRS). Remote Sens. Environ. 124, 282–298. https://doi.org/10.1016/j.rse.2012.05.004.

Guillevic, P.C., Bork-Unkelbach, A., Göttsche, F.M., Hulley, G., Gastellu-Etchegorry, J.P., Olesen, F.S., Privette, J.L., 2013. Directional viewing effects on satellite land surface temperature products over sparse vegetation canopies - a multisensor analysis. IEEE Geosci. Remote Sens. Lett. 10, 1464–1468. https://doi.org/10.1109/LGRS.2013.2260319.

Guo, M., Cao, B., Fan, W., Ren, H., Cui, Y., Du, Y., Liu, Q., 2019. Scattering effect contributions to the directional canopy emissivity and brightness temperature based on CE-P and CBT-P models. IEEE Geosci. Remote Sens. Lett. 16, 957–961. https://doi.org/10.1109/LGRS.2018.2886606.

Hapke, B., 1981. Bidirectional reflectance spectroscopy: 1. Theory. Journal of Geophysical Research: Solid Earth 86, 3039–3305.

Hapke, B., 1993. Theory of Reflectance and Emittance Spectroscopy. Cambridge Univ, Press, New York.

Henderson, B.G., Theiler, J., Villeneuve, P., 2003. The polarized emissivity of a wind-

roughened sea surface: a Monte Carlo model. Remote Sens. Environ. 88, 453–467. https://doi.org/10.1016/j.rse.2003.09.003.
Hénon, A., Mestayer, P.G., Groleau, D., 2007. Thermo-radiative modeling and energy balance of the urban canopy: relations between simulated and measurable temperatures. In: Presented at the in: Proceedings of the 7th Symposium on the Urban Environment. California, AMS, San Diego.
Hénon, A., Mestayer, P.G., Groleau, D., Voogt, J., 2011. High resolution thermo-radiative modeling of an urban fragment in Marseilles city center during the UBL-ESCOMPTE campaign. Build. Environ. 46, 1747–1764. https://doi.org/10.1016/j.buildenv.2011.02.001.
Hoffmann, H., Nieto, H., Jensen, R., Guzinski, R., Zarco-Tejada, P., Friborg, T., 2016. Estimating evaporation with thermal UAV data and two-source energy balance models. Hydrol. Earth Syst. Sci. 20, 697–713. https://doi.org/10.5194/hess-20-697-2016.
Hong, F., Zhan, W., Göttsche, F.-M., Liu, Z., Zhou, J., Huang, F., Lai, J., Li, M., 2018. Comprehensive assessment of four-parameter diurnal land surface temperature cycle models under clear-sky. ISPRS J. Photogramm. Remote Sens. 142, 190–204. https://doi.org/10.1016/j.isprsjprs.2018.06.008.
Hori, M., Aoki, T., Tanikawa, T., Motoyoshi, H., Hachikubo, A., Sugiura, K., Yasunari, T.J., Eide, H., Storvold, R., Nakajima, Y., Takahashi, F., 2006. In-situ measured spectral directional emissivity of snow and ice in the 8-14 mu m atmospheric window. Remote Sens. Environ. 100, 486–502.
Hori, M., Aoki, T., Tanikawa, T., Hachikubo, A., Sugiura, K., Kuchiki, K., Niwano, M., 2013. Modeling angular-dependent spectral emissivity of snow and ice in the thermal infrared atmospheric window. Appl. Opt., AO 52, 7243–7255. doi:https://doi.org/10.1364/AO.52.007243.
Hu, L., Monaghan, A., Voogt, J.A., Barlage, M., 2016a. A first satellite-based observational assessment of urban thermal anisotropy. Remote Sens. Environ. 181, 111–121. https://doi.org/10.1016/j.rse.2016.03.043.
Hu, T., Du, Y., Cao, B., Li, H., Bian, Z., Sun, D., Liu, Q., 2016b. Estimation of upward longwave radiation from vegetated surfaces considering thermal directionality. IEEE Trans. Geosci. Remote Sens. 54, 6644–6658. https://doi.org/10.1109/TGRS.2016.2587695.
Hu, T., Cao, B., Du, Y., Li, H., Wang, C., Bian, Z., Sun, D., Liu, Q., 2017. Estimation of surface upward longwave radiation using a direct physical algorithm. IEEE Trans. Geosci. Remote Sens. 55, 4412–4426. https://doi.org/10.1109/TGRS.2017.2692261.
Hu, T., Renzullo, L.J., Cao, B., van Dijk, A.I.J.M., Du, Y., Li, H., Cheng, J., Xu, Z., Zhou, J., Liu, Q., 2019. Directional variation in surface emissivity inferred from the MYD21 product and its influence on estimated surface upwelling longwave radiation. Remote Sens. Environ. 228, 45–60. https://doi.org/10.1016/j.rse.2019.04.012.
Huang, H., Liu, Q., Qin, W., Du, Y., Li, X., 2011. Temporal patterns of thermal emission directionality of crop canopies. J. Geophys. Res.-Atmos. 116.
Hulst, W.D., 1957. Light Scattering by Small Particles. Dover, New York, NY.
Islam, T., Srivastava, P.K., Petropoulos, G.P., 2016. Uncertainty quantification in the infrared surface emissivity model (ISEM). IEEE Journal of Selected Topics in Applied Earth Observations and Remote Sensing 9, 5888–5892. https://doi.org/10.1109/JSTARS.2016.2557303.
Ito, G., Arnold, J.A., Glotch, T.D., 2017. T-matrix and radiative transfer hybrid models for densely packed particulates at mid-infrared wavelengths: packed particulate light scattering. Journal of Geophysical Research: Planets 122, 822–838. https://doi.org/10.1002/2017JE005271.
Ito, G., Mishchenko, M.I., Glotch, T.D., 2018. Radiative-transfer modeling of spectra of planetary regoliths using cluster-based dense packing modifications. Journal of Geophysical Research: Planets 123, 1203–1220. https://doi.org/10.1029/2018JE005532.
Jackson, R.D., Reginato, R.J., Pinter, P.J., Idso, S.B., 1979. Plant canopy information extraction from composite scene reflectance of row crops. Appl. Opt. 18, 3775–3782.
Jacob, F., Gu, X.F., Hanocq, J.-F., Tallet, N., Baret, F., 2003. Atmospheric corrections of single broadband channel and multidirectional airborne thermal infrared data: application to the ReSeDA experiment. Int. J. Remote Sens. 24, 3269–3290. https://doi.org/10.1080/01431160210153958.
Jacob, F., Schmugge, T., Olioso, A., French, A., Courault, D., Ogawa, K., Petitcolin, F., Chehbouni, G., Pinheiro, A., Privette, J., 2008. Modeling and Inversion in Thermal Infrared Remote Sensing over Vegetated Land Surfaces, in: Advances in Land Remote Sensing. Springer, Dordrecht, pp. 245–291. https://doi.org/10.1007/978-1-4020-6450-0_10.
Jacob, F., Lesaignoux, A., Olioso, A., Weiss, M., Caillault, K., Jacquemoud, S., Nerry, F., French, A., Schmugge, T., Briottet, X., Lagouarde, J.-P., 2017. Reassessment of the temperature-emissivity separation from multispectral thermal infrared data: introducing the impact of vegetation canopy by simulating the cavity effect with the SAIL-Thermique model. Remote Sens. Environ. 198, 160–172. https://doi.org/10.1016/j.rse.2017.06.006.
Jia, L., Li, Z.L., Menenti, M., Su, Z., Verhoef, W., Wan, Z., 2003. A practical algorithm to infer soil and foliage component temperatures from bi-angular ATSR-2 data. Int. J. Remote Sens. 24, 4739–4760.
Jiang, L., Zhan, W., Voogt, J., Zhao, L., Gao, L., Huang, F., Cai, Z., Ju, W., 2018. Remote estimation of complete urban surface temperature using only directional radiometric temperatures. Build. Environ. 135, 224–236. https://doi.org/10.1016/j.buildenv.2018.03.005.
Jiao, Z., Hill, M.J., Schaaf, C.B., Zhang, H., Wang, Z., Li, X., 2014. An anisotropic flat index (AFX) to derive BRDF archetypes from MODIS. Remote Sens. Environ. 141, 168–187. https://doi.org/10.1016/j.rse.2013.10.017.
Jiao, Z., Yan, G., Zhao, J., Wang, T., Chen, L., 2015. Estimation of surface upward longwave radiation from MODIS and VIIRS clear-sky data in the Tibetan Plateau. Remote Sens. Environ. 162, 221–237. https://doi.org/10.1016/j.rse.2015.02.021.
Joseph, J.H., Wiscombe, W.J., Weinman, J.A., 1976. The Delta-Eddington approximation for radiative flux transfer. J. Atmos. Sci. 33, 2452–2459. https://doi.org/10.1175/1520-0469(1976)033<2452:TDEAFR>2.0.CO;2.
Kanda, M., Kanega, M., Kawai, T., Moriwaki, R., Sugawara, H., 2007. Roughness lengths for momentum and heat derived from outdoor urban scale models. J. Appl. Meteor. Climatol. 46, 1067–1079. https://doi.org/10.1175/JAM2500.1.
Keck, T., Preusker, R., Fischer, J., 2017. Retrieving snow and ice characteristics by remotely sensed emissivity using the multi-view brightness temperature within 8μm to 14μm. Remote Sens. Environ. 201, 181–195. https://doi.org/10.1016/j.rse.2017.09.006.
Kimes, D.S., 1980. Effects of vegetation canopy structure on remotely sensed canopy temperatures. Remote Sens. Environ. 10, 165–174.
Kimes, D.S., 1981. Remote-sensing of temperature profiles in vegetation Canopies using multiple view angles and inversion techniques. IEEE Trans. Geosci. Remote Sens. 19, 85–90.
Kimes, D.S., 1983. Remote-sensing of row crop structure and component temperatures using directional radiometric temperatures and inversion techniques. Remote Sens. Environ. 13, 33–55.
Kimes, D.S., Kirchner, J.A., 1983. Directional radiometric measurements of row-crop temperatures. Int. J. Remote Sens. 4, 299–311.
Kimes, D.S., Idso, S.B., Pinter, P.J., Reginato, R.J., Jackson, R.D., 1980. View angle effects in the radiometric measurement of plant canopy temperatures. Remote Sens. Environ. 10, 273–284.
Koetz, B., Bastiaanssen, W., Berger, M., Defourney, P., Bello, U.D., Drusch, M., Drinkwater, M., Duca, R., Fernandez, V., Ghent, D., Guzinski, R., Hoogeveen, J., Hook, S., Lagouarde, J., Lemoine, G., Manolis, I., Martimort, P., Masek, J., Massart, M., Notarnicola, C., Sobrino, J., Udelhoven, T., 2018. High Spatio- Temporal Resolution Land Surface Temperature Mission - a Copernicus Candidate Mission in Support of Agricultural Monitoring, in: IGARSS 2018–2018 IEEE International Geoscience and Remote Sensing Symposium. Presented at the IGARSS 2018–2018 IEEE International Geoscience and Remote Sensing Symposium, pp. 8160–8162. doi:https://doi.org/10.1109/IGARSS.2018.8517433
Krayenhoff, E.S., Voogt, J.A., 2007. A microscale three-dimensional urban energy balance model for studying surface temperatures. Boundary-Layer Meteorol 123, 433–461. https://doi.org/10.1007/s10546-006-9153-6.
Kustas, W., Anderson, M., 2009. Advances in thermal infrared remote sensing for land surface modeling. Agric. For. Meteorol. 149, 2071–2081.
Kuusk, A., 1985. The hot spot effect of a uniform vegetative cover. Sov. J. Remote. Sens. 3, 645–658.
Labed, J., Stoll, M.P., 1991. Angular variation of land surface spectral emissivity in the thermal infrared - laboratory investigations on bare soils. Int. J. Remote Sens. 12, 2299–2310.
Lagouarde, J.-P., Irvine, M., 2008. Directional anisotropy in thermal infrared measurements over Toulouse city centre during the CAPITOUL measurement campaigns: first results. Meteorog. Atmos. Phys. 102, 173–185.
Lagouarde, J.-P., Kerr, Y.H., Brunet, Y., 1995. An experimental-study of angular effects on surface-temperature for various plant Canopies and bare soils. Agric. For. Meteorol. 77, 167–190.
Lagouarde, J.-P., Ballans, H., Moreau, P., Guyon, D., Coraboeuf, D., 2000. Experimental study of brightness surface temperature angular variations of maritime pine (Pinus pinaster) stands. Remote Sens. Environ. 72, 17–34. https://doi.org/10.1016/S0034-4257(99)00085-1.
Lagouarde, J.-P., Moreau, P., Irvine, M., Bonnefond, J.-M., Voogt, J.A., Solliec, F., 2004. Airborne experimental measurements of the angular variations in surface temperature over urban areas: case study of Marseille (France). Remote Sens. Environ. 93, 443–462. https://doi.org/10.1016/j.rse.2003.12.011.
Lagouarde, J.-P., Henon, A., Kurz, B., Moreau, P., Irvine, M., Voogt, J., Mestayer, P., 2010. Modelling daytime thermal infrared directional anisotropy over Toulouse city centre. Remote Sens. Environ. 114, 87–105.
Lagouarde, J.-P., Hénon, A., Irvine, M., Voogt, J., Pigeon, G., Moreau, P., Masson, V., Mestayer, P., 2012. Experimental characterization and modelling of the nighttime directional anisotropy of thermal infrared measurements over an urban area: case study of Toulouse (France). Remote Sensing of Environment, Remote Sensing of Urban Environments 117, 19–33. https://doi.org/10.1016/j.rse.2011.06.022.
Lagouarde, J.-P., Bach, M., Sobrino, J.A., Boulet, G., Briottet, X., Cherchali, S., Coudert, B., Dadou, I., Dedieu, G., Gamet, P., Hagolle, O., Jacob, F., Nerry, F., Olioso, A., Ottlé, C., Roujean, J., Fargant, G., 2013. The MISTIGRI thermal infrared project: scientific objectives and mission specifications. Int. J. Remote Sens. 34, 3437–3466. https://doi.org/10.1080/01431161.2012.716921.
Lagouarde, J.-P., Dayau, S., Moreau, P., Guyon, D., 2014. Directional anisotropy of brightness surface temperature over vineyards: case study over the Medoc region (SW France). IEEE Geosci. Remote Sens. Lett. 11, 574–578. https://doi.org/10.1109/LGRS.2013.2282492.
Lagouarde, J.-P., Bhattacharya, B.K., Crébassol, P., Gamet, P., Babu, S.S., Boulet, G., Briottet, X., Buddhiraju, K.M., Cherchali, S., Dadou, I., Dedieu, G., Gouhier, M., Hagolle, O., Irvine, M., Jacob, F., Kumar, A., Kumar, K.K., Laignel, B., Mallick, K., Murthy, C.S., Olioso, A., Ottlé, C., Pandya, M.R., Raju, P.V., Roujean, J.-L., Sekhar, M., Shukla, M.V., Singh, S.K., Sobrino, J., Ramakrishnan, R., 2018. The Indian-French TRISHNA Mission: Earth Observation in the Thermal Infrared with High Spatio-temporal Resolution. Presented at the 2018 IEEE International Geoscience and Remote Sensing Symposium, IEEE, Spain, pp. 4082–4085.
Leader, J.C., 1976. An analysis of the spatial coherence of laser light scattered from a surface with two scales of roughness*. J. Opt. Soc. am., JOSA 66, 536–546. doi:https://doi.org/10.1364/JOSA.66.000536.
Lee, C.M., Cable, M.L., Hook, S.J., Green, R.O., Ustin, S.L., Mandl, D.J., Middleton, E.M., 2015. An introduction to the NASA hyperspectral InfraRed imager (HyspIRI) mission and preparatory activities. Remote Sensing of Environment. Special Issue on the

Hyperspectral Infrared Imager (HyspIRI) 167, 6–19. https://doi.org/10.1016/j.rse.2015.06.012.
Lesaignoux, A., Fabre, S., Briottet, X., 2013. Influence of soil moisture content on spectral reflectance of bare soils in the 0.4–14 μm domain. Int. J. Remote Sens. 34, 2268–2285. https://doi.org/10.1080/01431161.2012.743693.
Li, H., Pinel, N., Bourlier, C., 2011a. A monostatic illumination function with surface reflections from one-dimensional rough surfaces. Waves Random Complex Media 21, 105–134. https://doi.org/10.1080/17455030.2010.524263.
Li, H., Pinel, N., Bourlier, C., 2011b. Polarized infrared emissivity of one-dimensional Gaussian sea surfaces with surface reflections. Appl. Opt., AO 50, 4611–4621. doi:https://doi.org/10.1364/AO.50.004611.
Li, H., Pinel, N., Bourlier, C., 2012. Polarized infrared emissivity of 2D sea surfaces with one surface reflection. Remote Sens. Environ. 124, 299–309. https://doi.org/10.1016/j.rse.2012.05.021.
Li, H., Liu, Q., Du, Y., Jiang, J., Wang, H., 2013a. Evaluation of the NCEP and MODIS atmospheric products for single channel land surface temperature retrieval with ground measurements: a case study of HJ-1B IRS data. IEEE Journal of Selected Topics in Applied Earth Observations and Remote Sensing 6, 1399–1408. https://doi.org/10.1109/JSTARS.2013.2255118.
Li, H., Pinel, N., Bourlier, C., 2013b. Polarized infrared reflectivity of one-dimensional Gaussian sea surfaces with surface reflections. Appl. Opt., AO 52, 6100–6111. doi:https://doi.org/10.1364/AO.52.006100.
Li, H., Pinel, N., Bourlier, C., 2014a. Polarized infrared reflectivity of 2D sea surfaces with two surface reflections. Remote Sens. Environ. 147, 145–155. https://doi.org/10.1016/j.rse.2014.02.018.
Li, H., Sun, D., Yu, Y., Wang, Hongyan, Liu, Y., Liu, Q., Du, Y., Wang, Heshun, Cao, B., 2014b. Evaluation of the VIIRS and MODIS LST products in an arid area of Northwest China. Remote Sens. Environ. 142, 111–121.
Li, S., Yu, Y., Sun, D., Tarpley, D., Zhan, X., Chiu, L., 2014c. Evaluation of 10 year AQUA/MODIS land surface temperature with SURFRAD observations. Int. J. Remote Sens. 35, 830–856. https://doi.org/10.1080/01431161.2013.873149.
Li, X., Li, X.W., Li, Z.Y., Ma, M.G., Wang, J., Xiao, Q., Liu, Q., Che, T., Chen, E.X., Yan, G.J., Hu, Z.Y., Zhang, L.X., Chu, R.Z., Su, P.X., Liu, Q.H., Liu, S.M., Wang, J.D., Niu, Z., Chen, Y., Jin, R., Wang, W.Z., Ran, Y.H., Xin, X.Z., Ren, H.Z., 2009. Watershed allied telemetry experimental research. J. Geophys. Res.-Atmos. 114, 19. https://doi.org/10.1029/2008jd011590.
Li, X., Cheng, G., Liu, S., Xiao, Q., Ma, M., Jin, R., Che, T., Liu, Q., Wang, W., Qi, Y., Wen, J., Li, H., Zhu, G., Guo, J., Ran, Y., Wang, S., Zhu, Z., Zhou, J., Hu, X., Xu, Z., 2013c. Heihe watershed allied telemetry experimental research (HiWATER): scientific objectives and experimental design. Bull. Amer. Meteorol. Soc. 94, 1145–1160. https://doi.org/10.1175/BAMS-D-12-00154.1.
Li, X.W., Strahler, A.H., 1986. Geometric-optical bidirectional reflectance modeling of a Conifer Forest Canopy. IEEE Trans. Geosci. Remote Sens. 24, 906–919.
Li, X.W., Strahler, A.H., 1988. Modeling the gap probability of a discontinuous vegetation canopy. Geoscience and Remote Sensing, IEEE Transactions on 26, 161–170. https://doi.org/10.1109/36.3017.
Li, X.W., Strahler, A.H., 1992. Geometric-optical bidirectional reflectance modeling of the discrete crown vegetation canopy: effect of crown shape and mutual shadowing. Geoscience and Remote Sensing, IEEE Transactions on 30, 276–292. https://doi.org/10.1109/36.134078.
Li, X.W., Strahler, A.H., Friedl, M.A., 1999. A conceptual model for effective directional emissivity from nonisothermal surfaces. IEEE Trans. Geosci. Remote Sens. 37, 2508–2517.
Li, Z.L., Stoll, M.P., Zhang, R.H., Jia, L., Su, Z.B., 2001. On the separate retrieval of soil and vegetation temperatures from ATSR data. Sci. China. Ser. D Earth Sci. 44, 97–111.
Li, Z.L., Tang, B.H., Wu, H., Ren, H.Z., Yan, G.J., Wan, Z.M., Trigo, I.F., Sobrino, J.A., 2013d. Satellite-derived land surface temperature: current status and perspectives. Remote Sens. Environ. 131, 14–37.
Li, Z.L., Wu, H., Wang, N., Qiu, S., Sobrino, J.A., Wan, Z.M., Tang, B.H., Yan, G.J., 2013e. Land surface emissivity retrieval from satellite data. Int. J. Remote Sens. 34, 3084–3127. https://doi.org/10.1080/01431161.2012.716540.
Li, Z.-L., Zhang, R., Sun, X., Su, H., Tang, X., Zhu, Z., Sobrino, J.A., 2004. Experimental system for the study of the directional thermal emission of natural surfaces. Int. J. Remote Sens. 25, 195–204. https://doi.org/10.1080/0143116031000116453.
Lipton, A.E., Ward, J.M., 1997. Satellite-view biases in retrieved surface temperatures in mountain areas. Remote Sens. Environ. 60, 92–100. https://doi.org/10.1016/S0034-4257(96)00165-4.
Liu, Q., Huang, H., Qin, W., Fu, K., Li, X., 2007. An extended 3-D radiosity-graphics combined model for studying thermal-emission directionality of crop canopy. IEEE Trans. Geosci. Remote Sens. 45, 2900–2918.
Liu, Q., Yan, C., Xiao, Q., Yan, G., Fang, L., 2012. Separating vegetation and soil temperature using airborne multiangular remote sensing image data. Int. J. Appl. Earth Obs. Geoinf. 17, 66–75.
Liu, Qiang, Chen, L., Liu, Qinhuo, Xiao, Q., 2003. A radiation transfer model to predict canopy radiation in thermal infrared band. Journal of Remote Sensing 7, 161–167.
Liu, X., Tang, B.-H., Li, Z.-L., 2018. Evaluation of three parametric models for estimating directional thermal radiation from simulation, airborne, and satellite data. Remote Sens. 10, 420. https://doi.org/10.3390/rs10030420.
Liu, Y., Yu, Y., Yu, P., Göttsche, F.M., Trigo, I.F., 2015. Quality assessment of S-NPP VIIRS land surface temperature product. Remote Sens. 7, 12215–12241. https://doi.org/10.3390/rs70912215.
Ma, W., 2009. A computer model for simulating the directional thermal radiance of urban targets (M.S. degree dissertation). Beijing Normal University, Beijing, China.
Ma, X.L., Wan, Z., Moeller, C.C., Menzel, W.P., Gumley, L.E., 2002. Simultaneous retrieval of atmospheric profiles, land-surface temperature, and surface emissivity from moderate-resolution imaging spectroradiometer thermal infrared data: extension of a two-step physical algorithm. Appl. Opt., AO 41, 909–924. doi:https://doi.org/10.1364/AO.41.000909.
Malakar, N.K., Hulley, G.C., 2016. A water vapor scaling model for improved land surface temperature and emissivity separation of MODIS thermal infrared data. Remote Sens. Environ. 182, 252–264. https://doi.org/10.1016/j.rse.2016.04.023.
Masson, V., 2000. A physically-based scheme for the urban energy budget in atmospheric models. Bound.-Layer Meteorol. 94, 357–397. https://doi.org/10.1023/A:1002463829265.
Masson, V., Gomes, L., Pigeon, G., Liousse, C., Pont, V., Lagouarde, J.-P., Voogt, J., Salmond, J., Oke, T.R., Hidalgo, J., Legain, D., Garrouste, O., Lac, C., Connan, O., Briottet, X., Lachérade, S., Tulet, P., 2008. The Canopy and Aerosol Particles Interactions in TOulouse Urban Layer (CAPITOUL) experiment. Meteorog. Atmos. Phys. 102, 135. https://doi.org/10.1007/s00703-008-0289-4.
Masuda, K., 2006. Infrared sea surface emissivity including multiple reflection effect for isotropic Gaussian slope distribution model. Remote Sens. Environ. 103, 488–496. https://doi.org/10.1016/j.rse.2006.04.011.
Masuda, K., Takashima, T., Takayama, Y., 1988. Emissivity of pure and sea waters for the model sea surface in the infrared window regions. Remote Sens. Environ. 24, 313–329. https://doi.org/10.1016/0034-4257(88)90032-6.
McGuire, M.J., Balick, L.K., Smith, J.A., Hutchison, B.A., 1989. Modeling directional thermal radiance from a Forest canopy. Remote Sens. Environ. 27, 169–186.
Menenti, M., Jia, L., Li, Z.-L., Djepa, V., Wang, J., Stoll, M.P., Su, Z.B., Rast, M., 2001. Estimation of soil and vegetation temperatures with multiangular thermal infrared observations: IMGRASS, HEIFE, and SGP 1997 experiments. Journal of Geophysical Research: Atmospheres 106, 11997–12010. https://doi.org/10.1029/2000JD900671.
Merlin, O., Chehbouni, A., 2004. Different approaches in estimating heat flux using dual angle observations of radiative surface temperature. Int. J. Remote Sens. 25, 275–289. https://doi.org/10.1080/0143116031000116408.
Minnis, P., Khaiyer, M.M., 2000. Anisotropy of land surface skin temperature derived from satellite data. J. Appl. Meteorol. 39, 1117–1129. https://doi.org/10.1175/1520-0450(2000)039<1117:AOLSST>2.0.CO;2.
Mishchenko, M.I., Macke, A., 1997. Asymmetry parameters of the phase function for isolated and densely packed spherical particles with multiple internal inclusions in the geometric optics limit. J. Quant. Spectrosc. Radiat. Transf. 57, 767–794. https://doi.org/10.1016/S0022-4073(97)00012-5.
Moersch, J.E., Christensen, P.R., 1995. Thermal emission from particulate surfaces: a comparison of scattering models with measured spectra. Journal of Geophysical Research: Planets 100, 7465–7477.
Monteith, J., Szeicz, G., 1962. Radiative temperature in the heat balance of nature surfaces. Q. J. R. Meteorol. Soc. 88, 496–507.
Morishima, R., Edgington, S.G., Spilker, L., 2012. Regolith grain sizes of Saturn's rings inferred from Cassini–CIRS far-infrared spectra. Icarus 221, 888–899. https://doi.org/10.1016/j.icarus.2012.09.012.
Morrison, W., Kotthaus, S., Grimmond, C.S.B., Inagaki, A., Yin, T., Gastellu-Etchegorry, J.-P., Kanda, M., Merchant, C.J., 2018. A novel method to obtain three-dimensional urban surface temperature from ground-based thermography. Remote Sens. Environ. 215, 268–283. https://doi.org/10.1016/j.rse.2018.05.004.
Nerry, F., Stoll, M.P., Kologo, N., 1991. Scattering of a Co2-laser beam at 10.6 Mu-M by bare soils - experimental-study of the polarized bidirectional scattering coefficient - model and comparison with directional emissivity measurements. Appl. Opt. 30, 3984–3995.
Nichol, J.E., 1998. Visualisation of urban surface temperatures derived from satellite images. Int. J. Remote Sens. 19, 1639–1649. https://doi.org/10.1080/014311698215153.
Niclos, R., Valor, E., Caselles, V., Coll, C., Sanchez, J.M., 2005. In situ angular measurements of thermal infrared sea surface emissivity - validation of models. Remote Sens. Environ. 94, 83–93.
Niclòs, R., Caselles, V., Valor, E., Coll, C., 2007. Foam effect on the sea surface emissivity in the 8–14 μm region. Journal of Geophysical Research: Oceans 112. https://doi.org/10.1029/2007JC004521.
Niclòs, R., Galve, J.M., Valiente, J.A., Estrela, M.J., Coll, C., 2011. Accuracy assessment of land surface temperature retrievals from MSG2-SEVIRI data. Remote Sens. Environ. 115, 2126–2140. https://doi.org/10.1016/j.rse.2011.04.017.
Nielsen, D.C., Clawson, K.L., Blad, B.L., 1984. Effect of solar azimuth and infrared thermometer view direction on measured soybean canopy temperature. Agron. J. 76, 607–610.
Nilson, T., 1971. A theoretical analysis of the frequency of gaps in plant stands. Agric. Meteorol. 8, 25–38.
Norman, J.M., 1979. Modeling the Complete Crop Canopy, in: Modification of the Aerial Environment of Plants. Am. Soc. Agric. Eng, Michigan, pp. 249–277.
Norman, J.M., 1988. Synthesis of canopy processes. In: Plant Canopies: Their Growth. Form and Function. Cambridge University Press, New York, pp. 161–175.
Norman, J.M., 1993. Scaling processes between leaf and canopy levels, in: scaling physiological processes: leaf to globe. Academic press, pp. 41–76.
Norman, J.M., Becker, F., 1995. Terminology in thermal infrared remote sensing of natural surfaces. Remote Sens. Rev. 12, 159–173. https://doi.org/10.1080/02757259509532284.
Norman, J.M., Kustas, W.P., Humes, K.S., 1995. Source approach for estimating soil and vegetation energy fluxes in observations of directional radiometric surface temperature. Agricultural and Forest Meteorology, Thermal Remote Sensing of the Energy and Water Balance over Vegetation 77, 263–293. https://doi.org/10.1016/0168-1923(95)02265-Y.
Ogawa, K., Schmugge, T., Jacob, F., French, A., 2003. Estimation of land surface window (8–12 μm) emissivity from multi-spectral thermal infrared remote sensing — A case

study in a part of Sahara Desert. Geophysical Research Letters 30. doi:https://doi.org/10.1029/2002GL016354
Olioso, A., 1992. Simulation deséchanges d'énergie et de masse d'un couvert végétal dans le but de relier la transpiration et la photosynthèse aux mesures de réflectance et de température de surface (Doctoral thesis). (Montpellier II).
Olioso, A., Jacob, F., Lesaignoux, A., 2014. SAIL-Thermique: A Model for Land Surface Spectral Emissivity in the Thermal Infrared. Evaluation and Reassessment of the Temperature- Emissivity Separation (TES) Algorithm in Presence of Vegetation Canopies. Presented at the AGU Fall Meeting Abstracts, pp. 0461.
Olioso, A., Jacob, F., Weiss, M., 2018. First Evaluation of Land Surface Emissivity Spectra Simulated with the Sail-Thermique Model, in: IGARSS 2018–2018 IEEE International Geoscience and Remote Sensing Symposium. Presented at the IGARSS 2018–2018 IEEE International Geoscience and Remote Sensing Symposium, pp. 3951–3954. doi:https://doi.org/10.1109/IGARSS.2018.8519436
Otterman, J., Starr, D., Brakke, T., Davies, R., Jacobowitz, H., Mehta, A., Cheruy, F., Prabhakara, C., 1997. Modeling zenith-angle dependence of outgoing longwave radiation: implication for flux measurements. Remote Sens. Environ. 62, 90–100. https://doi.org/10.1016/S0034-4257(97)00084-9.
Paw U, K.T., 1992. Development of models for thermal infrared radiation above and within plant canopies. ISPRS J. Photogramm. Remote Sens. 47, 189–203. https://doi.org/10.1016/0924-2716(92)90032-5.
Paw, U.K.T., Ustin, S.L., Zhang, C.A., 1989. Anisotropy of thermal infrared exitance in sunflower canopies. Agric. For. Meteorol. 48, 45–58.
Peng, J.J., Liu, Q., Liu, Q.H., Li, J.H., Ma, H.Z., Fang, L., 2011. Kernel-driven model fitting of multi-angle thermal infrared brightness temperature and its application. Journal of Infrared and Millimeter Waves 30, 361–365.
Pinheiro, A.C., Privette, J.L., Mahoney, R., Tucker, C.J., 2004. Directional effects in a daily AVHRR land surface temperature from satellites. IEEE Trans. Geosci. Remote Sens. 42, 1941–1954.
Pinheiro, A.C.T., Privette, J.L., Guillevic, P., 2006. Modeling the observed angular anisotropy of land surface temperature in a savanna. IEEE Trans. Geosci. Remote Sens. 44, 1036–1047. https://doi.org/10.1109/TGRS.2005.863827.
Pitman, K.M., Wolff, M.J., Clayton, G.C., 2005. Application of modern radiative transfer tools to model laboratory quartz emissivity: MODERN RT MODELS OF QUARTZ EMISSIVITY. Journal of Geophysical Research: Planets 110, n/a-n/a. doi:https://doi.org/10.1029/2005JE002428
Prévot, L., 1985. Modélisation des échanges radiatifs au sein des couverts végétaux. University of Paris VI, Application a la télédétection. Validation sur un couvert de mais.
Prihodko, L., Goward, S.N., 1997. Estimation of air temperature from remotely sensed surface observations. Remote Sens. Environ. 60, 335–346. https://doi.org/10.1016/S0034-4257(96)00216-7.
Qin, W.H., Gerstl, S.A.W., 2000. 3-D scene modeling of semidesert vegetation cover and its radiation regime. Remote Sens. Environ. 74, 145–162.
Qin, Z., Karnieli, A., Berliner, P., 2001. A mono-window algorithm for retrieving land surface temperature from Landsat TM data and its application to the Israel-Egypt border region. Int. J. Remote Sens. 22, 3719–3746. https://doi.org/10.1080/01431160010006971.
Quan, J., Chen, Y., Zhan, W., Wang, J., Voogt, J., Li, J., 2014. A hybrid method combining neighborhood information from satellite data with modeled diurnal temperature cycles over consecutive days. Remote Sens. Environ. 155, 257–274. https://doi.org/10.1016/j.rse.2014.08.034.
Rasmussen, M.O., Pinheiro, A.C., Proud, S.R., Sandholt, I., 2010. Modeling angular dependences in land surface temperatures from the SEVIRI instrument onboard the geostationary Meteosat second generation satellites. IEEE Trans. Geosci. Remote Sens. 48, 3123–3133.
Rasmussen, M.O., Gottsche, F.M., Olesen, F.S., Sandholt, I., 2011. Directional effects on land surface temperature estimation from Meteosat second generation for savanna landscapes. IEEE Trans. Geosci. Remote Sens. 49, 4458–4468. https://doi.org/10.1109/TGRS.2011.2144604.
Rautiainen, M., Stenberg, P., 2005. Application of photon recollision probability in coniferous canopy reflectance simulations. Remote Sens. Environ. 96, 98–107. https://doi.org/10.1016/j.rse.2005.02.009.
Rees, W.G., James, S.P., 1992. Angular variation of the infrared emissivity of ice and water surfaces. Int. J. Remote Sens. 13, 2873–2886.
Ren, H., Yan, G., Chen, L., Li, Z., 2011. Angular effect of MODIS emissivity products and its application to the split-window algorithm. ISPRS J. Photogramm. Remote Sens. 66, 498–507. https://doi.org/10.1016/j.isprsjprs.2011.02.008.
Ren, H., Yan, G., Liu, R., Nerry, F., Li, Z.-L., Hu, R., 2013. Impact of sensor footprint on measurement of directional brightness temperature of row crop canopies. Remote Sens. Environ. 134, 135–151. https://doi.org/10.1016/j.rse.2013.02.025.
Ren, H., Liu, R., Yan, G., Mu, X., Li, Z.L., Nerry, F., Liu, Q., 2014. Angular normalization of land surface temperature and emissivity using multiangular middle and thermal infrared data. IEEE Trans. Geosci. Remote Sens. 52, 4913–4931. https://doi.org/10.1109/TGRS.2013.2285924.
Ren, H., Liu, R., Yan, G., Li, Z., Qin, Q., Liu, Q., Nerry, F., 2015a. Performance evaluation of four directional emissivity analytical models with thermal SAIL model and airborne images. Opt. Express, OE 23, A346–A360. https://doi.org/10.1364/OE.23.00A346.
Ren, H., Yan, G., Liu, R., Li, Z., Qin, Q., Nerry, F., Liu, Q., 2015b. Determination of optimum viewing angles for the angular normalization of land surface temperature over vegetated surface. Sensors 15, 7537–7570. https://doi.org/10.3390/s150407537.
Ross, J.K., 1981. The Radiation Regime and Architecture of Plant Stands. Netherlands.
Rotach, M.W., Vogt, R., Bernhofer, C., Batchvarova, E., Christen, A., Clappier, A., Feddersen, B., Gryning, S.-E., Martucci, G., Mayer, H., Mitev, V., Oke, T.R., Parlow, E., Richner, H., Roth, M., Roulet, Y.-A., Ruffieux, D., Salmond, J.A., Schatzmann, M., Voogt, J.A., 2005. BUBBLE – an urban boundary layer meteorology project. Theor. Appl. Climatol. 81, 231–261. https://doi.org/10.1007/s00704-004-0117-9.
Roujean, J.-L., 2000. A parametric hot spot model for optical remote sensing applications. Remote Sens. Environ. 71, 197–206. https://doi.org/10.1016/S0034-4257(99)00080-2.
Roujean, J.-L., Leroy, M., Deschamps, P.-Y., 1992. A bidirectional reflectance model of the Earth's surface for the correction of remote sensing data. Journal of Geophysical Research: Atmospheres (1984–2012) 97, 20455–20468. doi:https://doi.org/10.1029/92JD01411
Salisbury, J.W., D'Aria, D.M., Wald, A., 1994. Measurements of thermal infrared spectral reflectance of frost, snow, and ice. Journal of Geophysical Research: Solid Earth 99, 24235–24240. https://doi.org/10.1029/94JB00579.
Shi, Y., 2011. Thermal infrared inverse model for component temperatures of mixed pixels. Int. J. Remote Sens. 32, 2297–2309. https://doi.org/10.1080/01431161003698252.
Simultaneous Nadir Overpasses (SNOs) Tool, 2014. http://ncc.nesdis.noaa.gov/SNOPredictions.
Smith, B., 1967. Geometrical shadowing of a random rough surface. IEEE Trans. Antennas Propag. 15, 668–671. https://doi.org/10.1109/TAP.1967.1138991.
Smith, W.L., Knuteson, R.O., Revercomb, H.E., Feltz, W., Howell, H.B., Menzel, W.P., Nalli, N.R., Brown, O., Brown, J., Minnett, P., McKeown, W., 1996. Observations of the infrared radiative properties of the ocean–implications for the measurement of sea surface temperature via satellite remote sensing. Bull. Amer. Meteor. Soc. 77, 41–52. https://doi.org/10.1175/1520-0477(1996)077<0041:OOTIRP>2.0.CO;2.
Snyder, W.C., Wan, Z.M., 1998. BRDF models to predict spectral reflectance and emissivity in the thermal infrared. IEEE Trans. Geosci. Remote Sens. 36, 214–225. https://doi.org/10.1109/36.655331.
Snyder, W.C., Wan, Z.M., Zhang, Y.L., Feng, Y.Z., 1997. Thermal infrared (3-14 mu m) bidirectional reflectance measurements of sands and soils. Remote Sens. Environ. 60, 101–109.
Sobrino, J.A., Li, Z.-L., Stoll, M.P., Becker, F., 1996. Multi-channel and multi-angle algorithms for estimating sea and land surface temperature with ATSR data. Int. J. Remote Sens. 17, 2089–2114. https://doi.org/10.1080/01431169608948760.
Sobrino, J.A., Caselles, V., 1990. Thermal infrared radiance model for interpreting the directional radiometric temperature of a vegetative surface. Remote Sens. Environ. 33, 193–199.
Sobrino, J.A., Cuenca, J., 1999. Angular variation of thermal infrared emissivity for some natural surfaces from experimental measurements. Appl. Opt. 38, 3931–3936.
Sobrino, J.A., Jiménez-Muñoz, J.C., 2014. Minimum configuration of thermal infrared bands for land surface temperature and emissivity estimation in the context of potential future missions. Remote Sens. Environ. 148, 158–167. https://doi.org/10.1016/j.rse.2014.03.027.
Sobrino, J.A., Romaguera, M., 2004. Land surface temperature retrieval from MSG1-SEVIRI data. Remote Sens. Environ. 92, 247–254. https://doi.org/10.1016/j.rse.2004.06.009.
Sobrino, J.A., Caselles, V., Becker, F., 1990. Significance of the remotely sensed thermal infrared measurements obtained over a citrus orchard. ISPRS J. Photogramm. Remote Sens. 44, 343–354. https://doi.org/10.1016/0924-2716(90)90077-O.
Sobrino, J.A., Jiménez-Muñoz, J.C., Verhoef, W., 2005. Canopy directional emissivity: comparison between models. Remote Sens. Environ. 99, 304–314. https://doi.org/10.1016/j.rse.2005.09.005.
Song, X., Zhao, Y., 2007. Study on component temperatures inversion using satellite remotely sensed data. Int. J. Remote Sens. 28, 2567–2579.
Soux, A., Voogt, J.A., Oke, T.R., 2004. A model to calculate what a remote sensor `Sees' of an urban surface. Bound.-Layer Meteorol. 111, 109–132. https://doi.org/10.1023/B:BOUN.0000010995.62115.46.
Stenberg, P., Mottus, M., Rautiainen, M., 2016. Photon recollision probability in modelling the radiation regime of canopies - a review. Remote Sens. Environ. 183, 98–108. https://doi.org/10.1016/j.rse.2016.05.013.
Su, L.H., Li, X.W., Friedl, M., Strahler, A., Gu, X.F., 2002. A kernel-driven model of effective directional emissivity for non-isothermal surfaces. Progress in Natural Science-Materials International 12, 603–607.
Sugawara, H., Takamura, T., 2006. Longwave radiation flux from an urban canopy: evaluation via measurements of directional radiometric temperature. Remote Sens. Environ. 104, 226–237. https://doi.org/10.1016/j.rse.2006.01.024.
Sun, H., Chen, Y., Zhan, W., Wang, M., Ma, W., 2015. A kernel model for urban surface thermal emissivity anisotropy and its uncertainties. J. Infrared Millim. Waves 34, 66–73.
Sun, Y., Wang, J., Zhang, R., Gillies, R., Xue, Y., Bo, Y., 2005. Air temperature retrieval from remote sensing data based on thermodynamics. Theor. Appl. Climatol. 80, 37–48.
Sutherland, R.A., Bartholic, J.F., 1977. Significance of vegetation in interpreting thermal-radiation from a terrestrial surface. J. Appl. Meteorol. 16, 759–763.
Tang, B., Li, Z.-L., 2008. Estimation of instantaneous net surface longwave radiation from MODIS cloud-free data. Remote Sens. Environ. 112, 3482–3492. https://doi.org/10.1016/j.rse.2008.04.004.
Timmermans, J., Verhoef, W., van der Tol, C., Su, Z., 2009. Retrieval of canopy component temperatures through Bayesian inversion of directional thermal measurements. Hydrol. Earth Syst. Sci. 13, 1249–1260. https://doi.org/10.5194/hess-13-1249-2009.
van der Tol, C., Verhoef, W., Timmermans, J., Verhoef, A., Su, Z., 2009. An integrated model of soil-canopy spectral radiances, photosynthesis, fluorescence, temperature and energy balance. Biogeosciences 6, 3109–3129. https://doi.org/10.5194/bg-6-3109-2009.
Trigo, I.F., Menteiro, I.T., Olesen, F.S., Kabsch, E., 2008. An assessment of remotely sensed land surface temperature. Journal of Geophysical Research: Atmospheres 113,

1–12.
Valor, E., Caselles, V., 1996. Mapping land surface emissivity from NDVI: application to European, African, and South American areas. Remote Sens. Environ. 57, 167–184. https://doi.org/10.1016/0034-4257(96)00039-9.
Verbrugghe, M., Cierniewski, J., 1998. Influence and modelling of view angles and microrelief on surface temperature measurements of bare agricultural soils. ISPRS J. Photogramm. Remote Sens. 53, 166–173.
Verhoef, W., 1984. Light-scattering by leaf layers with application to canopy reflectance modeling - the Sail model. Remote Sens. Environ. 16, 125–141.
Verhoef, W., Jia, L., Xiao, Q., Su, Z., 2007. Unified optical-thermal four-stream radiative transfer theory for homogeneous vegetation canopies. IEEE Trans. Geosci. Remote Sens. 45, 1808–1822.
Vinnikov, K.Y., Yu, Y., Goldberg, M.D., Tarpley, D., Romanov, P., Laszlo, I., Chen, M., 2012. Angular anisotropy of satellite observations of land surface temperature. Geophys. Res. Lett. 39, L23802. https://doi.org/10.1029/2012GL054059.
Voogt, J.A., 2008. Assessment of an urban sensor view model for thermal anisotropy. Remote Sensing of Environment, Soil Moisture Experiments 2004 (SMEX04) special issue 112, 482–495. doi:https://doi.org/10.1016/j.rse.2007.05.013.
Voogt, J.A., Oke, T.R., 1997. Complete Urban Surface Temperatures. J. Appl. Meteorol. 36, 1117–1132. https://doi.org/10.1175/1520-0450(1997)036<1117:CUST>2.0.CO;2.
Voogt, J.A., Oke, T.R., 1998. Effects of urban surface geometry on remotely-sensed surface temperature. Int. J. Remote Sens. 19, 895–920. https://doi.org/10.1080/014311698215784.
Voogt, J.A., Oke, T.R., 2003. Thermal remote sensing of urban climates. Remote Sensing of Environment, Urban Remote Sensing 86, 370–384. https://doi.org/10.1016/S0034-4257(03)00079-8.
Wald, A.E., 1994. Modeling thermal infrared (2–14 μm) reflectance spectra of frost and snow. Journal of Geophysical Research: Solid Earth 99, 24241–24250. https://doi.org/10.1029/94JB01560.
Wald, A.E., Salisbury, J.W., 1995. Thermal infrared directional emissivity of powdered quartz. Journal of Geophysical Research: Solid Earth 100, 24665–24675.
Wan, Z.M., Dozier, J., 1996. A generalized split-window algorithm for retrieving land-surface temperature from space. IEEE Trans. Geosci. Remote Sens. 34, 892–905.
Wan, Z.M., Li, Z.L., 1997. A physics-based algorithm for retrieving land-surface emissivity and temperature from EOS/MODIS data. IEEE Trans. Geosci. Remote Sens. 35, 980–996.
Wang, D., Chen, Y., Cui, Y., Sun, H., 2018a. A geometric model to simulate urban thermal anisotropy for simplified neighborhoods. IEEE Trans. Geosci. Remote Sens. 56, 4930–4944. https://doi.org/10.1109/TGRS.2018.2842794.
Wang, D., Chen, Y., Zhan, W., 2018b. A geometric model to simulate thermal anisotropy over a sparse urban surface (GUTA-sparse). Remote Sens. Environ. 209, 263–274. https://doi.org/10.1016/j.rse.2018.02.051.
Wang, H., Xiao, Q., Li, H., Du, Y., Liu, Q., 2015. Investigating the impact of soil moisture on thermal infrared emissivity using ASTER data. IEEE Geosci. Remote Sens. Lett. 12, 294–298. https://doi.org/10.1109/LGRS.2014.2336912.
Wang, K., Liang, S., 2009. Evaluation of ASTER and MODIS land surface temperature and emissivity products using long-term surface longwave radiation observations at SURFRAD sites. Remote Sens. Environ. 113, 1556–1565. https://doi.org/10.1016/j.rse.2009.03.009.
Wang, K., Wan, Z., Wang, P., Sparrow, M., Liu, J., Zhou, X., Haginoya, S., 2005. Estimation of surface long wave radiation and broadband emissivity using Moderate Resolution Imaging Spectroradiometer (MODIS) land surface temperature/emissivity products. Journal of Geophysical Research: Atmospheres 110. https://doi.org/10.1029/2004JD005566.
Wang, N., Tang, B., Li, C., Li, Z., 2010. A generalized neural network for simultaneous retrieval of atmospheric profiles and surface temperature from hyperspectral thermal infrared data, in: 2010 IEEE International Geoscience and Remote Sensing Symposium. Presented at the 2010 IEEE International Geoscience and Remote Sensing Symposium, pp. 1055–1058. doi:https://doi.org/10.1109/IGARSS.2010.5651405
Wang, W., Liang, S., Augustine, J.A., 2009. Estimating high spatial resolution clear-sky land surface upwelling longwave radiation from MODIS data. Geoscience and Remote Sensing, IEEE Transactions on 47, 1559–1570. https://doi.org/10.1109/TGRS.2008.2005206.
Watts, P.D., Allen, M.R., Nightingale, T.J., 1996. Wind speed effects on sea surface emission and reflection for the along track scanning radiometer. J. Atmos. Ocean. Technol. 13, 126–141. https://doi.org/10.1175/1520-0426(1996)013<0126:WSEOSS>2.0.CO;2.
Webster, C., Westoby, M., Rutter, N., Jonas, T., 2018. Three-dimensional thermal characterization of forest canopies using UAV photogrammetry. Remote Sens. Environ. 209, 835–847. https://doi.org/10.1016/j.rse.2017.09.033.
Wen, J., Liu, Qiang, Xiao, Q., Liu, Qinhuo, You, D., Hao, D., Wu, S., Lin, X., 2018. Characterizing land surface anisotropic reflectance over rugged terrain: a review of concepts and recent developments. Remote Sens. 10, 370. https://doi.org/10.3390/rs10030370.
Wiscombe, W.J., Warren, S.G., 1980. A Model for the Spectral Albedo of Snow .1. Pure Snow. J. Atmos. Sci. 37, 2712–2733.
World Meteorological Organization, 2016. The Global Observing System for Climate: Implementation Needs.
Wu, X., Smith, W.L., 1997. Emissivity of rough sea surface for 8–13 μm: modeling and verification. Appl. Opt., AO 36, 2609–2619. doi:https://doi.org/10.1364/AO.36.002609.
Wu, Y., Wang, N., He, J., Jiang, X., 2015. Estimating mountain glacier surface temperatures from Landsat-ETM + thermal infrared data: a case study of Qiyi glacier, China. Remote Sens. Environ. 163, 286–295. https://doi.org/10.1016/j.rse.2015.03.026.
Xu, X., Chen, L., Zhuang, J., 2001. Genetic inverse algorithm for retrieval of component temperature of mixed pixel by multi-angle thermal infrared remote sensing data. Sci. China Ser. D-Earth Sci. 44, 363–372. https://doi.org/10.1007/BF02907107.
Xu, X., Fan, W., Chen, L., 2002. Matrix expression of thermal radiative characteristics for an open complex. Sci. China. Ser. D Earth Sci. 45, 654–661.
Yan, G., Ren, H., Hu, R., Yan, K., Zhang, W., 2012. A portable Multi-Angle Observation System, in: 2012 IEEE International Geoscience and Remote Sensing Symposium. Presented at the 2012 IEEE International Geoscience and Remote Sensing Symposium, pp. 6916–6919. doi:https://doi.org/10.1109/IGARSS.2012.6352572
Yan, G., Wang, T., Jiao, Z., Mu, X., Zhao, J., Chen, L., 2016. Topographic radiation modeling and spatial scaling of clear-sky land surface longwave radiation over rugged terrain. Remote Sens. Environ. 172, 15–27. https://doi.org/10.1016/j.rse.2015.10.026.
Yan, G.J., Jiang, L.M., Wang, J.D., Chen, L.F., Li, X.W., 2003. Thermal bidirectional gap probability model for row crop canopies and validation. Sci. China. Ser. D Earth Sci. 46, 1241–1249. https://doi.org/10.3321/j.issn:1006-9267.2002.10.010.
Yang, J., Wong, M.S., Menenti, M., Nichol, J., 2015. Modeling the effective emissivity of the urban canopy using sky view factor. ISPRS J. Photogramm. Remote Sens. 105, 211–219. https://doi.org/10.1016/j.isprsjprs.2015.04.006.
Yang, J., Wong, M.S., Menenti, M., Nichol, J., Voogt, J., Krayenhoff, E.S., Chan, P.W., 2016. Development of an improved urban emissivity model based on sky view factor for retrieving effective emissivity and surface temperature over urban areas. ISPRS J. Photogramm. Remote Sens. 122, 30–40. https://doi.org/10.1016/j.isprsjprs.2016.09.007.
Yu, T., Gu, X., Tian, G.L., LeGrand, M., Baret, F., Hanocq, J.F., Bosseno, R., Zhang, Y., 2004. Modeling directional brightness temperature over a maize canopy in row structure. Geoscience and Remote Sensing, IEEE Transactions on 42, 2290–2304. https://doi.org/10.1109/tgrs.2004.834196.
Yu, W., Li, J., Liu, Q., Zeng, Y., Zhao, J., Xu, B., Yin, G., 2018. Global land cover heterogeneity characteristics at moderate resolution for mixed pixel modeling and inversion. Remote Sens. 10, 856. https://doi.org/10.3390/rs10060856.
Yu, Y.Y., Pinheiro, A.C., Privette, J.L., 2006. Correcting Land Surface Temperature Measurements for Directional Emissivity Over 3-D Structured Vegetation. Proc. of the SPIE Remote Sensing and Modeling of Ecosystems for Sustainability, San Diego, CA.
Yu, Y.Y., Tarpley, D., Privette, J.L., Goldberg, M.D., Raja, M., Vinnikov, K.Y., Xu, H., 2009. Developing algorithm for operational GOES-R land surface temperature product. IEEE Trans. Geosci. Remote Sens. 47, 936–951.
Zakšek, K., Schroedter-Homscheidt, M., 2009. Parameterization of air temperature in high temporal and spatial resolution from a combination of the SEVIRI and MODIS instruments. ISPRS J. Photogramm. Remote Sens. 64, 414–421. https://doi.org/10.1016/j.isprsjprs.2009.02.006.
Zeng, Y., Li, J., Liu, Q., Huete, A.R., Xu, B., Yin, G., Zhao, J., Yang, L., Fan, W., Wu, S., Yan, K., 2016. An iterative BRDF/NDVI inversion algorithm based on a posteriori variance estimation of observation errors. IEEE Trans. Geosci. Remote Sens. 54, 6481–6496. https://doi.org/10.1109/TGRS.2016.2585301.
Zhan, W., Chen, Y., Zhou, J., Li, J., 2011. An algorithm for separating soil and vegetation temperatures with sensors featuring a single thermal channel. IEEE Trans. Geosci. Remote Sens. 49, 1796–1809.
Zhan, W., Chen, Y., Voogt, J.A., Zhou, J., Wang, J., Ma, W., Liu, W., 2012. Assessment of thermal anisotropy on remote estimation of urban thermal inertia. Remote Sens. Environ. 123, 12–24. https://doi.org/10.1016/j.rse.2012.03.001.
Zhan, W., Chen, Y., Zhou, J., Wang, J., Liu, W., Voogt, J., Zhu, X., Quan, J., Li, J., 2013. Disaggregation of remotely sensed land surface temperature: literature survey, taxonomy, issues, and caveats. Remote Sens. Environ. 131, 119–139. https://doi.org/10.1016/j.rse.2012.12.014.
Zhang, R., Sun, X., LI, Z.-L., Su, H., Tang, X., Stoll, M.P., 2000. Revealing of major factors in the directional thermal radiation of ground objects——a new way for improving the precision of directional radiant temperature measuring and data analysis. Science in China(Series E:Technological Sciences) 34–40.
Zhang, R., Rong, Y., Tian, J., Su, H., Li, Z.-L., Liu, S., 2015. A remote sensing method for estimating surface air temperature and surface vapor pressure on a regional scale. Remote Sens. 7, 6005–6025. https://doi.org/10.3390/rs70506005.
Zhao, W., Li, A., Bian, J., Jin, H., Zhang, Z., 2014. A synergetic algorithm for mid-morning land surface soil and vegetation temperatures estimation using MSG-SEVIRI products and TERRA-MODIS products. Remote Sens. 6, 2213–2238. https://doi.org/10.3390/rs6032213.